Rational Ligand Design for Charge Transfer in Quantum Dots

By

Andrew Dylan La Croix

Dissertation
Submitted to the Faculty of the
Graduate School of Vanderbilt University
in partial fulfillment of the requirements
for the degree of

DOCTOR OF PHILOSOPHY
in
Chemistry
October 31st, 2018
Nashville, Tennessee

Approved:

Janet E. Macdonald, Ph.D.

Timothy P. Hanusa, Ph.D.

Jeffrey N. Johnston, Ph.D.

Sandra J. Rosenthal, Ph.D.

D. Greg Walker, Ph.D.

DEDICATION

“If brute force doesn’t work, you aren’t using enough.” – Sherrilyn Kenyon

To Mama, Daddy, Matthew, Emily, Summer, and Sean.

This degree is much more a testament to your support than my own accomplishments.

ACKNOWLEDGEMENTS

This work was supported financially by the Vanderbilt Department of Chemistry, TN-SCORE (NSF EPS-1004083), and the Stanley and Ann T. Tarbell Endowment Fund. Portions of this work were performed at the Vanderbilt Institute of Nanoscale Science and Engineering, using facilities renovated under TN-SCORE (DMR 0907619) and NSF EPS-1004083. Computations were done using the Extreme Science and Engineering Discovery Environment (XSEDE) supported by National Science Foundation grant number ACI-1053575 as well as the National Energy Research Scientific Computing Center (NERSC), a DOE office of Science User Facility supported by the Office of Science of the U.S. Department of Energy under Contract No. DE-AC02-05CH11231. Financial support for travel to academic conferences to present the research described in this dissertation was provided by the Graduate School at Vanderbilt.

Though my tenure in graduate school was long, the time passed quickly in the company of amazingly supportive colleagues. It cannot be overstated that, even though immense personal effort is exerted, achieving the goal of graduating with a doctorate is impossible without the assistance of those who have been there before you, those who are going there with you, and those who are ready for you to return home.

Janet, your vivacious attitude towards science, teaching, and life has inspired me to (believe it or not) always see the positive side of every result, every conclusion, every problem, and every answer. I will always appreciate the patience and kindness you have for everyone you meet, especially towards myself after going through so many health issues. Thank you for allowing me into your lab, letting me put your ideas to work in the fume hood, bringing us ketchup chips from Canada, and pushing me towards greater things. I would also like to thank the members of my committee, Dr. Hanusa, Dr.

Johnston, Dr. Rosenthal, and Dr. Walker for always being available to answer my questions, no matter how trivial they may have been.

Everyone in the Macdonald group, present and past, has been simply amazing to work with. Emil, the prodigal post doc, you have been an incredible leader to me and to our entire lab. You taught me everything when I first joined the lab, and you taught me how to start looking for jobs. Keep training for that Ironman. Mike, thank you for always being able to tell me the paper which I was thinking of. It's an impressive skill. Shane, thank you for being there in tough times and always being there to talk or take a walk. Alice, running a marathon was not something I ever planned to do, nor will I likely ever do again, but I'll never forget all the miles run and philosophical discussions with you. Thank you for being such a great friend and always putting up with my questions about nothing. Nikki, you taught me more about being a mentor than anyone else; it is suffice to say you are great teacher yourself. You will go far, and I am so proud of you. Laura, thank you for keeping me hip with the times and always being so upbeat. Bryson, though our time together was brief, the cigarettes we smoked were not. Never lose your sense of humour and keep being yourself. Evan, I am always amazed at your attention to detail and patience. It's incredible. I've enjoyed our talks, and I wish the best for you and yours. Jordan, J-Unit, Jor-Jor Rhodes, J. R.: thanks for always being willing to help. Never cut your hair. Madeleine, Nathan, and Chris, I am sure you are going to lead the lab far, as long as you continue the time-honoured tradition of the lab call.

Outside of my immediate lab, there have been many that have been crucial to my success. Keri, Connor, and the rest of the Porter Lab, thank you for access to your equipment, chemicals, and knowledge. Andy, thanks for explaining all of the computational work simply enough for a chemist. Kemar, thanks for all of the spectroscopy help, and especially for that time you didn't let me burn my eye out with a laser. Thank you Don Stec for NMR assistance, Andrzej for help with various equipment, Kristein, Clara, and Dr. List for teaching help, and James for endless TEM help.

Last, but most certainly not least, I need to thank the foundation of why I went to Vanderbilt and how I was able to make it through all of the hardships to see the end: my family. Were it not for my desire to make you proud, I never would have attempted what seemed such a lofty goal. Mama, thank you for everything you've done throughout the years. From cub scouts, to piano lessons, to flying to Nashville to take care of me when my health got the best of me, I truly appreciate all of it. Without you at my back pushing me and supporting me, I wouldn't have made it this far. Daddy, thank you for all you've taught me about everything. I can credit you with helping me learn how to think about solving and fixing things, and I never would have been able to keep my car running or house together without your frequent advice. I look forward to helping you back home. Matthew, thanks for providing comic relief as my roommate the first few years of grad school. Those were tough times, and I needed you there. Emily, I can't wait to spend more time with you once I get home. I missed out on most of your teenage years, but I suppose we'll pick it up at 20. We have years of board games to catch up on. Summer, we've been through a lot together. Some good, some bad. Thank you for always being there for me and picking me up when I need it most. Lauren, thanks for everything in the last stretch. Don't be a stranger! Sean, thank you for all of your support in so many ways since freshman year of high school. I hope we have many years to come.

Here's to my family. This is for you.

TABLE OF CONTENTS

Page

CHAPTER

LIST OF FIGURES

Figure Page

Chapter 1

1 INTRODUCTION

1.1 The Non-renewable Earth

Worldwide usage of non-renewable energy is not sustainable given current growth in energy demands. For this reason, alternative energy sources need to be developed alongside current sources, so that a global energy crisis is averted when the time comes that energy can no longer reliably be sourced from non-renewable resources (estimated to occur within the next 53 years).[1] Several renewable sources, such as hydro, wind, geothermal, and solar have been studied in regards to meeting this need.[2] Of these, solar stands out as an extremely promising candidate for several reasons. Firstly, the amount of energy which strikes the earth yearly from the sun is estimated to be nearly 10,000x the current global energy demand.[3] Secondly, the application of this form of renewable energy could be easily adapted to open land, or to urban environments by affixing solar cells to the roofs of buildings or integrating them into windows.[4] Finally, the harvesting of solar light is an option which, in recent years, has become increasingly affordable for consumers in developed countries, and stands to be deployable for developing countries as well.

Currently, the most commonly utilized type of solar cell is made of silicon. This material has served well as an entry into utilizing solar energy, but there are factors which are major drawbacks for its use. For instance, in order to absorb enough light to make a usable solar cell, layers of silicon ~ 100 μm thick must be used to achieve 90% light absorption.[5] This is in contrast with other materials which have the capability of absorbing the same amount of light while using 0.05-0.40 μm thick layers.[6] The theoretical maximum efficiency for single p-n junction silicon cells is 33.7%,[7] while solar cells available for purchase generally show efficiencies in the range of 13-24%.[8,9] Lastly, utilizing silicon in solar requires a large amount of energy in processing, and consequently time and money, which must be invested in the purification of Si and manufacturing of the solar cells.

Given the restrictions of solar cells using pure Si, resources have been invested in developing new materials for solar energy capture which possess direct band gaps and lower costs of manufacturing. Of considerable interest are colloidal semiconductor nanoparticles. Nanoparticles (NPs), very small pieces of material with a diameter of 1-100 nm, are desirable for use in solar cells because they are easily solution processable and can have very high extinction coefficients.[10] Added to this, many of these materials from which NPs are fabricated, such as CdSe and PbS, absorb well in the visible range of light, and possess tunable bandgaps *via* quantum confinement. The combination of these qualities allows for a small amount of easily processed material to be made and tuned to specific parameters to achieve desired properties for a solar cell. **Figure 1.1** outlines the tremendous progress in the improvement of solar cell efficiency comparing quantum dot (QDs, a type of NP under quantum confinement [vide infra]) solar cells to traditional silicon solar cells.

Utilizing solar cells to directly convert the sun's energy into electricity is the most straightforward method of exploiting photonic energy, but another possibility is through photocatalysis. In a traditional solar cell, the electricity generated by the sun must be stored in a battery. By utilizing the sun's energy to instead directly reduce water into hydrogen gas, the energy is being stored in the chemical bonds of H_2 as a fuel. This method of energy storage is promising because compressed H_2 has a very high energy density, and the oxidation of H_2 with O_2 only produces water vapor as a byproduct.[11] While safe H_2 storage still remains a challenge, methods of producing H_2 using sunlight and H_2O via NPs of various types have been reported.[12–16] Forward progress in this field requires the ability to effectively split water into H_2 and O_2 utilizing a method which harnesses clean energy in order to produce this energy source.

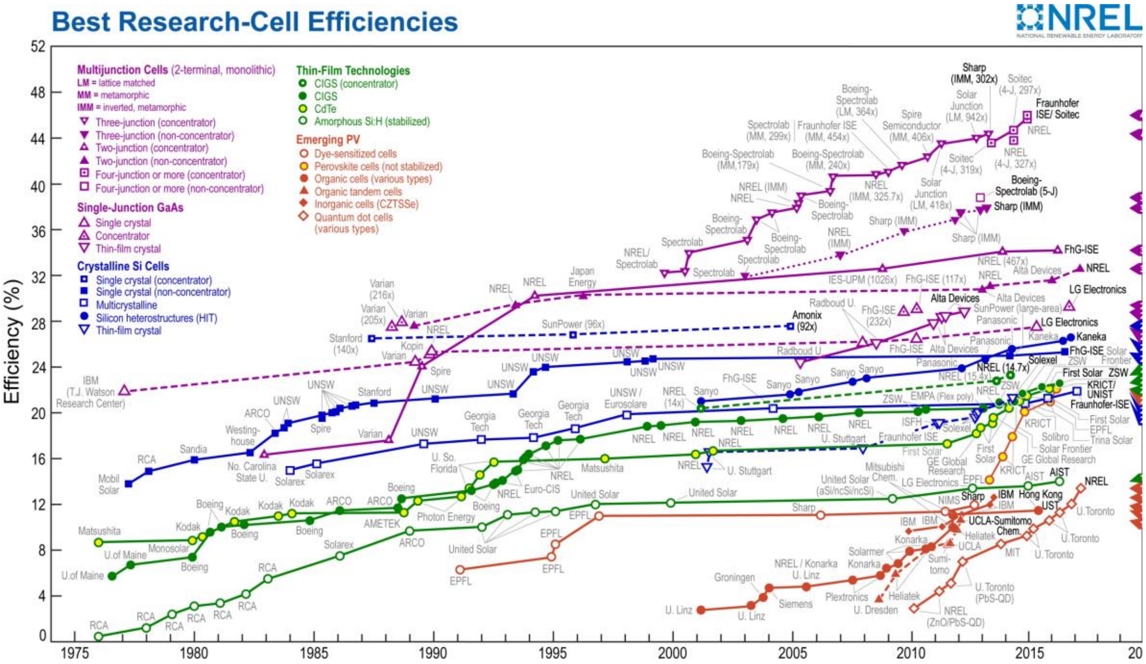

Figure 1.1 Solar Cell Efficiencies. The trend in increasing efficiencies of typical solar cell types shown since 1975. Si cells are common in commercial production, but have not seen near the improvement of multijunction, thin-film, or photo-voltaic technology. This plot is courtesy of the National Renewable Energy Laboratory, Golden, CO.

The following introductory sections will cover the fundamentals of nanoparticles including synthesis, surface interactions and challenges, and quantum confinement effects. Fundamental synthetic details must be understood in order to control, not only of the resulting size and morphology, but also the chemistry between the nanoparticle surface and surrounding environment. Further knowledge of the intrinsic materials properties are necessary when considering quantum confinement, and how changing electronic properties of a material will affect the ultimate application. Further discussion of the applications of these materials to solar cells and photocatalysis applications will follow.

1.2 Overview of Nanoparticles: Synthesis and Properties

NPs can be synthesized from many different types of materials including metals, metal compounds, semiconductors, and insulators.[10,17,18] While intense scientific research has been undertaken on these structures in recent decades, their use was unknowingly perpetuated in glass making as early as the fourth century. Au NPs feature light absorption around 520 nm due to surface plasmon resonance, a phenomena which is caused by oscillations of electrons on the surface of the material, resulting in a red or pink coloration.[19] This property was used to color the well-known Lycurgus cup and is also used in stained glass. The unique properties of nanoscale materials were, much later, specifically recognized by Michael Faraday as he noted that Au, when pressed into thin sheets, possessed unique properties not seen in bulk pieces of Au.[20] Later in 1959 the famed physicist Richard Feynman presented a talk titled *There's Plenty of Room at the*

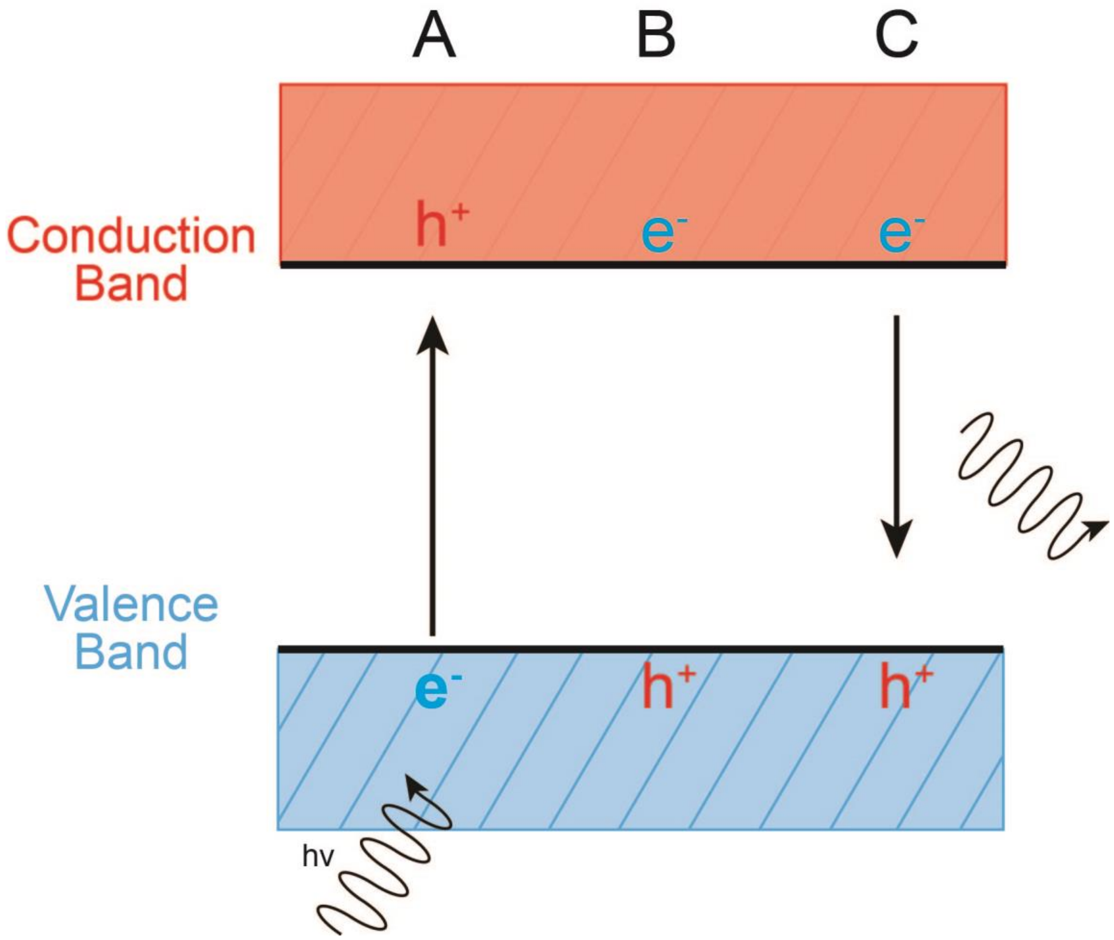

Figure 1.2: Visual Depiction of semiconductor photoabsorption. A) Upon the absorption of the appropriate amount of energy, the electron is excited from the valence band to the conduction band. B) An exciton pair is formed. At this stage the charges may be used to perform oxidative or reductive processes. C) The electron may recombine with the hole, giving off energy equal to that of the bandgap either as a photon (shown) in emissive radiative recombination or through heat in non-radiative recombination.

Bottom, where he heralded the unexplored realm of very small structures as one with vast potential for discovery.[20] The following decades saw an increased effort to both synthesize and characterize materials of smaller sizes for various applications.

While different types of NPs have unique applications, semiconductor NPs are of particular interest for solar energy capture. In a semiconductor, charge carriers are only generated upon the input of energy at a value equal to or greater than the band gap of the material. The amount of energy required is intrinsic to the particular material. For instance, if CdS is bombarded with visible light, an exciton pair (a negative charge [electron] in the condution band and positive charge [hole] in the valence band) will be generated. This is because the bandgap, or amount of energy required to generate an exciton pair, is 2.42 eV and falls within the energy spectrum of visible light at 512 nm.[21] At this point the electron and hole can be used for reductive and oxidative processes, respectively, or the electron can fall back to ground state and emit heat or a photon of light (**Figure 1.2**).

1.2.1 Nanoparticle Synthesis

NPs can be produced through top down methods such as the laser ablation or mechanical grinding of bulk materials[22–24] or by bottom up methods such as sol-gel techniques, self-assembly, and chemical colloidal synthesis.[25–28] In the remainder of this dissertation, bottom-up colloidal NP synthesis will be the focus. In particular, II-VI chalcogenide NPs, such as CdS, CdSe, and PbS, are highlighted extensively due to excellent material stability, appropriate band position for water reduction/oxidation, energetically relevant quantum confinement properties, and previous research done on the fundamental physical and optical properties of the materials. Colloidal NP syntheses are performed in organic solution and involve long ligands, which serve to stabilize the NP surfaces as they form. The formation of NPs can be understood by LaMer nucleation theory, which describes the trade-off between the favorable change in Gibbs free energy of forming a solid versus the unfavorable change in creating high energy surfaces. The equation below demonstrates this:

$$\Delta G_N(\mathrm{r}) = \frac{4}{3}\pi r^3 \Delta G_V + 4\pi r^2 \gamma \qquad \text{Eq. 1.1}$$

where r represents the radius of the NP, ΔG_V represents the free energy of forming a new solid, and γ represents the surface energy of the solid. The formation of a material is favorable, and therefore the first term of this equation will be negative. However, exposed surface states to the outside system will cause more interactions requiring surface passivation, thus being a positive term. Ligands are used to lower this surface energy term and stabilize smaller particles. This explains why larger particles are more stable, since the surface area to volume ratio increases as the size of a NP decreases.

Two methods are generally used in colloidal semiconducting NP syntheses: heat-up and hot injection. In a heat-up reaction, all reagents are in the reaction flask simultaneously as the temperature is increased. This causes the formation of the precursors of the cationic and anionic components of the compound semiconductor in situ. Once a temperature is reached that provides sufficient activation energy to overcome the energy cost of the formation of new surfaces, the molecular species will begin to grow over a period of time into molecular clusters. This process continues until the precursors are consumed, equilibrium with dissolved compounds is reached, or the heat is removed. The hot injection method involves the separation of

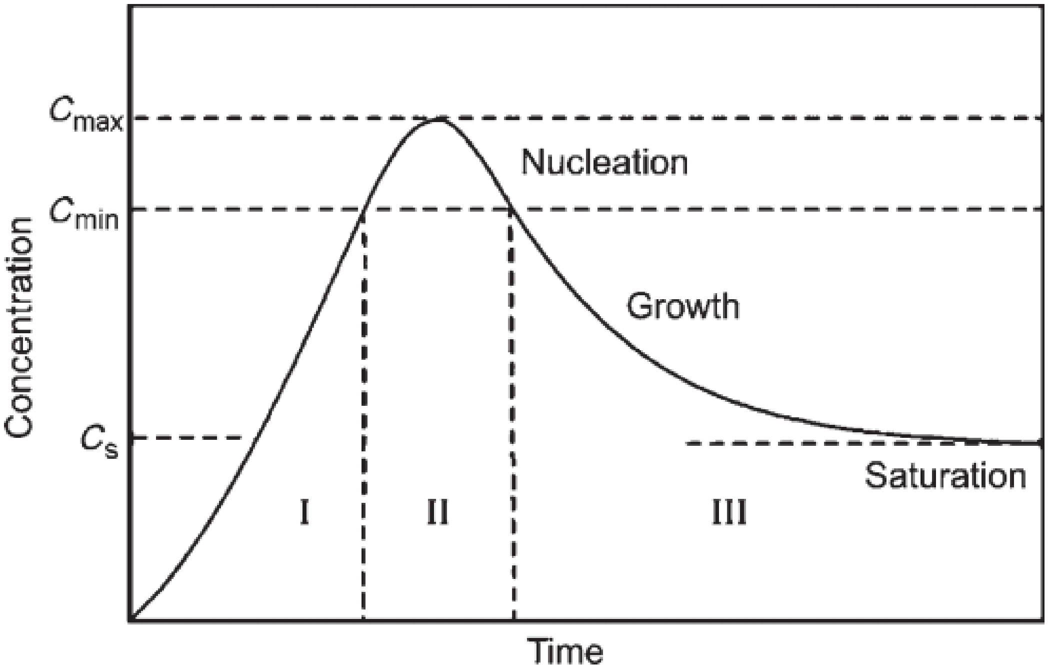

Figure 1.3: Visual Depiction of LaMer Nucleation Theory. During NP synthesis once the concentration of precursors reaches a critical point (between C_{max} and C_{min} in the figure, known as super saturation) nucleation occurs. Once the concentration falls below the nucleation threshold (C_{min}) nanoparticles will continue to grow until precursor consumption causes the concentration to drop below saturation (C_s). Reproduced with permission from reference 29.

cationic and anionic precursors. In this method one solution is injected into a second mixture which has been heated to a temperature above that at which growth occurs. This causes a fast nucleation and growth step relative to the heat-up method. The QDs will grow until the precursor concentration falls below the saturation point.[29] A rapid nucleation separated in time from growth leads to monodisperse NP samples. A visualization of these processes relating concentration and time to growth can be seen in **Figure 1.3**.

Another growth phenomenon which can occur is known as Ostwald ripening, which happens when the precursor concentration is depleted. Here smaller particles will dissolve and their ions are added to other, larger particles. This process is energetically favorable because the dissolution of small particles reduces the ratio of surface area to volume, thus lowering overall energy. While this causes an overall increase in average size, Ostwald ripening also causes an increase in the standard deviation of the size and results in polydispersity. This can be detrimental in some applications which require monodispersity for proper band alignment or NP packing.

Post either heat-up or direct injection synthesis, NPs are subjected to precipitation to remove byproducts. These byproducts could be unreacted precursors, degradation products from precursor decay, impurities from technical grade surfactants, and excess surfactant used during synthesis. Since the NPs from either a heat-up or hot injection method are coated in a corona of organic ligands, the particles are soluble in non-polar organic solvents. The surface ligands are typically long chain natural products such as oleic acid or oleylamine due to their availability, price, and lipophilicity. By adding a polar solvent such as methanol, ethanol, isopropanol, or acetone to the solution containing the NP, the NP will agglomerate with one another and precipitate from solution. The particles can then be separated from solution via centrifugation and supernatant removed.

A crucial factor in determining appropriate ligands for synthesis is that of binding strength to the material being made; during NP synthesis, a stronger or weaker binding molecule may

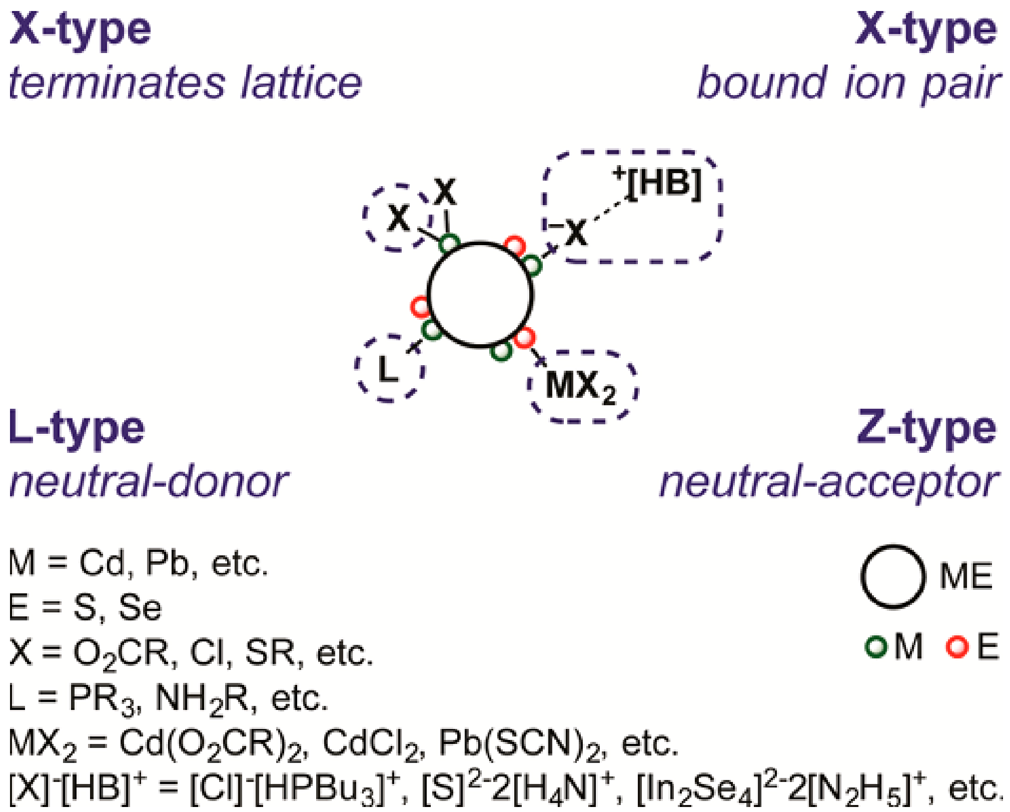

Figure 1.4: Types of Ligand Binding. Depiction of X, L and Z-type ligand binding to a NP. Reprinted (adapted) with permission from reference 31. Copyright 2013 American Chemical Society.

produce a particle which is larger or smaller, or vary the morphology of the final product. When considering bonding types, three different categories are commonly described: L, X, and Z, which correspond to neutral and anionic donors, and electron acceptors as shown in **Figure 1.4**.[30–32] Examples of L-type ligands are alkyl amines (such as olelyamine) or alkyl phosphines. Common X-type ligands are organic carboxylates and phosphonates which possess a negative charge. Z-type ligands are generally Lewis acids and typically coordinate to an anionic site. Z-type (a cationic species paired with two X-ligands) ligands have been observed to act as a capping layer around a nanoparticle surface in lieu of direct bonding between a single ligand and the nanocrystal lattice. It is important to remember these types of bonding interactions when designing experiments to control the size and morphology of the final product. X-type ligands can also be present in an ion bound pair such as the interaction between a S^{2-} anion with an ammonium cation. These classifications are also important when considering ligand exchanges (*vide infra*).

1.2.2 Nanoparticle Surface Characterization

In order for a NP to be useful in most applications, the interface with its outside environment must be understood and controlled. Complex chemistry occurs that affect both the particle and outside environment. For instance, formation of new bonds such as oxides on the NP surface can introduce trap states, which are new electronic states that can provide lower energy transitions, hindering quantum yields and charge transfer.[33] Change in the structure of the ligand corona (for instance, the addition of charged functional groups, metal ions, or shortening of ligands) can also introduce trap states, and the colloidal stability of the NPs may also be reduced. Further, leaching of metals such as Ag and Cd from NP surfaces is a possibility which can cause environmental and health concerns.[34] For these reasons, extensive research has been devoted to the surface chemistry of NPs. As the size of a NP decreases, the surface area to volume ratio increases; this fact is what makes NPs very active catalysts, as the surface sites are where chemical reactions occur. Of continuing interest to the scientific community is the characterization of these surfaces with respect to both the crystallographic facets and the organic ligands which cover the NP surface. In order to get a full picture of the nature of a surface, techniques which analyze different aspects of NP chemistry must be performed and results compared.

When characterizing the inorganic core of NPs, common techniques used are transmission electron micrscopy (TEM), selective area electron diffraction (SAED), scanning transmission electron spectroscopy (STEM), energy-dispersive X-ray spectroscopy (EDS), STEM-EDS, X-ray diffraction (XRD), powder X-ray diffraction (PXRD), and computational modeling.[35,36] TEM is a microscopy technique which utilizes electrons as “light” in a chamber under high vacuum. Since the wavelength of an electron is quite small under the acceleration voltages used in TEM, NPs of very small sizes can be directly visualized. The downside of this technique is that only elements which possess a sufficiently high Z number can be readily imaged, since the atoms must cause electrons to be scattered or diffracted which produces the image. This hindrance can be overcome through the conjunction of EDS and STEM. In STEM the electron beam is rastered across the sample and resulting data recorded for each point in two ways: dark field and bright field. Dark field records scattered electrons from the sample surface, while bright field records in line with the electron beam, as in TEM. EDS measurements record X-rays emitted due to electron irradiation at different energies which can be mapped to the ions which were struck. SAED and XRD give direct crystal lattice information, though through diffracting different energy sources.[37] SAED utilizes the diffracted electrons from a TEM to produce rings related to lattice parameters, while PXRD utilizes an X-ray source which illuminates a sample while the detector is moved at different angles to record incident X-rays. Combining direct imaging of NPs with information regarding the inorganic core through diffraction can then be supplemented with visualization of NP surfaces through programs such as Visualization for Electronic and Structural Analysis (VESTA). Visualization of surfaces can help in identifying growth mechanisms or chemical reactivity by showing prominent crystal facets as charged or neutral.

To gain a complete understanding of a NP, the surface ligand systems must also be examined. In colloidal NP systems, organic ligands coat the surface of nanoparticles resulting in a stable suspension in organic solvents. During synthesis long chain organic molecules with a high boiling point are used, but these are often replaced afterwards to facilitate denser packing of particles in films and or charge transfer out of the inorganic core, or provide attachment points for biological probes such as DNA or proteins.[38] Perhaps the simplest way to probe organic molecules on NP surfaces is nuclear magnetic resonance (NMR), but this technique comes with limitations not normally seen in molecular NMR. NMR utilizes radio frequency waves to cause the nuclear spin of nuclei to become excited, and then relax. The energy of relaxation can be measured and is slightly shifted depending on the chemical environment surrounding the nuclei being investigated. This allows for structural determination of molecules which are spin active such as ^{1}H or ^{13}C.[39–41] Since NMR performed on molecules free in solution relies on a similar relaxation rate for all protons of a specific nucleus, and the NP core affects the relaxation rates of nuclei nearby, surface broadening causes protons (or other nuclei being observed) close to the NP surface to give signals broad enough that they are not visible. Protons of a sufficient distance from the NP core (for instance, the alkene peaks in oleylamine) are still visible. Thus, NMR can be used to provide evidence of the existence of ligands containing peaks separated from the NP core, or to provide evidence of the absence of ligands used in synthesis. 2D NMR techniques such as diffusion ordered spectroscopy (DOSY) and nuclear Overhauser effect spectroscopy (NOESY) allow for studies on the equilibrium between ligands which are bound or free on NPs.[39] Other techniques used to observe surface ligands include X-ray photoelectron spectroscopy (XPS) which allows for observation of the oxidation states of atoms on the surface (thus providing evidence of functional groups or interactions with the crystal lattice), and thermogravimetric analysis (TGA) which allows one to determine the proportion by weight of a sample that makes up the organic shell versus the inorganic core.[42,43]

Given that the topic of this dissertation is specifically focused on semiconductor NPs, optical spectroscopy techniques are also particularly important in characterization. Semiconducting materials employed in photovoltaics and photocatalysis often utilize visible light, as ultimate applications usually involve utilizing the sun's energy to drive reactions forward. Therefore, UV-Visible spectroscopy (UV-Vis) is used to measure the amount of light absorbed by a material. This technique becomes very important when quantum confinement effects begin to shift absorption exciton peaks through the UV, visible, and near-IR ranges (*vide infra*). Fourier-Transform Infra-Red spectroscopy (FT-IR) is used to perform the same measurements, but for a broad region of the IR spectra. Information from IR gives stretching information which can be related to functional groups. Finally, photoluminescence spectroscopy (primarily fluorescence) is used to measure the emission of NPs after excitation at a set wavelength.[44] The ratio of the amount of light emitted to the amount of light absorbed is the quantum yield (QY). This value is particularly important when assessing the best application for a material; a NP being used as a biological "tag" would require a high QY for visibility, but a NP being used in a charge transfer application would want charges to be moved into the ligands, resulting in a "quench" in the QY. NPs are known for possessing remarkably high QY values, which has made them a popular choice for biological imaging applications.[45]

By combining all of these characterization techniques, an overall picture of a NP system can begin to be elucidated, allowing for the development of new NP syntheses and fine-tuning of ligand systems for new applications.

1.2.3 Quantum Confinement

Quantum confinement is a property which occurs in NPs when the size of the particle becomes smaller than the Bohr exciton radius (r_B) of the material. The Bohr exciton radius is a calculated intrinsic property of a material which represents the radius an exciton pair (hole and electron) will occupy in a bulk material upon excitation.[46] The following equation can be used to calculate this value:

$$r_B = \frac{\hbar^2 \varepsilon}{e^2}\left(\frac{1}{m_e^*} + \frac{1}{m_h^*}\right) \qquad \text{Eq. 1.2}$$

where m_e^* and m_h^* represent the mass of the electron and the mass of the hole, respectively. To envision at a molecular level what occurs when quantum confinement effects are observed, the linear combination of atomic orbitals (LCAO) can be employed.[47] In a bulk material, thousands and thousands of orbitals comprise the valence and conduction bands. As the size of a material is reduced from bulk to the nano size regime, the number of orbitals comprising the frontier molecular orbitals is greatly reduced. This results in discrete transitions of a higher energy as the number of orbitals is diminished and the electronic properties of the material shift from a bulk state to a molecular one. A representation of this is seen in **Figure 1.5**.[48] It is important to take into account the difference between the mass of the electron and the mass of the hole when determining the position of the valence and conduction band. As can be seen in the equation to calculate the Bohr exciton radius (**Eq. 1.2**), it is the inverse of the mass which is important in determination of r_B. Therefore, a smaller mass will have a larger effect on the movement of a band. Given that the mass of electrons is generally much smaller than the mass of holes, conduction bands will move to a higher energy at a greater rate than the valence

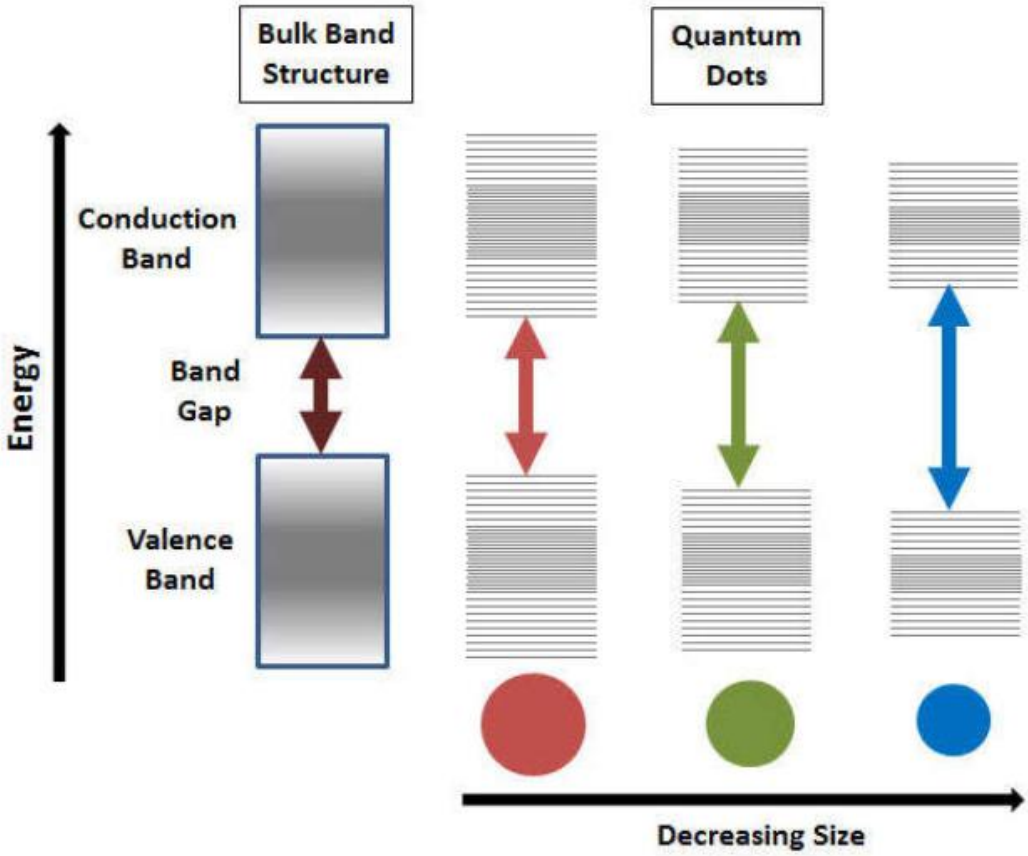

Figure 1.5: Quantum Confinement effects on Bandgaps. As NPs size decreases, the number of molecular orbitals decreases, causing the appearance of discrete energy levels. Reproduced from reference 48.

band moving to a lower energy when quantum confinement effects are observed. The Brus equation[49] takes into account the particle in a box interaction as the increased attraction of the exciton changes upon decreasing particle size:

$$E_g\,(\mathrm{r}) = E_g^0 + \frac{\hbar^2\pi^2}{2r^2}\left(\frac{1}{m_e^*} + \frac{1}{m_h^*}\right) - \frac{1.786e^2}{4\pi\varepsilon_0\varepsilon_r r} \qquad \text{Eq. 1.3}$$

where E_g^0 is the band gap energy for the semiconductor, r is the radius of the NP, $\hbar$ is Planck's constant, m_e^* and m_h^* are the mass of the electron and the mass of the hole respectively, ε_0 is the permittivity of free space, ε_r is the permittivity of the material, and e is the charge of an electron.

Since changing the bandgap of a semiconductor will change the amount of energy required to absorb a photon, the amount of energy emitted by a photon also changes. This property has led to the use of QDs of different sizes (and thus emitting different colors) for labeling cells in tissue for bio-imaging. The use of specifically functionalized QDs of different sizes, and therefore colors, allows the simultaneous labeling of multiple targets at once. Further, the ability to tune bandgaps to specific sizes allows for tailoring of QDs to be used in devices to encourage charge transport, as discussed below. The issue of charge transport is important for both device based and photocatalytic applications.[50]

1.3 Nanoparticle Applications

NPs have found niches in areas of science ranging from biology to physics. Perhaps one of the most widely known applications is that of biological imaging. There are several reasons for this including the ability to alter the wavelength of particle emission through size tuning, functionalize surfaces with any necessary groups or biological entities such as antibodies, and eliminate photo-bleaching which is seen in traditional organic emitters.[51,52] Though much less studied, nanoparticles have also been shown to exhibit second harmonic generation (SHG). SHG can be used to convert two photons of lower energy light into one photon of higher energy light.[53] This is relevant in the area of biological imaging due to the SHG from collagen.[54] While these fields continue to present interesting and useful data from a biological standpoint, the remainder of this dissertation will focus on the application of NPs in the areas of green chemistry, in particular that improving particles for photocatalysis and solar cells.

The holy grail of NP catalysis is that of complete water splitting, meaning that the generated electron is used for reduction of water to H_2 whilst the hole is used for the oxidation to O_2. It is necessary to note that complete water splitting has been successfully demonstrated in electrochemical cells, but since a potential must be applied to the cell it is not truly a green process.[55–57] For this reason, much research has been invested in the use of abundant solar energy as the source to perform water splitting.[58] Utilizing solar

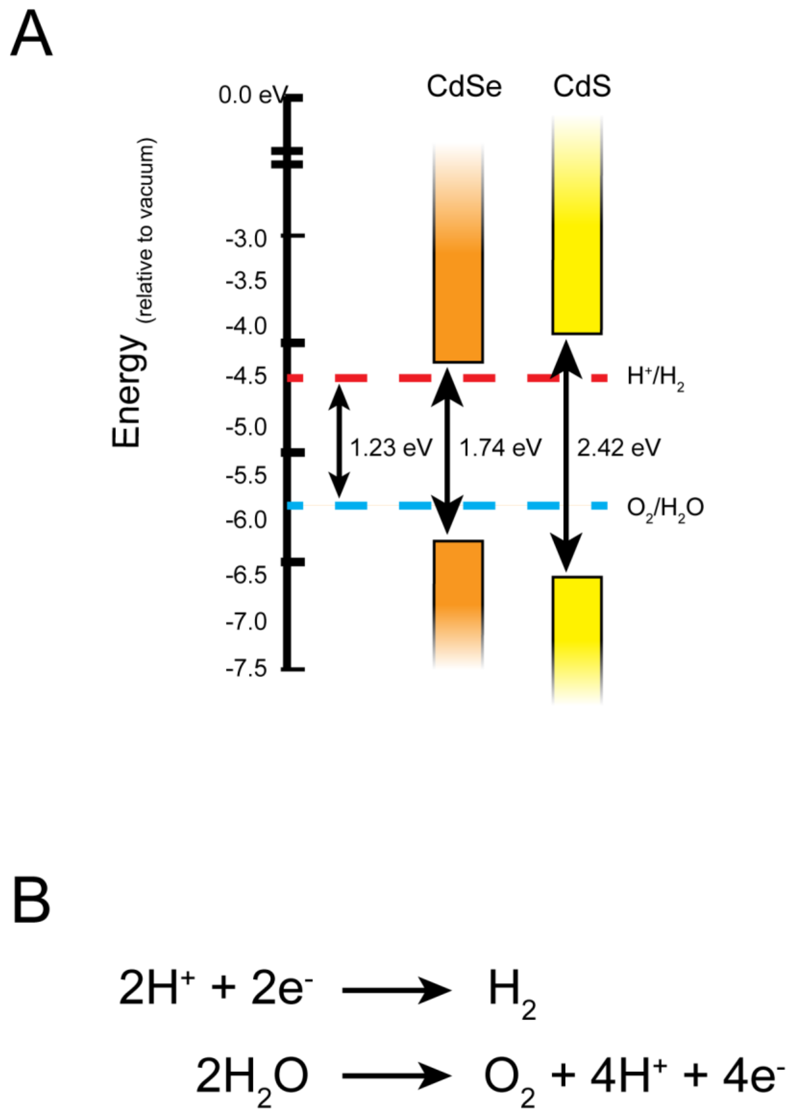

Figure 1.6. Energies and Half-reactions for Water Splitting. A) Diagram showing the minimum energy required for water splitting in relation to the alignments of CdSe and CdS. B) Half reactions of the water splitting reaction.

energy inherently introduces challenges to the reduction/oxidation mechanisms, primarily by limiting the energetic driving force to the band gap of visible light and requiring charges to be trapped on very long timescales relative to that which is normally seen. This is shown through the success of water reduction, but not oxidation, and the fact that reduction requires much less of an energetic driving force and occurs on much quicker timescales in comparison to water oxidation.[16] Bandgaps of commonly used semiconductor materials and the half reactions for water splitting are shown in **Figure 1.6**. Further applications of photocatalytic NP processes have utilized charge transfer for water remediation,[59] to combat biofouling of surfaces,[60] or to break down organic dyes.[61] These semiconducting materials possess the ability to coordinate or break down organic molecules and organisms which are otherwise difficult to remove.[62]

QDs have been utilized in devices including optoelectronics such as laser diodes, light emitting diodes, and solar cells. Concerning devices, the focus of this research is to improve the way in which QDs are used to fabricate a device such as a QD solar cells. In a typical QDSSC (depicted in **Figure 1.7**)[63], the QDs act as a photoabsorber which absorbs photons of light and separates the charges in order to generate a current. This requires the replacement of the charge insulating ligands originally on the QD surface. In a device, this process is generally performed via spin coating a solution of QDs onto a substrate, followed by removal of surface ligands in a low concentration 3-mercaptopropionic acid/methanol or ethanedithiol (EDT)/acetonitrile solution. An illustration of this procedure can be seen in **Figure 1.8**.[64]

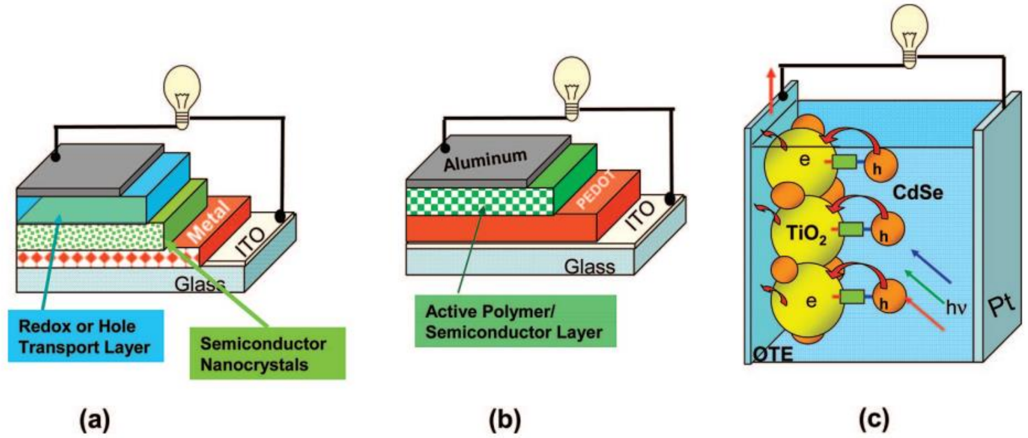

Figure 1.7. Depictions of various types of QDSSCs A) metal-semiconductor, B) polymer-semiconductor, and C) semiconductor-semiconductor. Reprinted (adapted) with permission from reference 63. Copyright 2008 American Chemical Society.

In order to have an efficient QDSSC, the QD film which is deposited must be uniform to facilitate charge transport. The primary issue with the aforementioned deposition method is that the ligand exchange occurs post deposition of particles into a film. This causes issues for multiple reasons including: solid state ligand exchanges on films can result in cracking as the inter-QD distance is drastically different after ligand exchange; surface leaching may occur during the exchange causing imperfect surfaces; the introduction of new molecular species in a dynamic environment can introduce new electronically active impurities;[65] and complete removal of the native ligands is a challenge.[66] Since ligand exchange to ligands such as MPA or EDT causes agglomeration of QDs if performed in solution, different methods of exchange are sought. Previous attempts at developing new methodology have included inorganic ligand exchange as well as amide bond cleavage.[67,68] Methods of cleavage reported herein will include the Fluorenylmethyloxycarbonyl (Fmoc) protecting group cleavage and photo-labile ligands.

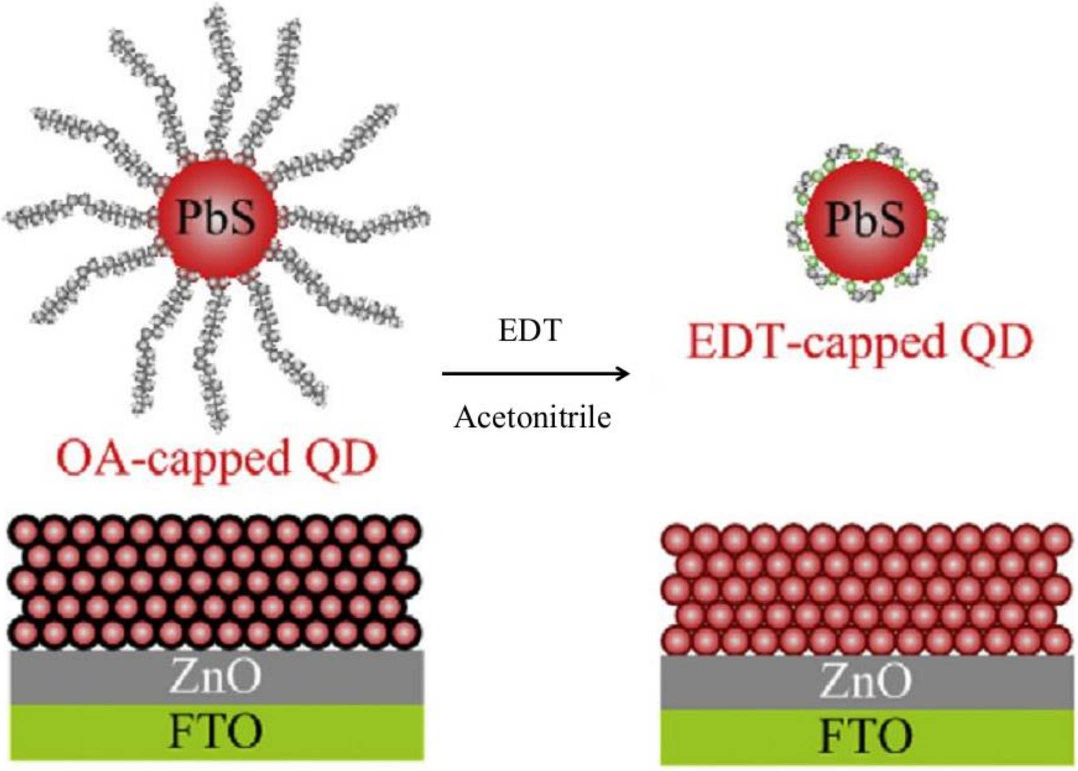

Figure 1.8. Deposition of PbS solar cells. PbS coated in native ligands and ligand-exchanged in the solid state with EDT. In this example ZnO and FTO are the electron transport layer and conductive substrate, respectively. Figure reproduced with modification from reference 64.

1.4 Scope of Dissertation

The focus of this dissertation will be to explain the importance of tailoring ligands for specific functionalities in the field of QD applications. The first portion of the document will cover the design and both experimental and theoretical testing of a ligand to be used for the extraction of holes from QDs. Hole extraction for oxidative purposes is a topic which, at this point in time, has been regarded largely as a nuisance rather than an opportunity. While electrons have been successfully used for reduction, holes have simply been eliminated through the use of sacrificial electron donors such as methanol. Chapter 2 covers the synthesis and study of a ligand designed to extract holes and trap them in a bound metal center.

Chapters 3 and 4 will focus on facile ligand cleavage for superior film production in QD devices. This will be accomplished through surface ligand modification. In particular, this is in regards to the cleavage of ligands which have been exchanged in a colloidal matter. By performing a complete exchange on particles in solution before shortening the ligands, films of a greater uniformity can be created. This method is in contrast to previous techniques which rely upon the formation of films followed by ligand exchange. Two methods will be discussed, one which involves the use of a mild base to cleave, and the other which utilizes light for cleavage. The final chapter will address a new binding mode being investigated in our lab known as the “crystal-bound” binding mode. Attention will be given to adapting this property to PbS and developing methods to control ligand functional groups.

Chapter 2

2 DESIGN OF A HOLE TRAPPING LIGAND

Light absorbed by NPs can be used to perform photocatalytic reactions, thus storing chemical energy in the bonds of molecules. The most well-known example of this is the splitting of water to H_2 and O_2. This chapter will cover attempts at adapting a colloidal semiconducting NP system towards utilizing photocatalysis for oxidative purposes. All synthetic work was carried out in the Macdonald lab, while spectroscopic and computational work was performed by Kemar Reid from the Rosenthal group and Andrew O'Hara from the Pantelides group, respectively. Data analysis and interpretation was performed in conjunction with all members.[69]

2.1 Introduction

With the growth in global energy demands comes the need for an alternative, clean energy source.[2,70] Hydrogen gas has for the past few decades been heralded as a potential alternative-energy candidate owing to its high energy storage capacity and lack of hazardous byproducts upon combustion.[71] The possibility of cleanly splitting water into hydrogen and oxygen gas has driven a broad field of research to investigate water splitting.[72–75] Utilizing nanoparticle (NP) systems to perform water splitting has been under intense investigation, as NPs have increased surface areas, tunable valence bands (VB) and conduction bands (CB), and synthetic control over size and shape; these NP features provide the opportunity to study electronic level alignment of excitons in the nanoparticle

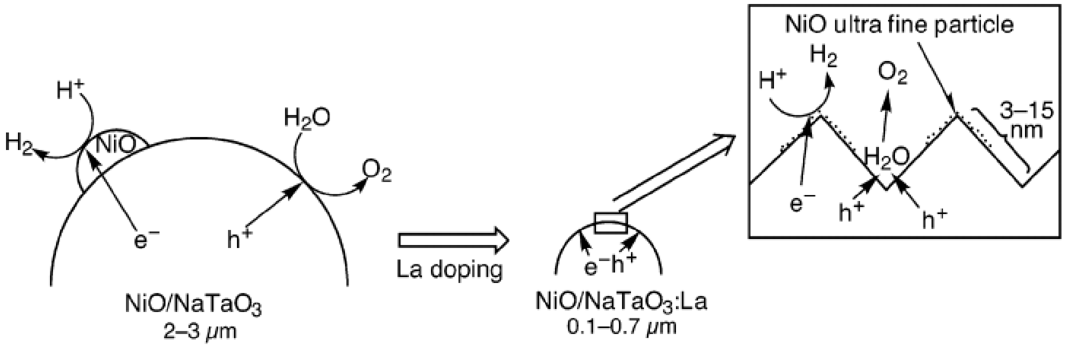

Figure 2.1: Depiction of various crystal facets in NiO/NaTaO$_3$:La NPs. Water is preferentially oxidized at the valleys of the jagged crystal face, while it is reduced preferentially at the peaks. Reprinted (adapted) with permission from reference 78. Copyright 2003 American Chemical Society.

core vs organic ligands,[76] and spatial attachment of multicomponent photocatalysts in a far more systematic manner.

The splitting of water into H_2 and O_2 has been demonstrated previously using both bulk and NP materials, the latter of which will be discussed in detail below.[15,77,78] The issue with previously studied water splitting methods is that the methods require the application of a potential, and in these cases the energy source is likely non-renewable. Examples of this are the use of MoS_2 grown on graphene and NiO/NaTaO$_3$:La structures.[55,79] Important information can be gleaned from these experiments, such as the latter case where it was shown that certain crystal facets promote H_2 or O_2 evolution. The authors demonstrated that in a jagged crystal face the valleys of NiO/NaTaO$_3$:La selectively oxidize water to O_2, while the peaks reduce the water to H_2 as in in **Figure 2.1**.[80] In this case the reaction was photocatalytic, but only under strong UV radiation which can only be provided through artificial means. In order to have a renewable system which is also efficient, a broader wavelength range of solar radiation needs to be employed.

In developing catalysts for photocatalytic water splitting, well studied semiconductors have been at the forefront of device research for some time. For example, CdS and CdSe/CdS nanorods (NRs) with attached metallic and metal oxide domains have been well studied for their ability to photoreduce water to H_2.[15,77,78] These systems and studies continue to suffer from limited stability of the particles and the requirement of sacrificial reductants, as the excited electron used for water reduction must be replenished from a molecule in solution.[74,81,82] Recent reports have highlighted that the interaction of sacrificial reductants for hole removal from the rods is the primary factor affecting quantum efficiency of hydrogen production,[78] and that near perfect photo-hydrogen conversion is possible.[15] Improved methods for hole transfer are, therefore, needed which will ultimately lead to complete water splitting. The time for hole transfer to ligands on the surface of a CdS or CdSe/CdS NR with coordinated metal centers has been reported to occur as quickly as 0.1-1 ns; Alivisatos et al. showed hole transfer to chemically inert thiol-tethered ferrocene derivatives,[83] and Dukovic et al. demonstrated 0.1-1 ns hole transfer to an adsorbed Ru complex, followed by 10-100 ns recombination with the electron on the Ru metal center.[15] Meanwhile, oxidative chemical transformations such as disulfide formation from thiolate ligands occur on the order of 10^4 ns.[84] It is also worthwhile to note that some of the fastest water oxidation on organometallic catalysts occur in 10^6 ns.[85] In comparison, the time of electron transfer to a Pt tip on a CdSe/CdS rod has been reported as 0.001-0.01 ns. The electron transfer and water reduction occurs on a much faster time scale than the oxidative processes.[13,86,87]

The focus of this research was to develop a system which could extract holes from a NR system on the same time-scale that electrons can be shuttled to a Pt tip, while also trapping the charges long enough for catalytic reaction to occur. Four points were considered in the design of a ligand for fast movement of holes: firstly, spatial overlap and continuous conjugation will promote ease of movement through the π orbitals of the ligand; secondly, a functional group known to be stable to oxidative processes while still being prone to hole trapping is necessary; thirdly, the ligand should contain a metal chelating moiety for potential catalytic reactions; and lastly, electronic transitions between the ligand and the CB should be disfavored in order to slow charge recombination. All of these properties are possible in a dithiocarbamate (DTC) functional group directly conjugated to 2,2'-bipyridine (Bipy). Previous reports have indicated that the DTC functional group is capable of sub-picosecond charge transfer when DTC is attached to known molecular hole acceptors.[88] DTC functional groups have shown to chelate CdS and CdSe while also showing spatial and energetic overlap with the VB,[89–92] while Bipy is a known chelator of water oxidation catalysts.[85] A representation of this system is seen in **Figure 2.2**.

Herein we report a theoretical and experimental study of a new ligand for CdS, 2,2'-bipyridine-4-ylcarbamodithioate (DTCBipy), and its further chelation of Fe(II). Fe(II) was chosen as it readily undergoes one-electron oxidation, has analogous chemistry to highly active Ru based water oxidation catalysts, is identified as a water oxidation catalyst in its own right, and the nanorod-ligand-metal hybrid system was experimentally accessible.[93,94] DFT calculations were performed using the Vienna ab initio simulation package (VASP)[95] for a free ligand and for a slab of CdS with the ligand covalently bound on the surface in order to determine the existence of midgap hole acceptor states. Hybridized energy levels and hole transfer dynamics from the CdS surface state were computed and indicated that successive hole transfer from the CdS to the ligand, then to the iron center, was faster than the radiative recombination from the CB to the VB of the CdS. Experimental assembly of the DTCBipy ligand system with chelated Fe(II) on fluorescent CdSe/CdS nanorods validated the theoretical predictions of the resulting absorbance spectra. The expected fluorescence quenches and Time Resolved Photoluminescence (TRPL) lifetimes were shortened due to the opening of new efficient non-radiative pathways.

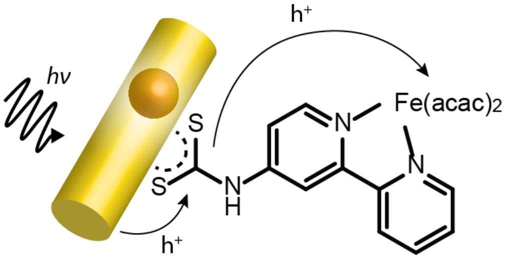

Figure 2.2. Schematic representation of the proposed system; a 2,2'-bipyridine group is covalently linked via a dithiocarbamate functional group for the use of hole transfer to an attached metal center for catalytically oxidative reactions. Reprinted (adapted) with permission from refrence 69. Copyright 2017 American Chemical Society.

2.2 Theoretical Study

In collaboration with Andrew O'hara from the group of Sokrates Pantelides, a computational comparison of the ligand and CdS energy levels gave encouraging results (see SI), and motivated more detailed calculations of a slab of CdS with the ligand covalently bound on the surface. The calculations of the pristine slab with a $(10\bar{1}0)$ CdS facet do not have any midgap states. The optimized structure, as obtained by DFT energy minimization, for DTCBipy on CdS has two filled mid-gap molecular states just above the surface confined VB. The charge densities for the four relevant states are plotted in **Figure 2.3.**

The relevant electronic states exhibit differing levels of contribution from the ligand and CdS wave functions. The wave functions for the mid-gap molecular states are predominantly comprised of the molecular wave functions, with a small contribution from the CdS. Likewise, the VB contains partial contribution from the ligand but retains predominantly CdS surface character. In contrast, the CB is almost purely of CdS origin with even spatial distributions throughout. As result, only a small narrowing of the CdS band gap is expected.

The optical absorption profile was obtained from the transition matrix elements between occupied and unoccupied states using VASP (SI). It was determined that the optical transitions between the mid-gap states and the CB minimum are dipole forbidden (with dipole oscillator strengths of less than 0.01), and consequently, the plotted calculated optical absorption (**Figure A. 1.**) has no peaks in the relevant wavelength region. The DTCBipy LUMO derived state sits significantly above the CB minimum of CdS and so the intramolecular excitations of the ligand are of sufficient energy to be occluded by the transitions of the semiconductor.

Relevant for through-bond charge transfer, there is spatial overlap of the wave function of the surface confined VB and the mid-gap states, and the two have differing wave function symmetry. Therefore, we can expect allowed electronic transitions between the VB and mid-gap states to be dipole allowed if either contains a hole. Using the calculated oscillator strengths for transitions between each mid-gap molecular state and the

VB, we calculate a hole transfer time of 370 ns from CdS to the DTCBipy. It is important to point out that this calculation assumes a density of 0.34 ligands per nm^2 whereas the experimental data (**Table A. 1.**) show the actual surface coverage on CdS NRs is almost an order of magnitude higher. As the hole acceptor states are localized molecular states, interactions between ligands should be a second order effect. This means rates can be scaled linearly with ligand coverage.[83] Therefore, linearly scaling for the experimentally relevant coverage of 2200 ligands per CdSe/CdS NRs (*vide infra*), a theoretical hole transfer time of 167 ps is calculated. Since hole localization to the CdS surface occurs in times only slightly longer than localization to the CdSe core[96–100] and the calculated rates for transfer to the ligands are much faster than exciton recombination for CdSe/CdS NRs,[15,83] this implies that hole transfer to the ligand states via the CdS surface state is a competitive process to core localization.

In the case of surface-attached DTCBipyFe(acac)$_2$, a similar small red shift of the CdS bandgap is expected due to hybridization of the VB with ligand states. Seven filled mid-gap molecular states are expected (**Figure 2.3**) States 2 and 4 are similar to the two mid-gap states in the Fe-free case. States 1, 2, and 3 demonstrate the conjugation of the dithiocarbamate group through to the Fe center. The upper three states are primarily due to molecular orbitals of the Fe d-states with surrounding atoms (essentially the three e_g-type states of a d^6 metal with octahedral coordination). These states are depicted in **Figure 2.3** and Figure A.2.

As in the case of DTCBipy, all transitions between mid-gap molecular states of DTCBipyFe and the CB are dipole forbidden, and the oscillator strength is less than 0.01. The additional features seen in the absorption spectra (Figure A. 1) are due to

(a) DTCBipy level alignment

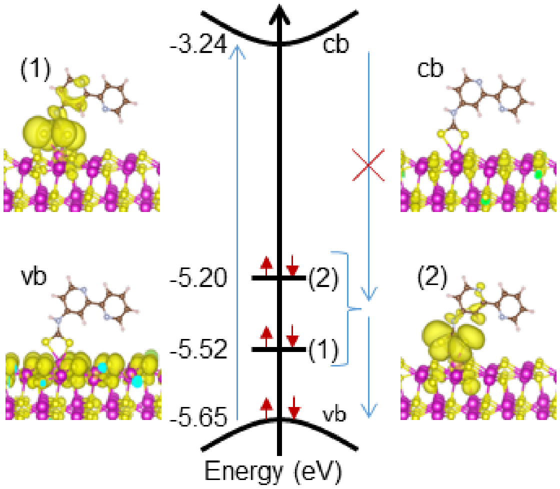

(b) DTCBipyFe(acac)$_2$ level alignment

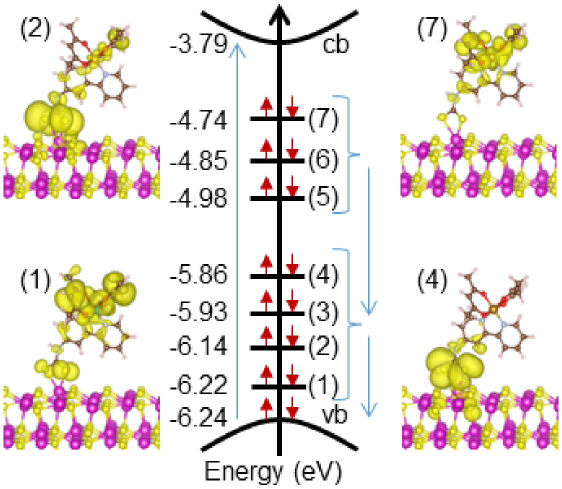

Figure 2.3. Level alignment and Charge Densities of System ;(a) DTCBipy and (b) DTCBipyFe(acac)$_2$ on the CdS surface. For DTCBipyFe(acac)$_2$, only the three levels (1, 2, and 4) with the fastest calculated hole transfer rates from the CdS VB as well as the highest mid-gap state (7) are shown (see Supplementary Information for all). The arrows indicate the different optically allowed transitions between levels. Reprinted (adapted) with permission from refrence 69. Copyright 2017 American Chemical Society.

intramolecular excitations from the mid-gap states to unoccupied ligand molecular states above the CB. The transitions between the VB and DTCBipyFe(acac)$_2$ mid-gap molecular states are dipole allowed. The oscillator strength of these transitions was used to calculate a hole transfer time to a single ligand of 303 ns. As above, if the rate is adjusted for the experimental ligand density, a hole transfer rate is 137 ps is calculated. This represents an increase of 22% in rate versus the non-metal center chelated form. In addition to the transitions from surface states to the ligands, tunneling from the quantum dot to the metal chelating ligands is in theory possible and the rate can be comparable,[83] further enhancing the quenching of the quantum yield. Again, these rates are two orders of magnitude faster than band edge recombination of CdSe/CdS.

The four lower DTC-dominated molecular states predominantly account for the hole transfer rate from CdS to DTCBipyFe, rather than the upper three Fe d-orbital dominated molecular states. Therefore, we calculated the transition rate between the upper three and lower four molecular states and found that the transfer rates are either similar or an order of magnitude faster compared to the initial transfer from the VB to the lower four states. This indicates that a hole can be transferred from the CdS VB to the upper Fe-based mid-gap states through a two-step process in which the initial transfer from the semiconductor to the ligand is rate determining. The ability to transfer the hole to the Fe is important for future applications to photocatalytic oxidation at the metal site.

After Andrew O’hara’s computational work showed promise for hole removal, synthetic work was undertaken to make the system.

2.3 Synthetic Detail

2.3.1 Coupling Attempts

Multiple attempts at the synthesis of a suitable 2,2'-bipyridine ligand were made before arriving at the final DTC used in this work. Initially the deprotonation of 5,5'-dimethyl-2,2'-pyridine by lithium diisopropyl amide was attempted, but a lack of reactivity and availability of a pure enough CO_2 source rendered these attempts futile (**Figure 2.4a**). It was suspected that since CO_2 was not available from a cylinder and had to be generated in situ from dry ice, moisture was being allowed into the reaction and quenching the generated base. This was shown as only starting material was ever recovered from the reaction.

Attempts at coupling functionalized pyridine rings were then investigated, as this method would lead to greater control over the final product. For instance, the ability to place functional groups in a way so that the metal catalyst was either closer or further away from the NP surface could be beneficial in later experiments. In one attempt, 5-nitro-2-chloropyridine was reduced to 5-amino-2-chloropyridine over iron, followed by protection of the amine with a benzylideneamine protecting group. Protection of the amine was deemed necessary due to concerns of the free amine chelating any metal catalyst present in the coupling reaction. A Negishi coupling was then attempted using the protected amino pyridine with 2-chloropyridine utilizing $NiBr_2(PPh_3)_2$ as a cross-coupling catalyst, but no reactivity was observed.[101] These reactions can be seen in **Figure 2.4b**. It was deemed likely that this was due to inactivity of the zinc as used in the experiments, so experiments were then focused on ensuring an active organozinc compound was being produced

Activation techniques were focused on ensuring active zinc was being produced and the metal was inserting in to the aryl-halide bond. Initially a method using Zn activated with 1,2-dibromo ethane and trimethylsilyl chloride and accelerated with the addition of LiCl was attempted on 2-bromopyridine and 3-iodopyridine,[102] but analysis by gas chromatography (GC) indicated that no reaction was occurring. Another method was then attempted using lithium metal and naphthalene as an electron shuttle with $ZnCl_2$ to insert Zn into 2-bromopyridine,[103–105] and traces from GC indicated the formation of a peak attributed to the organozinc compound (**Figure 2.4c**). This compound was then used in Buchwald couplings using $Pd(PPh_3)_4$ and different phosphorus ligands (**Figure 2.4d**), but no ^1H NMR peaks above 9 ppm relating to a bipyridine molecule were observed.[106] To exhaust possible reaction mechanisms which could produce the desired coupled product, a Suzuki coupling using either a purchased phenylboronic MIDA ester and Butyloxycarbonyl (Boc) protected 3-amino pyridine or 2-pyridylboronate and 2-bromopyridine with $Pd(PPh_3)_4$ was run with similar results (**Figure 2.4e**).[107–109] It was concluded from these results that the reaction substrate, pyridine, must be interfering with the metal catalysts by chelating them and quenching reactivity. Alternative routes to producing the 4-amine-2,2'-bipyridine were sought.

A)

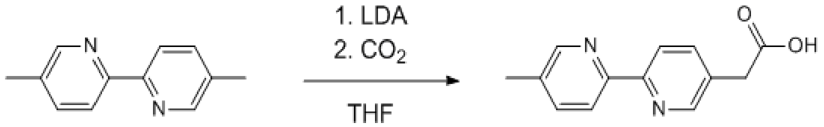
N
N
1. LDA
2. CO_2
THF
N
N
O
OH

B)

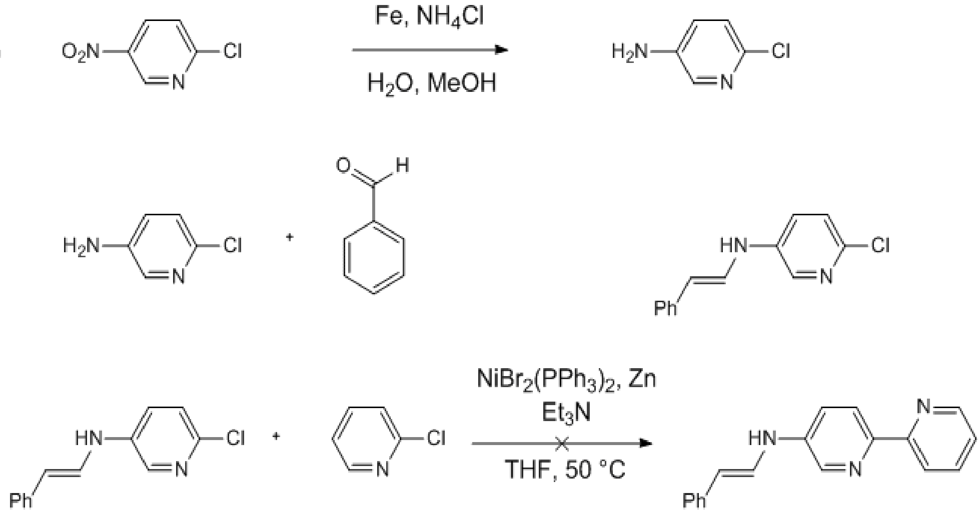
O_2N
N
Cl
Fe, NH_4Cl
H_2O, MeOH
H_2N
N
Cl
H_2N
N
Cl
+
O
H
HN
N
Cl
Ph
HN
N
Cl
Ph
+
N
Cl
$NiBr_2(PPh_3)_2$, Zn
Et_3N
THF, 50 °C
HN
N
N
Ph

C)

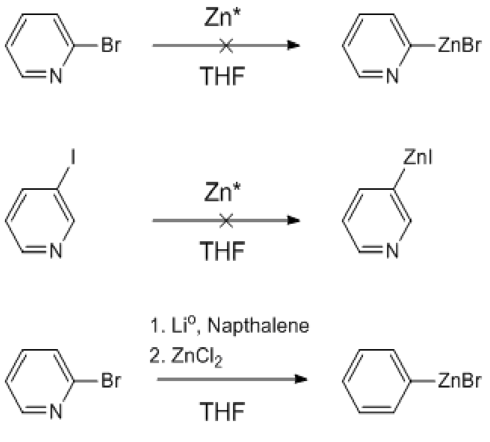
N
Br
Zn*
THF
N
ZnBr
I
N
Zn*
THF
ZnI
N
N
Br
1. Li^o, Napthalene
2. $ZnCl_2$
THF
ZnBr

D)

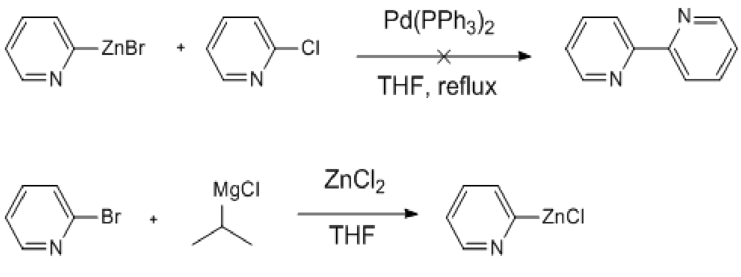
N
ZnBr
+
N
Cl
$Pd(PPh_3)_2$
THF, reflux
N
N
N
Br
+
MgCl
$ZnCl_2$
THF
N
ZnCl

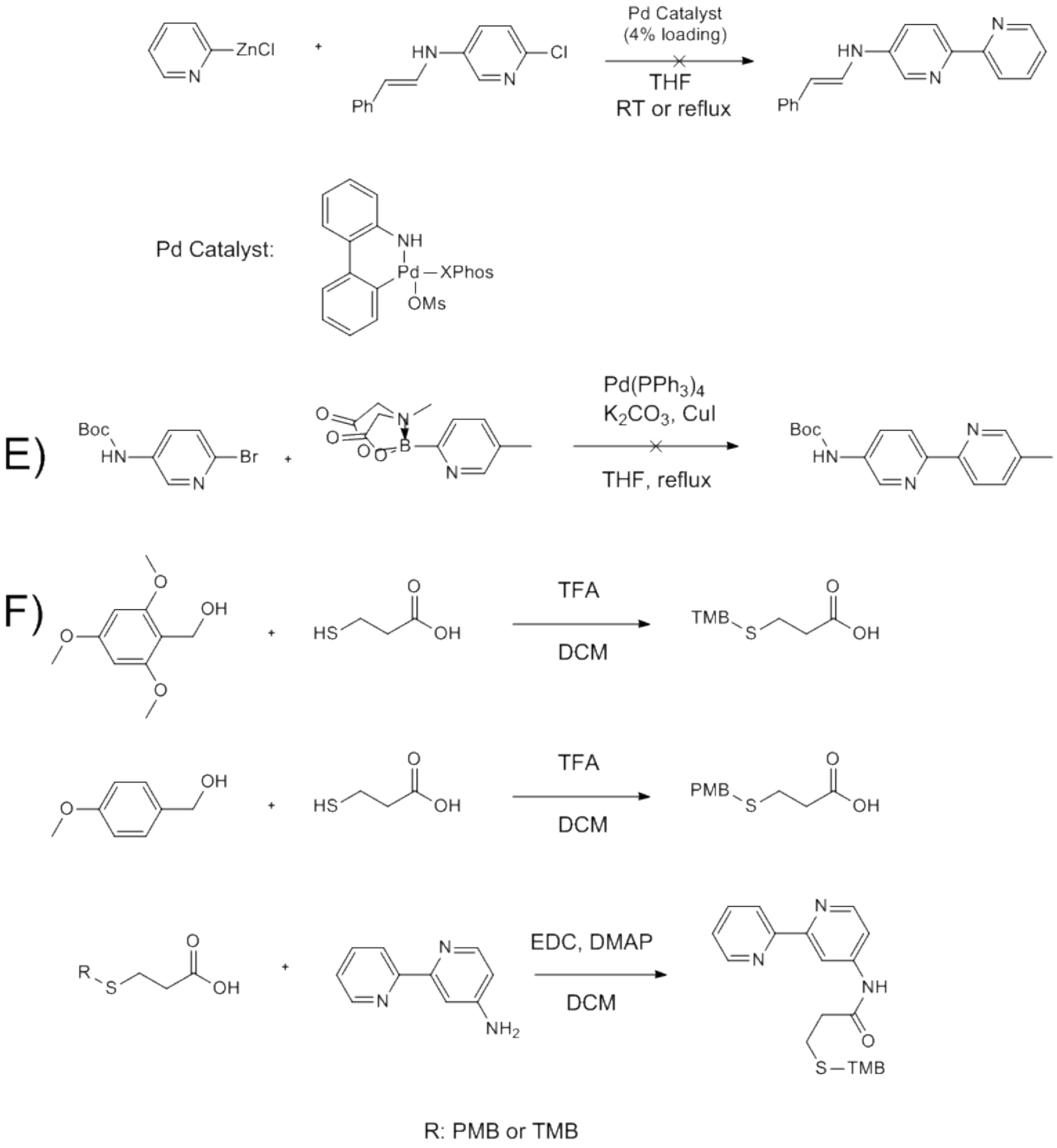

Figure 2.4 Attempted Coupling Syntheses. A) Carboxylation of 5-methyl-2,2'-bipyridine. B) Reduction of 5-nitro-2-chloropyridine to 5-amino-2-chloropyridine, followed by benzylidene protection and attempted Negishi coupling with $NiBr_2(PPh_3)_2$. C) Activation of pyridyl halides to organozinc halides. D) Buchwald couplings using $Pd(PPh_3)_4$ and phosphorus catalysts. E) Suzuki coupling with MIDA-ester. F) MPA protection followed by EDC coupling to amino bipyridine.

A separate set of experiments was run with the goal of coupling the later synthesized amine (vide infra) to 3-mercaptopropionic acid (3-MPA) in order to create a very stable bond which could covalently attach to the NP surface as shown in **Figure 2.4f**. To do this, the sulfur group of 3-MPA was protected with tri-methoxybenzyl (TMB) protecting group,[110] followed by an 1-ethyl-3-(3-dimethylaminopropyl)carbodiimide (EDC) coupling to produce the corresponding amide. While this coupling was successful, it was abandoned due to difficulty in removal of the TMB group. Other protecting groups for MPA were employed for the sulfur group including benzoyl, p-methoxybenzyl, and benzyl ether. The acid group was also activated by conversion to the acid chloride to no avail. In all of these experiments the molecules suffered from lack of reactivity or difficulty in removal of the sulfur protecting group. Once a successful synthesis and ligand exchange protocol for DTCBipy was developed, research focus was shifted to other areas.

2.3.2 Successful Synthesis and Exchange

Prior to successful chelation of DTCBipy on the surface of CdSe/CdS, control experiments based on the work of the Weiss group were performed. This led to an interesting discovery; when attempting to exchange native ligands from either CdSe or CdS seeds with that of DTCBipy, the seeds were no longer in solution as observed by UV-Vis spectroscopy. To investigate the cause of this, the exchange was performed with four different variables: phenyldithiocarbamate (the ligand the Weiss group used), DTCBipy, 2,2'-bipyridine, and a mixture of 2,2'-bipyridine and phenyldithiocarbamate. In these scenarios, dissolution of the seeds was only observed when both a dithiocarbamate group and a 2,2'-bipyridine (which is a strongly chelating ligand) were present. UVVis spectra of this can be seen in **Figure 2.5**. The strongly ligating ligands appeared to etch and dissolve the seeds, and both the DTC and bipyridine moieties are needed to see this effect. While the same phenomenon was not observed with CdSe/CdS rods (likely due to more stable surface chemistry of the CdSe/CdS rods due to the lower surface energy of the larger rods), it is worth noting that the initiation of ligand exchange and presence of Bipy may affect the surface chemistry of NPs.

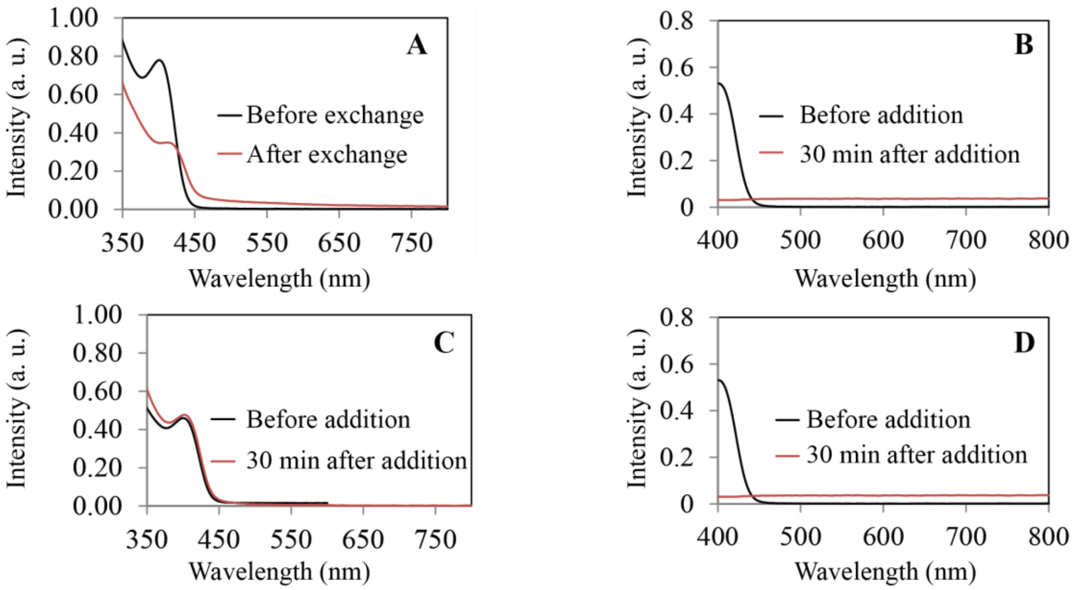

Figure 2.5. Dissolution of CdSe Controls Black denotes NP before organic treatment, while red denotes after. All exchanges were performed using the same concentrations as performed by Weiss et. al. A) Phenyldithiocarbamate B) DTCBipy C) 2,2'-bipyridine D) Phenyldithiocarbamate and 2,2'-bipyridine. Reprinted (adapted) with permission from refrence 69. Copyright 2017 American Chemical Society.

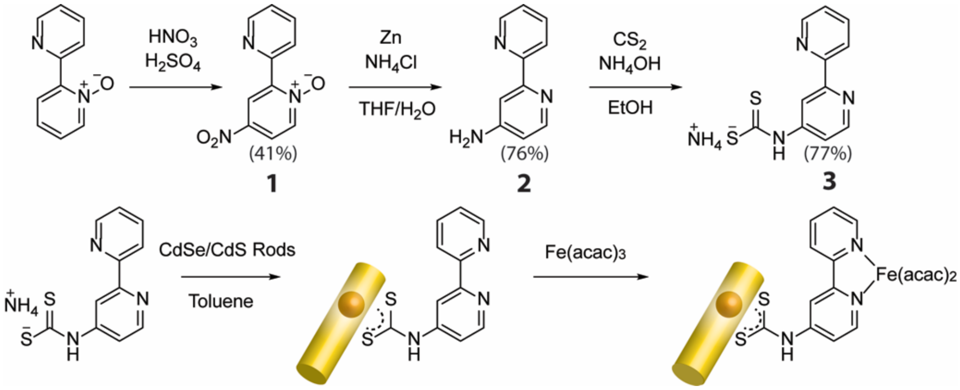

Figure 2.6. Synthetic Scheme; Synthesis of ammonium-[2,2’-bipyridin]-4-ylcarbamodithioate, via nitration, reduction, and nucleophilic acyl substitution of 2,2’-bipyridyl n-oxide, ligand exchange onto CdSe/CdS NRs and coordination of Fe(acac)$_3$. Reprinted (adapted) with permission from refrence 69. Copyright 2017 American Chemical Society.

Given the promising theoretical predictions, experiments were designed to synthesize and study the proposed ligand system. The successful synthesis of the ligand ammonium-[2,2’-bipyridin]-4-ylcarbamodithioate **(Figure 2.6**, **3**) was completed *via* the nitration of commercially available 2,2’-bipyridine N-oxide to 4-nitro-[2,2’-bipyridine] 1-oxide (**1**).[111] Reduction to 4-amino-2,2’bipyridine (**2**) was performed over Zn dust.[112] The reaction of this amine with carbon disulfide in the presence of ammonium hydroxide[113] yielded the desired dithiocarbamate as an ammonium salt (**3**). CdSe/CdS NRs were grown *via* a seeded growth approach as reported elsewhere **(Appendix A.**1.). [114]

Ligand exchange of DTCBipy onto CdSe/CdS NRs was performed by adding a solution of **3** in toluene to NRs in toluene and stirring in the dark under Ar for 16 h. A concentration of 4.5 ligands/nm^2 was determined experimentally to be optimal for surface saturation. In order to complete the conjugation of a metal center to the CdSe/CdS rods, a solution of $Fe(acac)_3$ was added to the DTCBipy coordinated CdSe/CdS rods (**Figure 2.6**, detailed experimental procedures available in SI). An additional absorbance feature appeared, peaking at 541 nm. This absorbance matches that of a free solution of DTCBipy and the iron precursor without the presence of the NRs. This absorbance also matches the computational absorbance profile of $DTCBipyFe(acac)_2$ (**Figure A.3** and **Figure 2.7**) and the presence of crisp ^1H NMR peaks further indicates diamagnetic low spin Fe(II) (**Figure A.5**).

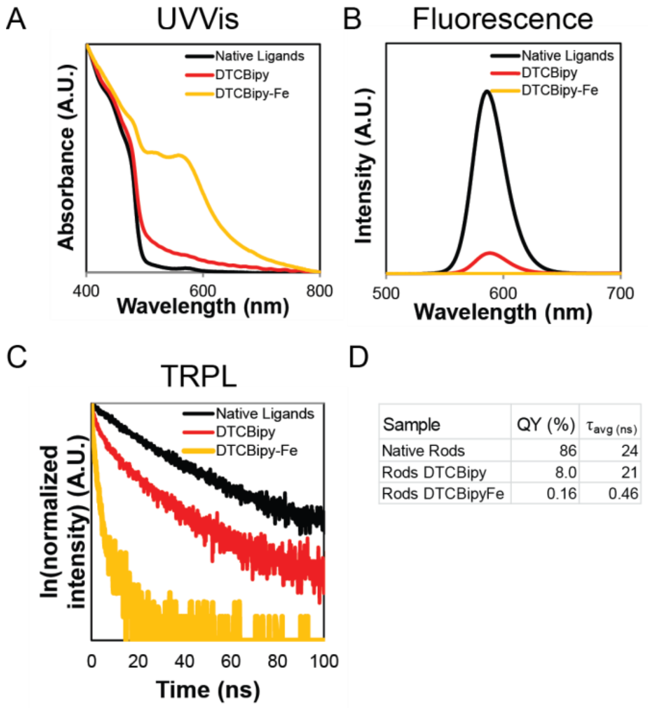

Sample	QY (%)	$\tau_{avg\ (ns)}$
Native Rods	86	24
Rods DTCBipy	8.0	21
Rods DTCBipyFe	0.16	0.46

Figure 2.7. Spectroscopic Analysis;A) UV/Visible spectrum of CdSe/CdS NRs with native ligands (black), after ligand exchange with DTCBipy (red), and subsequent treatment with Fe(acac)$_3$ (gold) B) Fluorescence spectroscopy of NRs C) TRPL of NRs (see supplementary information for parameters). D) PL and TRPL data. Reprinted (adapted) with permission from refrence 69. Copyright 2017 American Chemical Society.

2.4 Spectroscopic Analysis

Scanning transmission electron microscopy energy dispersive X-ray spectroscopy (STEM)-EDS mapping visualizes the distribution of Fe on the NRs (**Figure 2.8**). An additional wide field image (STEM)-EDS map of DTCBipyFe ligand exchanged rods is available in the SI (**Figure A.7**). Control experiments where Fe(acac)$_3$ was mixed with NRs ligated with native ligands did not show any association between Fe and the NRs

(**Figure A.6**). Quantitative EDS (**Table A. 1.**) of 10 different areas of sample revealed an average Fe signal of 2.41± 0.32 Fe atoms per nm^2 of nanoparticle surface area were present. Since the amount of Fe added was 4.5 ligands/nm^2 and this is greater than 2.41 ligands/nm^2, this number shows persistence of the Fe only when bound to DTCBipy.

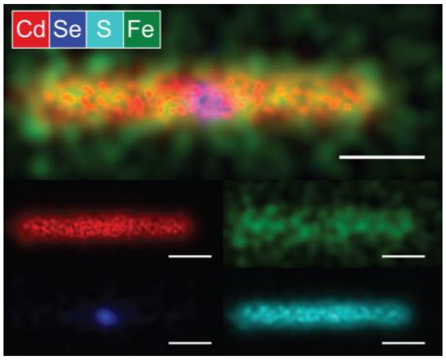

Figure 2.8. STEM-EDS map. CdSe/CdS rod ligand exchanged with DTCBipy then treated with Fe(acac)3. Scale bar is 10 nm. The overall picture omits S for clarity. Reprinted (adapted) with permission from refrence 69. Copyright 2017 American Chemical Society.

Experimental validation of the predicted hole transfer from the NR to the ligands was performed by analyzing the samples via steady-state and time-resolved (TR) photoluminescence (PL) spectroscopy. Given the band alignment of CdSe/CdS, only fluorescence from the CdSe core can be observed. Ligand exchange of native ligand NRs with DTCBipy (**Figure 2.7**) resulted in a large quench in QY from 85% to 8.0% , which was observed previously for DTC containing ligands.[89] This is consistent with our prediction that hole transfer from the CdS to DTCBipy is facile and prevents radiative recombination of excitons. Formation of the DTCBipy-Fe complex caused a further quench in the QY to 0.16%, as expected since hole transfer was calculated to be even faster once Fe was coordinated. This QY quench was over a factor of ten larger than that seen by only adding Fe(acac)$_3$ to a solution containing native ligand capped NRs (**Figure A.9**.). The latter is likely due to charge trapping at a small amount of Fe adsorbed to the surface, as was similarly observed by Shevchenko *et. al.* in the case of CdSe/CdS mixed with Au.[115] Similar QY quenches were observed when exciting primarily the CdSe core, which denotes that the charge transfer process is primarily surface mediated. (**Figure A.10**.).

In collaboration with Kemar Reid from the lab of Sandra J. Rosenthal, TRPL data was acquired for the synthesized system and details regarding the laser parameters can be found in the **Appendix A**. Fits of the TRPL data for the CdSe/CdS NRs capped with native ligands showed a τ_{avg} of 23.5 ns for the fluorescence of the CdSe core, which is in good agreement with those reported elsewhere in literature.[116] The bi-exponential decay (**Figure A.10** and **Figure A.11**) was assigned to band edge recombination and a small amount of trapping of charges to surface states. Upon ligand exchange with DTCBipy, τ_{avg} decreased slightly to 20.9 ns (**Figure 2.7**). The combined large QY quench and consistent lifetime dynamics indicates that the holes are mostly extracted from the photoexcited CdS rod to the ligands before they can be localized to the CdSe core. The VB offset of CdSe is 0.55 eV from the CdS VB,[114] and sits above the mid-gap states so they are not accessible for hole transfer from the CdSe core. Upon chelation of Fe to the surface coordinated DTCBipy ligand, τ_{avg} quenches to 455 ps (**Figure 2.7**) and is best fit by a tri-exponential decay with time constants of 133 ps, 1.24 ns, and 15.03 ns. While directly assigning these pathways to specific processes is difficult, a lifetime of 1.24 ns is similar to those reported for intrinsic CdSe core recombination,[117] and the 133 ps component is similar to our calculated value for transition from the CdS to the ligand molecular states. The 15.03 ns component is of very low contribution to the weighted average (**Figure A.13**). We note that the 133 ps process is significantly longer than the sub-picosecond hole transfer times experimentally measured by the Weiss group for a conjugated DTCBipy ligand.[88] This can be expected as the driving force reported for the sub-picosecond hole transfer ligand is -1.2 eV, while in the DTCBipy system the driving force for transfer from the CdS to the molecular ligand state is much smaller, as it was calculated to only be between -0.02 to -0.38 eV.

2.5 Conclusions and Future Directions

Unfortunately, studies concerning the oxidation of water using DTCBipy were curtailed by the realization that the ligand, DTCBipy, was itself sensitive to moisture. It is known that dithiocarbamates are sensitive to degradation in acidic medium due to protonation of the amine group which results in the release of carbon disulfide.[118] In this case degradation was observed when DTCBipy was dissolved in pyridine (a basic solvent) and water added to χ=0.2 of H_2O. The observed effect was the return of fluorescence in CdSe/CdS rods which were previously quenched (see **Figure A.16**), and the occurrence of a putrid smell due to released CS_2. This prompted further studies to be carried out in anhydrous conditions, and ligand to be stored under argon in the freezer in between experiments.

In summary, we have modeled and synthesized a CdSe/CdS NR system with an organic ligand capable of electronically coupling with the energetics of the NR while chelating a molecular metal center. DFT studies revealed the presence of two hybridized mid-gap molecular states on CdS in the presence of DTCBipy; these states show promising calculated hole transfer rates between CdS and DTCBipy with minimal recombination *via* the CB. The experimental quench in quantum yield supports this prediction, though these experiments alone cannot entirely rule out the existence of trapping or separation caused by other pathways.[30,119,120] The chelation of Fe(II) by this complex resulted in seven mid-gap states. The calculations indicate that the rate of hole trapping should further increase and proceed most efficiently by a two-step process from the CdS to the DTC group orbitals, followed by a faster transition to the Fe center. The measured hole transfer time is slower than those seen for other DTC based ligands,[88] but comparing the energetic driving forces of the processes the transfer time follows the expected trend. One of the potential advantages of this conjugated ligand design is that transitions from the ligand mid-gap states to the CdS CB are dipole forbidden, which in the future should facilitate slow oxidative catalytic processes to occur on the metal center, rather than facile recombination with the electron. The assembly of this system indicates great potential in the use of light as a renewable driving force for oxidative and reductive processes in a single colloidal nanoparticle system.

Chapter 3

3 MULTI-STEP LIGAND EXCHANGE ON P-TYPE QUANTUM DOTS FACILITATES HIGH-PERFORMANCE SOLAR CELLS

Upon absorption of light, semiconductor NPs generate an exciton pair that can be used to perform a chemical reaction, as discussed previously, or separated and transported to different materials, as occurs in a solar cell. This chapter will discuss an idea which was developed in our lab concerning the fabrication of solar cells. Quantum Dots (QDs, NPs under quantum confinement) are used in QD solar cells as a photo-absorber. This requires film deposition followed by either a solid-state exchange or chemical treatment of surface ligands. In our lab, a new ligand utilizing the Fmoc protecting group was synthesized and tested as a ligand for colloidally stable PbS QDs. Devices were fabricated and tested through collaboration with James Fan and Kevin Yang from the Sargent group at the University of Toronto. Devices constructed utilizing the facile deprotection mechanism of Fmoc-coated PbS films produced higher efficiency solar cells in comparison to control devices.

3.1 Introduction

Solution-processed colloidal QDs have attracted much interest over the past decade as they offer attractive characteristics for optoelectronic devices such as photovoltaics (PVs),[6] photodetectors,[121] lasers,[122] and light-emitting diodes.[123] Among the attractive properties of this type of material are the low cost of fabrication, the ability to tune the bandgap of the desired material for specific applications, and a high absorption per unit length.

Much attention has been paid in recent studies towards improving QD active layers in PV devices. Comparatively, there has been little focus on the fabrication of the hole transport layer (HTL). [124–129] In the earlier generation of PbS PV devices, the typical HTL consists of a MoO_x/Au/Ag anode.[124,130,131] In this type of device, the MoO_x is sputtered onto the PbS active layer and Au and Ag are sequentially thermally deposited on top of the $MoO_{x.}$ The MoO_x serves as an ohmic contact to the Au layer, facilitates hole transport, and protects the PbS active layer from the noble metal evaporation process.[130] These types of devices have power conversion efficiencies (PCE) up to 9.5%.[131] In recent years, the choice of material has been switched to a solution processable layer such as PbS QDs functionalized with a short chain thiol (e.g., 1,2-ethanedithiol (EDT)).[132] In comparison to MoO_x, EDT-PbS also provides an ohmic contact between Au, and this HTL can be processed in ambient conditions. The band positions of halide-passivated PbS-active layers is deeper than that of EDT-PbS QDs, therefore using EDT-PbS QDs as an HTL provides a band offset that offers hole transport while blocking electrons.[132,133] Devices with EDT-PbS HTLs have recently exhibited PCEs that exceed 10%.[125,127,134]

The EDT-PbS layer is typically prepared through a solid-state ligand exchange approach.[135] An oleic acid (OA)-capped PbS (OA-PbS) film is prepared by spin-coating PbS QDs on top of a PbS active layer; ligand exchange is performed by soaking the film in an EDT solution. This process is generally repeated twice to yield a HTL PbS thin film, and from henceforth will be referred to as EDT/EDT-PbS.[135] This ligand exchange process, however, may disturb the QD surfaces. It has been reported that during the exchange process, the detachment of $Pb(OA)_2$ species may occur and result in QDs with etched, fused, or oxidized surfaces.[136,137] In addition, unreacted free thiol groups (R-SH, R = alkyl or aryl chains), as opposed to thiolates ($R\text{-}S^-$), may form oxidation products in an ambient environment.[138] Therefore, a facile method to introduce non-charge-insulating ligands is highly desired.

It has been previously shown that a homogeneous ligand exchange can be performed directly after the synthesis of QDs in a one-pot reaction.[138] During the cooling stage, alkanethiol capping ligands are injected into the reaction flask to undergo ligand exchange in the nonpolar phase.[139140] This method of homogeneous ligand exchange is gentle to the surface because the QDs are not exposed to air during this process, and the aggregated QDs are easily precipitated away from the free OA ligands in solution during the purification process.[141] However, the direct injection of bifunctional EDT molecules during the synthesis stage will cause crosslinking and aggregation of the PbS-QDs, resulting in a colloidally unstable solution.[128] The QDs must remain suspended post-synthesis in a homogenous suspension to allow the deposition of a uniform film.

This work builds upon strategies by Turo et al.,[142] which placed long chain esters within a molecule that stabilized nanoparticles in a homogenous colloidal solution while also providing further functionality via the ability to hydrolyze the ester to an acid. The fluorenylmethyloxycarbonyl (Fmoc) protecting group has been commonly used in solid state peptide synthesis where it is cleaved using a gentle organic base treatment.[143–145] Fmoc was attached asymmetrically to EDT to produce the molecule O-((9H-fluoren-9-yl)methyl) S-(2-mercaptoethyl) carbonothioate (FMT) (**1**) (**Figures B.1 and B.2**). We hypothesized that the FMT ligand would exchange with surface OA ligand, forming FMT-

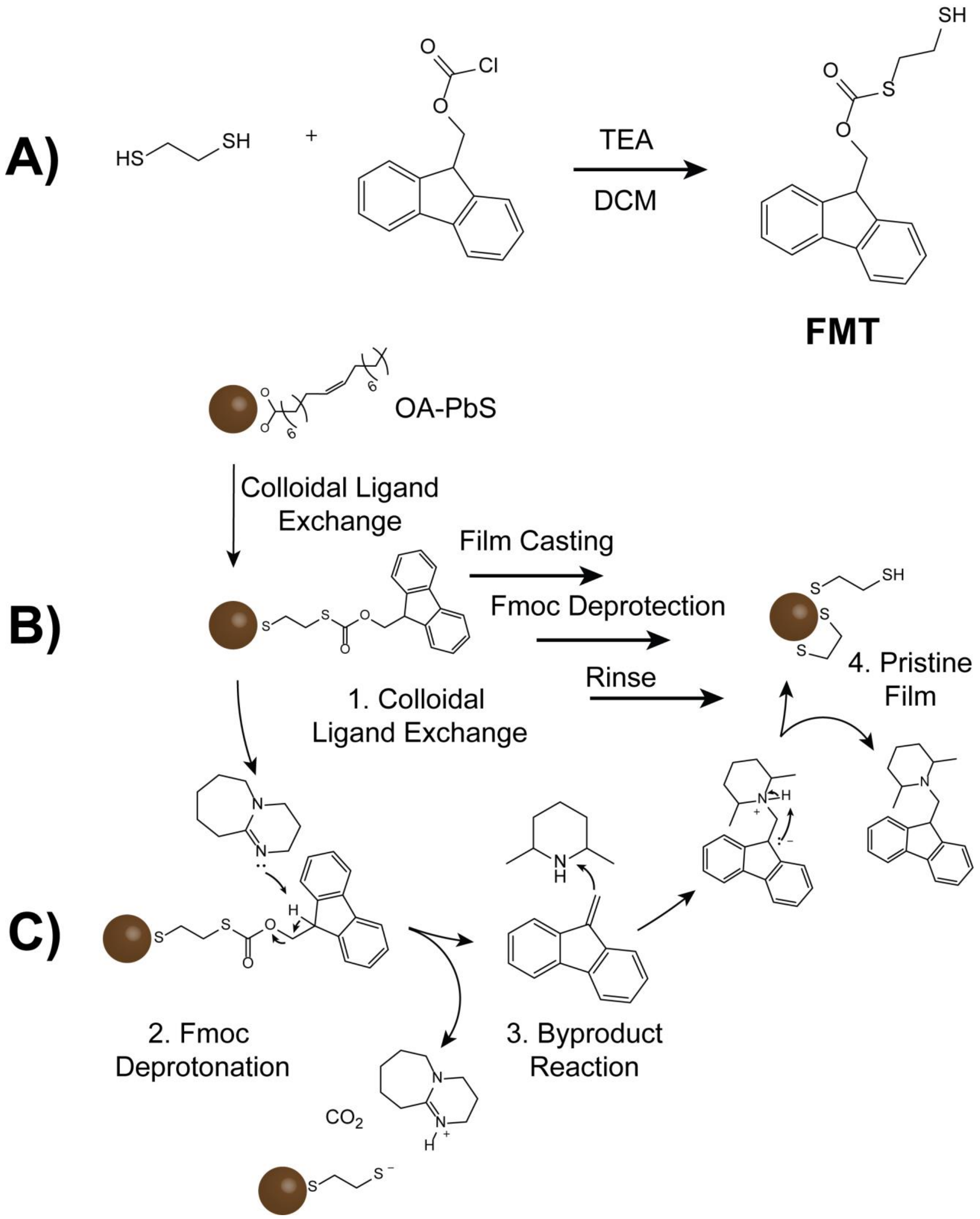

Figure 3.1. Ligand Synthesis and Device Fabrication; A) Synthesis of FMT. B) Schematic illustration showing PbS thin film formation. Pristine oleic acid (OA)-capped PbS is exchanged in solution with FMT. After the cleavage with a facile base, byproducts are removed leaving behind only EDT. C) Mechanism of Fmoc deprotection.

passivated PbS QDs. Molecular DFT calculations for FMT and EDT can be seen in

Figure B.8 and indicate that the electron donating HOMO of the FMT is ~.5 eV higher than that of EDT. This places the HOMO of FMT closer to that of the valence band of PbS (~ -6.14 eV), allowing for a stronger bonding interaction.[146] These initially long bulky ligands enabled the FMT-PbS QDs to be colloidally stable in a non-polar solvent, and yielded smooth and uniform thin films from spin coating procedures. Following film deposition, the FMT was cleaved by a mild base to produce a high quality EDT-PbS QD film as shown in **Figure 3.1**.[143] FMT syntheses as well as initial ligand exchange and cleavage conditions were developed in the Macdonald lab, and FMT was shipped to the Sargent lab for further device preparation and characterization. We applied the film preparation strategy to fabricate QD PVs and studied the effect of different bases upon the QD surfaces during the Fmoc deprotection. We will denote the cleaved FMT-PbS film as cFMT-PbS as the nomenclature for the rest of this manuscript. The EDT-capped PbS QD prepared by the traditional direct soak method will simply be denoted as EDT-PbS.

3.2 Ligand Synthesis and Film Fabrication

In designing a ligand tailored for the application of an uniform film, the Fmoc protecting group presented itself as the optimal choice since it 1) can be combined with the commonly used EDT, 2) provides colloidal stability for the QDs after homogenous ligand exchange, 3) can be cleaved with a mild base that does not interfere with the QD surfaces, 4) can be synthesized on the gram scale in a scale-up one-step synthesis, 5) is a short ligand which facilitates dense QD packing, and 6) deprotection of the ligand forms byproducts that are electronically and chemically inert to the QD surfaces, in particular avoiding carboxylic acids which have been shown to be problematic in PbS photovoltaics.[65] The mechanism of deprotection for an Fmoc protecting group is detailed in **Figure 3.1**. Briefly, the most acidic proton residing on cyclopentyl ring within the Fmoc protecting group is first deprotonated by a mild base. This causes the electrons to break the dibenzofulvene bond, therefore forming the unstable carbonothioate in solution, which quickly decomposes into CO_2 and EDThiolate. The dibenzofulvene byproduct is a highly reactive nucleophile which then reacts with a nearby electrophile to form an inert molecule. In this report, 1,8-diazabicyclo(5.4.0)undec-7-ene (DBU), was used in catalytic amounts to perform the initial deprotonation of the Fmoc group, while dimethylpiperidine (DMPpy) was used as a sterically hindered electrophile for reaction with the dibenzofulvene adduct.[143]

The synthesis of OA-PbS has followed the procedure reported by Hines and Scholes[147] and was slightly modified for this study (see Supplementary Information). Briefly, Pb-oleate is generated in situ via the dissolution of PbO in OA. At a temperature of 63 °C a mixture of trimethylsilyl sulfide in ODE was swiftly injected, and the reaction was allowed to cool to room temperature before purification via precipitation with acetone. A ^{1}H NMR of OA-PbS particles can be seen in **Figure B.3** which shows the alkene protons from the oleic acid attached to the QD surface. FMT-PbS solutions were prepared by ligand exchange of FMT on to the PbS surfaces via the dropwise addition of a solution of FMT in $CHCl_3$ to OA-PbS suspended in $CHCl_3$. The QDs were precipitated with acetone until no alkene peak from OA could be observed in the ^{1}H NMR upon resuspension in $CDCl_3$ (**Figure B.4)**. Only very broad, weak signals from bound FMT were observable due to surface broadening effects from the PbS surface.[39] To make the FMT-PbS solution

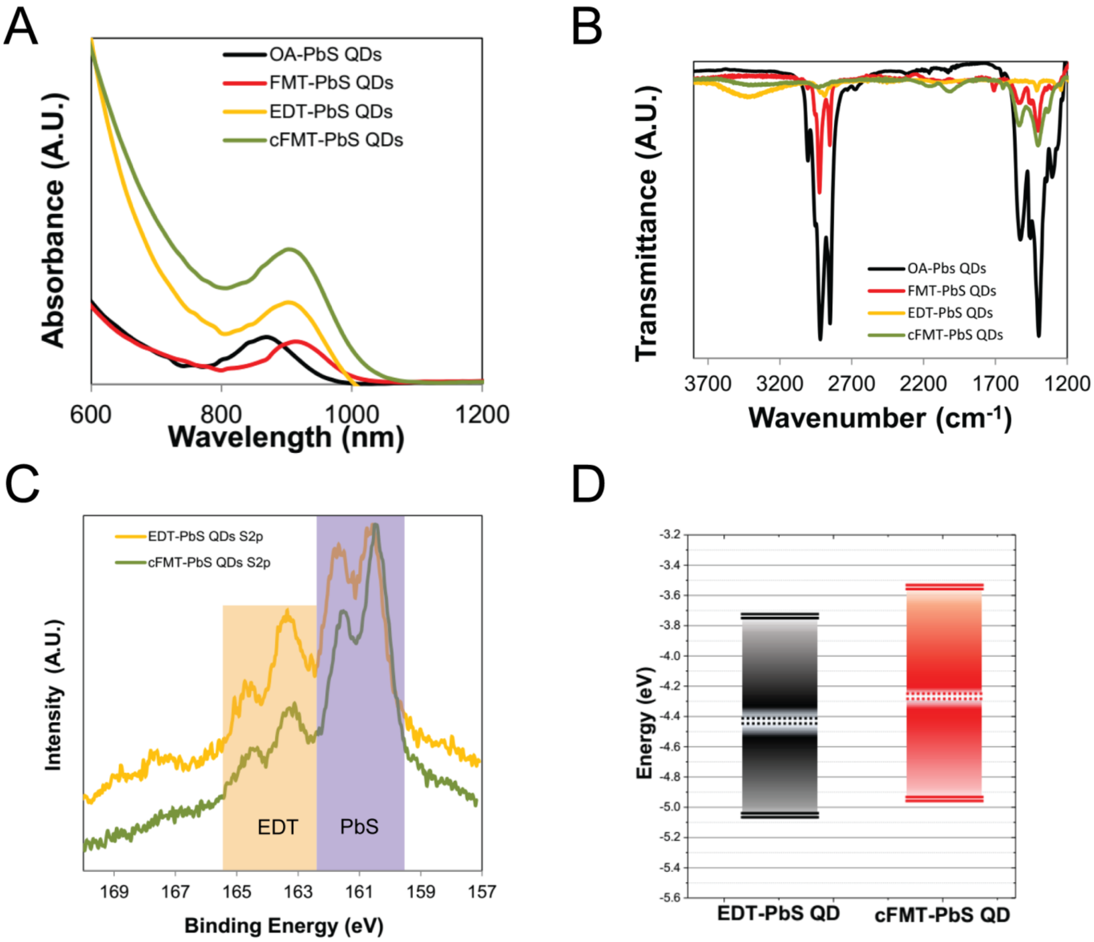

Figure 3.2. Optical Spectroscopies of PbS films; A) Absorbance spectra of QD films: OA-PbS (black), FMT-PbS (red), EDT-PbS films made by the conventional method (yellow), and cFMT-PbS films (green). B) FTIR spectra QD films: OA-PbS (black, scaled to one third intensity for comparison), FMT-PbS (red), EDT-PbS films made by the conventional method (yellow), and cFMT-PbS films (green). C) XPS sulfur 2p spectra comparing the EDT-PbS film (yellow) and cFMT-PbS film (green) D) Band structure determined by UPS and absorbance results comparing the band alignments of an EDT-PbS film (black) and a cFMT-PbS film (red).

ready for device fabrication, the FMT-PbS precipitate was dissolved in octane at 50 mgmL^{-1} to yield thin, uniform, spin coated films. While the FMT concept, synthesis and exchange was developed personally in the Macdonald lab, the ligand was shipped to

James Fan of the Sargent group where he carried out ligand exchange, film deposition, and film characterization as well as device fabrication.

Fmoc cleavage or EDT ligand exchange was performed on the respective films, and surface analysis techniques were used to verify the fulfillment of a complete “on film” reaction. Similar absorbance values for both FMT-PbS and OA-PbS films suggest that both have similar thicknesses. The FMT-PbS film is red-shifted compared to OA-PbS as has been observed for other systems upon ligand exchange.[148] The absorbance of both films increased after their conversion to cFMT-PbS or EDT-PbS QD films (**Figure 3.2a**). Previous studies have suggested that the optical density of PbS films increases after ligand exchange reactions when the exchanged QDs are more densely packed.[149] When comparing the two absorption spectra in **Figure 3.2a**, it is evident that the optical density increased significantly more for cFMT-PbS QD films than the EDT-PbS counterpart, indicating a higher packing density of the QDs. The denser packing and stronger absorbance at the exciton peak is also reflected later in the External quantum efficiency measurements of the prepared devices (*vide infra*) (**Figure 3.3d**).

Fourier transform infrared (FTIR) spectroscopy reveals a decrease in organic content after each QD functionalization. In particular, the C-H stretches (2850-3000 cm^{-1}) were reduced successively between OA-PbS, FMT-PbS and cFMT-PbS. A broad –OH peak appears at 3500 cm^{-1} for the EDT-PbS QD film which can be attributed to the

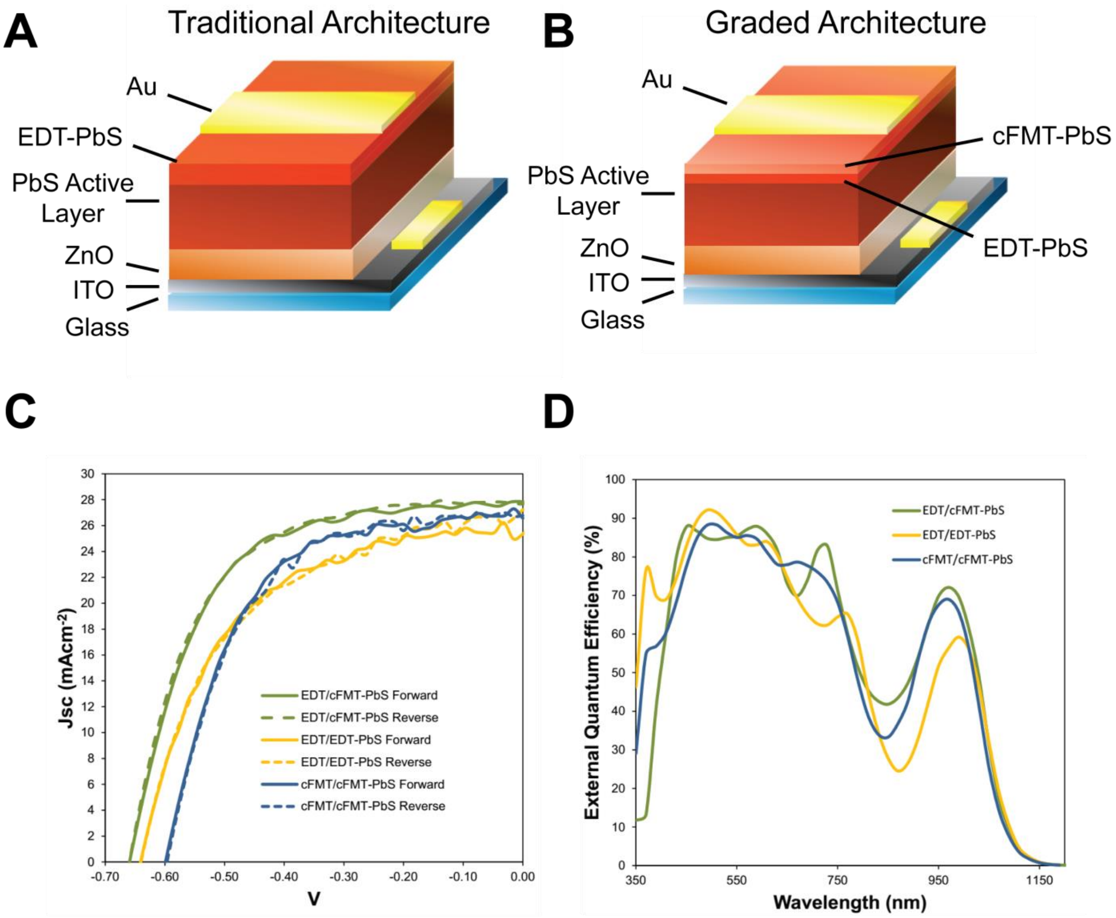

Figure 3.3. Devices Structure and Data; A) Solar cell architecture using only the conventional EDT exchange method. B) Solar cell architecture utilizing both the traditional EDT exchange method and the FMT exchange method. C) *J*-*V* curves for FMT-colloidal QDs (black) and traditional OA-colloidal QDs (grey). D) External quantum efficiency measurements comparing the devices fabricated with an FMT-colloidal QD and traditional OA-colloidal QDs.

fabrication process of EDT-PbS; the direct soak EDT solvent, acetonitrile, is hydrophilic which allows for atmospheric moisture to be absorbed into the film.[150] A complete decrease in the carbonyl peak can be seen when comparing the OA-PbS to the EDT-PbS. However, the carbonyl peak remains in the cFMT-PbS sample compared to the FMT-PbS.

The shape of this peak changes, and is reflective of that reported for bicarbonate which could be produced from CO_2 in the basic cleavage environment.[243]

X-ray photoelectron spectroscopy (XPS) measurements were used to determine the surface composition of the EDT-PbS and cFMT-PbS QD films (**Figure B.5**). The spin orbit coupled sulfur $2p_{3/2}$ and sulfur $2p_{1/2}$ peaks appearing at around 160.4 eV and 161.7 eV shown in **Figure B.5c** matches closely to that of PbS.[128] The pair of peaks at 163.5 and 164.7 eV corresponds to thiolates of EDT bound to the PbS surface. It is worth noticing that the normalized intensities of peaks originating from EDT are of much greater intensity for the EDT-PbS compared to the cFMT-PbS, suggesting more ligand is present in EDT-PbS film, consistent with the tighter packing of QDs in cFMT-PbS noted by the absorbance measurements above. The cleavage procedure may avoid the introduction of excess non-functional ligand into the films. The peaks in the Pb4f and C1s spectra of both films match closely **(Figure B.5a and d)**. Again, both films show in the oxygen 1s spectra expected lead oxide species due to air exposure at 530.7 eV,[151] but an additional large peak at 532.6 eV was only observed for the EDT-PbS films, which is attributed to lead oleate species.[152,153] The presence of carboxylate indicates an incomplete EDT ligand exchange and/or oleate removal during the fabrication of the direct soak EDT film. The lack of a carboxylate signal on the cFMT-PbS O1s spectra suggests that the homogeneous ligand exchange successfully displaced all of the oleic acid.

The electronic properties of a cFMT-PbS QD film and its traditional EDT-PbS counterpart were analyzed using ultraviolet photoelectron spectroscopy (UPS) (**Figure 3.2d and B.6**). The determination of the valence band maximum, conduction band minimum, and Fermi level for each films are discussed in detail in the experimental section. The bandgaps for the EDT-PbS QD film and the cFMT-PbS QD film were 1.35 eV (λ_{ex} = 918.5 nm) and 1.41 eV (λ_{ex} = 880 nm), respectively. The position of the bandgap for the EDT-PbS QD film matches well with those reported in literature, while the cFMT-PbS film measurements showed a shallower band position than EDT-PbS.[132,133] For these similarly sized QDs, it was surprising that the band position of the cFMT-PbS QD film exhibited a band position that is higher in energy than the EDT-PbS QD film. This is likely due to a previously observed ligand effects, as EDT capped QDs are known to produce a more p-type QD film than OA capped QDs.[154] Given that OA was shown to remain in the films using the EDT direct soak method, it is likely that the complete removal of OA through the FMT approach produces a more stongly p-type film lifting the band position. The shallower position of the conduction band as seen in the cFMT-PbS QD film may allow for further electron blocking when used as a hole transport layer in a typical inverted QD solar cell. A good electron blocking layer will decrease the chance of charge recombination at the Au contact, and successfully transport holes to the anode. [132,134,155]

3.3 Device Fabrication and Characterization

To illustrate the advantages of the solution processed cFMT-PbS QDs, we used this approach to construct a HTL for solar cells. A traditional PbS solar cell architecture is indium doped tin oxide (ITO)/zinc oxide (ZnO)/PbS-Active layer/EDT-PbS/Au (**Figure 3.3a**).[125,132,134] The specific method for producing the ZnO electron transport layer and PbS active layer has been discussed in previous literature.[134] In the conventional QD PV device, two layers of solid-state exchanged EDT-PbS (50 nm in total) were applied onto the top of the active layer to serve as the HTL[132]. Herein, we replaced the traditional HTL with our cFMT-PbS layers while keeping the rest of the device architecture unchanged.

To evaluate the quality of the fmoc cleavage approach to the preparation of the HTL in a device scenario, the FMT-QDs were cleaved using a mixture of DBU and a second weaker base. In this reaction, DBU is used as a catalytic base, while the second base acts as a nucleophilic "sponge" to remove the dibenzofulvene byproduct.[143] The solar cell figures of merit, open circuit voltage (V_{oc}), short circuit current density (J_{sc}), fill factor (FF), and power conversion efficiencies (PCEs) are listed in **Figure 3.4** for three base treatment protocols. A large variation of PCEs were observed when the byproduct "sponge" was changed, and performance of these devices were compared to the control device. The control device utilizes EDT/EDT-PbS QDs for the HTL and had a PCE of 9.43%. When FMT-PbS HTLs were soaked with only a 1% v/v DBU solution and no secondary base, a device with a PCE of 7.8% was produced. The combination of low V_{oc}, J_{sc}, and FF indicate that the device has poor band alignment and poor charge extraction. We hypothesize the reduction in performance is due to residual DBU, dibenzofulvene, or uncleaved Fmoc left within the film even after the washing procedure. According to the mechanism in **Figure 3.1**, DBU is responsible for performing the initial deprotonation leading to cleavage of the Fmoc group. However, as a non-nucleophilic base, it will not readily react with dibenzofulvene, and steps of the cleavage may reverse and therefore produce an incomplete cleavage. While the addition of a nucleophile to the treatment protocol is therefore needed, careful consideration must be given to the base sterics and electronics. When the base/nucleophile combination of aa 1% solution of 9:2 v/v 2,6-lutidine and DBU were used to remove the dibenzofulvene byproduct, a device was produced with a PCE of only 5.8%. Unfortunately, the electron rich nitrogen group of 2,6-lutidine likely performs a ligand exchange with the QD surfaces, similar to those seen previously with butylamine.[156–158] The 2,6-lutidine as a surface ligand may diminish charge transport between QDs, lowering the overall performance of the device. Due to this issue, we hypothesized that a similar base with a bulkier side chain may actually avoid ligand exchange on the surface of the QDs due to steric hindrance but still be able to react with the small dibenzofulvene. Therefore, the choice of 2,6-ditertbutylpyridine (DTP) was a good replacement over the smaller 2,6-lutidene. For this specific device, the optimized concentration of 1% 9:3 v/v DTP:DBU was employed. This device exhibited a noticeably higher J_{sc} over the other FMT-based devices (27 mA/cm^{-2} vs. 20mA/cm^{-2}), and an overall PCE of 9.56%. External quantum efficiency (EQE) measurements reveal that the cFMT-PbS QD devices are enhanced mainly in the height of the exciton peak (**Figure 3.3d**). The overall performance of the cFMT/cFMT-PbS (9.56%) was slightly greater than that of our EDT/EDT-PbS device (9.43%).

From UPS studies as seen in **Figure 3.2**, there was evidence that band positions of the cFMT-PbS QD films are shallower than the EDT-PbS counterparts. Therefore, a graded HTL architecture designed as EDT/cFMT-PbS was employed as seen in **Figure 3.3**. Graded HTLs architectures can create an energy landscape that facilitates hole transport and have been used previously to improve the efficiency of PbS-QD solar cells by effectively extending the depletion width in the main absorber layer.[135159] In this scenario, instead of spincoating two OA-PbS layers followed ligand exchange to EDT after each application, one EDT-PbS layer is fabricated in this traditional manner followed by the addition of an FMT-PbS layer which is then cleaved with base (DBU) and nucleophile

(2,6-dimethylpiperidine, DMPpy), a base chosen for its improved ability to react with dibenzolfulvene due to its lack of aromaticity. The base used for the FMT-cleaved QDs was a mixture of 30:1 DMPpy:DBU. A device produced in this fashion yielded a performance of 11.01%. Most noticeably, this device retained the high V_{oc} from a pure directly soaked EDT/EDT-PbS QD device, while maintaining a high *FF* value. The external quantum efficiency (EQE) plots reveal enhancements at the exciton peak for both the EDT/cFMT-PbS and EDT/EDT-PbS QD devices (**Figure 3.3d**).

Functionalization solvent	V_{oc} (V)	J_{sc} (mA/cm^2)	$FF_{forward}$ (%)	$FF_{reverse}$ (%)	PCE (%)
DBU only	0.58	20.77	66.02	65.30	7.80
9:2 v/v 2,6-lutidine: DBU	0.56	20.58	54.07	51.17	5.88
9:3 v/v DTP:DBU	0.60	26.96	59.72	58.53	9.56
EDT-PbS control	0.63	26.29	57.89	56.01	9.43
Graded: 1 Layer EDT-PbS + 1 layer 30:1 v/v DMPpy: DBU	0.66	27.41	60.65	61.14	11.01

Figure 3.4. Figure of Merit for Solar CellsFigure 4.1. Mechanism of NB Degradation;

3.4 Conclusions

In conclusion, a high quality EDT-functionalized PbS QD film was produced through an alternative protection and deprotection step of EDT. The native OA ligands of PbS were completely exchanged in solution and removed by a novel FMT ligand to yield colloidal FMT-capped QDs. These FMT-QDs were used to construct the hole transport layer. The Fmoc protecting group of the FMT ligand was easily removed by a mild base treatment, and a pristine EDT-PbS film was produced. A film with denser QD packing, fewer EDT-ligands, fewer carboxylate-impurities and more p-type character was produced through the FMT cleavage method than the traditional EDT ligand exchange method. The effectiveness of this hole transport layer was tested in the fabrication of a QD solar cell, and yielded power conversion efficiencies greater than the traditional EDT-PbS counterpart. By developing a graded device architecture by using the first direct soak-counterpart and then a cFMT-PbS QD film, a QD device with a performance of over 11% was fabricated. This work provides important insight into the necessity of improving the HTL and highlights the role that chemistry on the surface of QDs affects their electronic properties.

This work illustrates the necessity of collaboration to advance scientific ideals. Though the original idea of utilizing FMT for solar cells was born in the Macdonald lab, researchers with specialization in device fabrication were needed to bring the idea to fruition. After the ligand had been synthesized and initial ligand exchange conditions optimized, workers in the Sargent group were able to use the ligand to make films, make devices, and characterize devices. Intellectual contribution was thus split in two different fabrication steps, then combined at the end for data interpretation.

Chapter 4

4 CONCEPT AND PRELIMINARY WORK: LIGHT SENSITIVE LIGANDS

As discussed in the previous chapter, one of the major challenges of utilizing QDs for solar cells involves the processing of ligands (either through introduction in colloidal phase or solid state) for a densely packed film. Surface ligands must be exchanged from charge insulating ligands to short ligands which permit charge transfer; this is typically done in the solid state and suffers from issues in either case. Performing a ligand exchange on a film can cause disturbances to the QD surface, while reaction cleavage on the QD surface may be incomplete or leave behind electronically active impurities. The following section will outline the concept of using light-degradable ligands for ligand cleavage, followed by a summary of completed work.

4.1 Introduction and Background

The use of light as a catalyst for bond breaking or fission has been studied for a variety of applications across multiple fields. In the field of biology, photo-activated reactions have played a large role in the development of systems which allow for real-time monitoring of cell environments through photo-responsive hydrogel material.[160–162] Another technique which has garnered significant interest is "biocaging" in which a bioactive molecule or marker is "tagged" and can be released once delivered to a specific area of interest. For instance, polyethylene oxide materials were developed which form micelles that burst upon UV radiation,[163] and other photolabile biocompatible protecting groups have been synthesized which degrade upon UV or IR light absorption.[164–166] Further research into two-photon biomarker deprotection for reduction in background noise in biological imaging is also a topic of interest to the community.[167] These accomplishments have opened up their own area of research in biology; however, the use of photochemistry for colloidal QD device fabrication remains unexplored.

Light has been used in photochemistry as a clean catalyst in various reactions. Some of these include photocycloadditions and rearrangements,[168,169] redox reactions,[170,171] and organometallic reactions.[172,173] The chemistry has been applied to the field of materials science to create reactive polymers which degrade upon light irradiation,[174–176] as well as polymers that will form a gel and expand under UV irradiation through the presence of the o-nitrobenzyl (NB) and the use of click chemistry. [177] Crucial to this is the o-nitrobenzyl group (NB) which was first introduced as a photoactive protecting group for peptides by Woodward and coworkers in 1970.[178] NB has since seen a large application in biological and materials uses as the active group is simple to install on many molecules, stable to most conditions except extremely alkaline or acidic environments,[179,180] and produces relatively benign byproducts after NB activation and removal.[181–188] While possessing these qualities, it was reported by Woodward and co-workers that complete cleavage as determined by gas chromatography (GC) occurred within 1-24 hours of irradiation.[178] Other groups expanded on the possibility of monitoring for uncaging or deprotection by UVVis absorption,[181] proton NMR,[186] and HPLC,[189] and synthetic schemes were devised to greatly increase the rate of deprotection.[166,183,184,186] The current proposed photo-degradation mechanism is shown in **Figure 4.1**. Briefly, the aromatic benzene ring is excited by UV radiation, causing cyclization with the nitro group resulting in the formation of nitrosobenzaldehyde and protonated leaving group. This degradation applied to molecules synthesized here can be seen in **Figure 4.2a**.

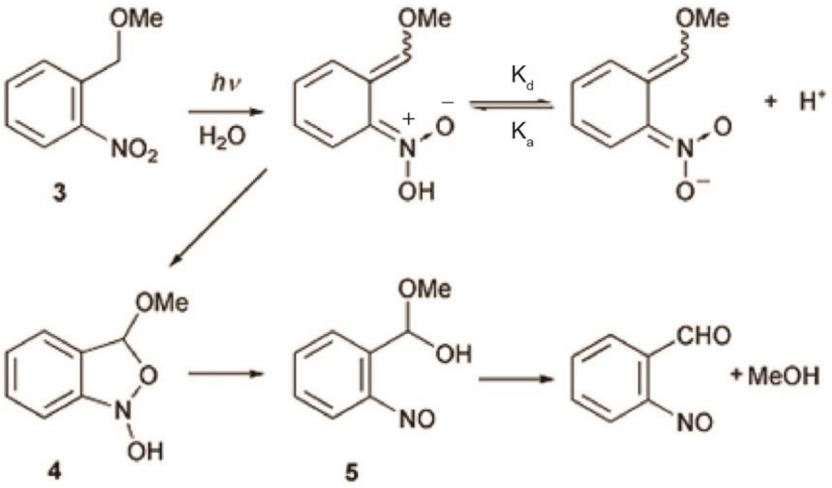

Figure 4.1. Mechanism of NB Degradation; Pathway of degradation of NB including equilibrium state of nitro group. In this case, the “protected” functional group was methanol. Reproduced from reference 165.

In the design of a ligand containing a group suitable for colloidal QD applications, both EDT and MPA were considered for binding to the QD. In this work EDT is primarily utilized due to the affinity of thiols for CdSe and PbS which are common in device fabrication. The reaction of EDT with a chloroformate precursor possessing the NB tag produces a molecule containing a light sensitive group, carbonate, and thiol which may be readily exchanged with the QD. The produced ligands should decompose under light irradiation to nitrosobenzaldehyde and 2-mercaptoethylcarbonothioate, which will quickly decompose to produce EDT and carbon dioxide.[190] An illustration of this can be seen in

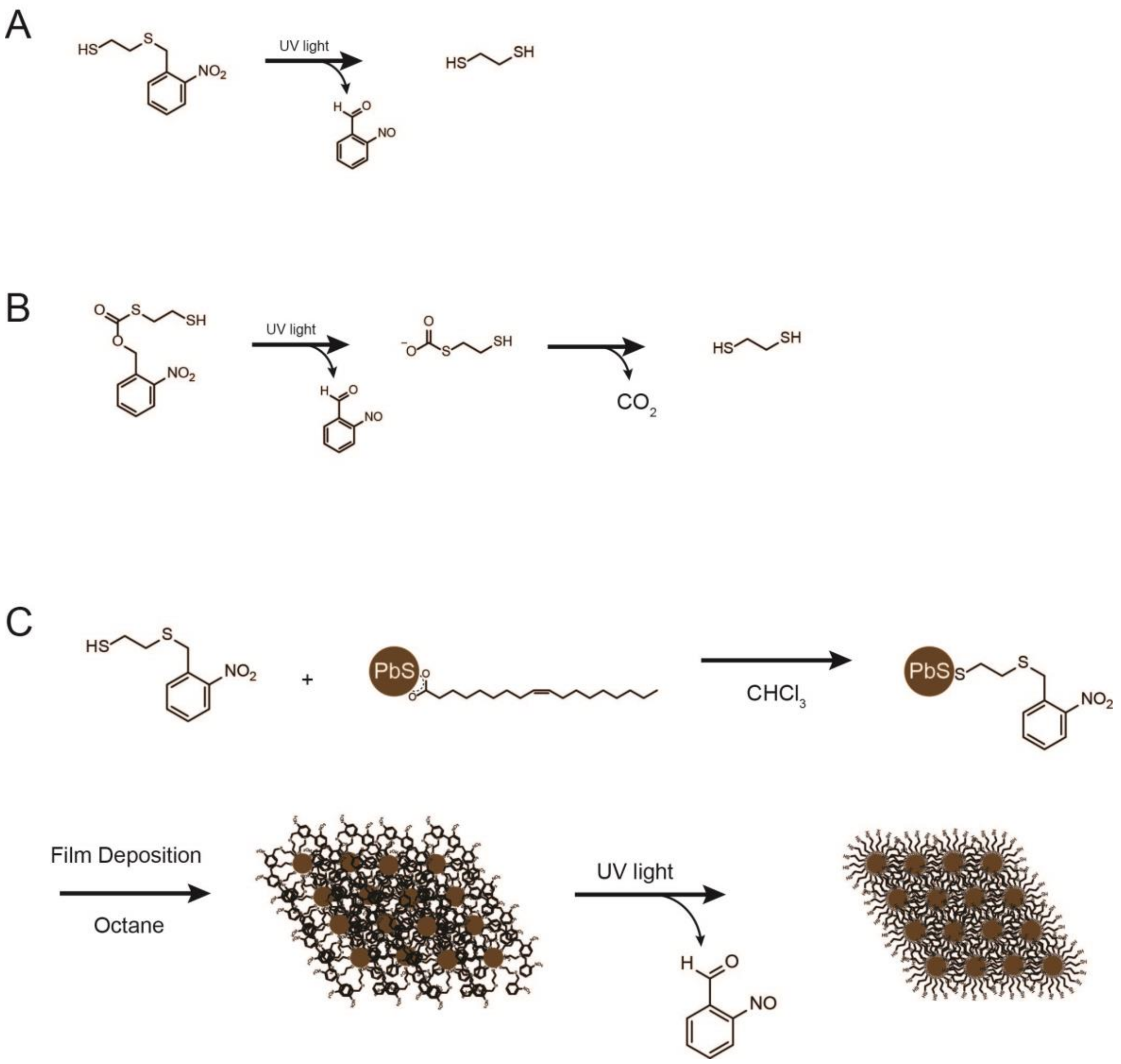

Figure 4.2. Degradation and Fabrication Pathways; A) Degradation of monofunctionally NB protected EDT. B) Degradation of monofunctionally NB protected thiocarbonate-EDT. C) Deposition and degradation of PbS.

Figure 4.2b. Studies were also undertaken to synthesize the ligand lacking the thiocarbonate functionality. This methodology minimizes the minimum amount of soluble byproducts produced while also avoiding the need to add other cleavage reagents which may produce other impurities or disrupt the nanoparticle surface. **Figure 4.2c** shows the proposed path to utilizing these types of ligands in a QD film. QDs are first ligand exchanged colloidally, followed by film deposition. Since UV light is the catalyst for degradation, films can then be subjected to light, and byproducts from the reaction can simply be washed away leaving a tightly packed, ordered QD film.

4.2 Synthesis and Degradation

Several reaction pathways were explored to evaluate the application of these types of ligands to QD systems. Initial syntheses involved alkyl chloroformates as they are the simplest starting point, reagents are readily available, their structure mimics that of preciously reported QD ligands.[67,142]. A one-step reaction between the alkyl chloroformate and nucleophile results in the desired ligand in moderate yield. The general reaction scheme for these ligands can be seen in **Figure 4.3a**. After reaction and ligand exchange conditions were optimized, NB ligands were synthesized as shown in **Figure 4.3b and c**. The methoxyl variant of the chloroformate ligand, O-(4,5-dimethoxy-2-nitrobenzyl) S-(2-mercaptoethyl) carbonothioate (DNMC), was synthesized since the onset of absorption is significantly redshifted compared to the variant without methoxy groups, which should allow for lower energy photocleavage.[191] A ligand omitting the thiocarbonate

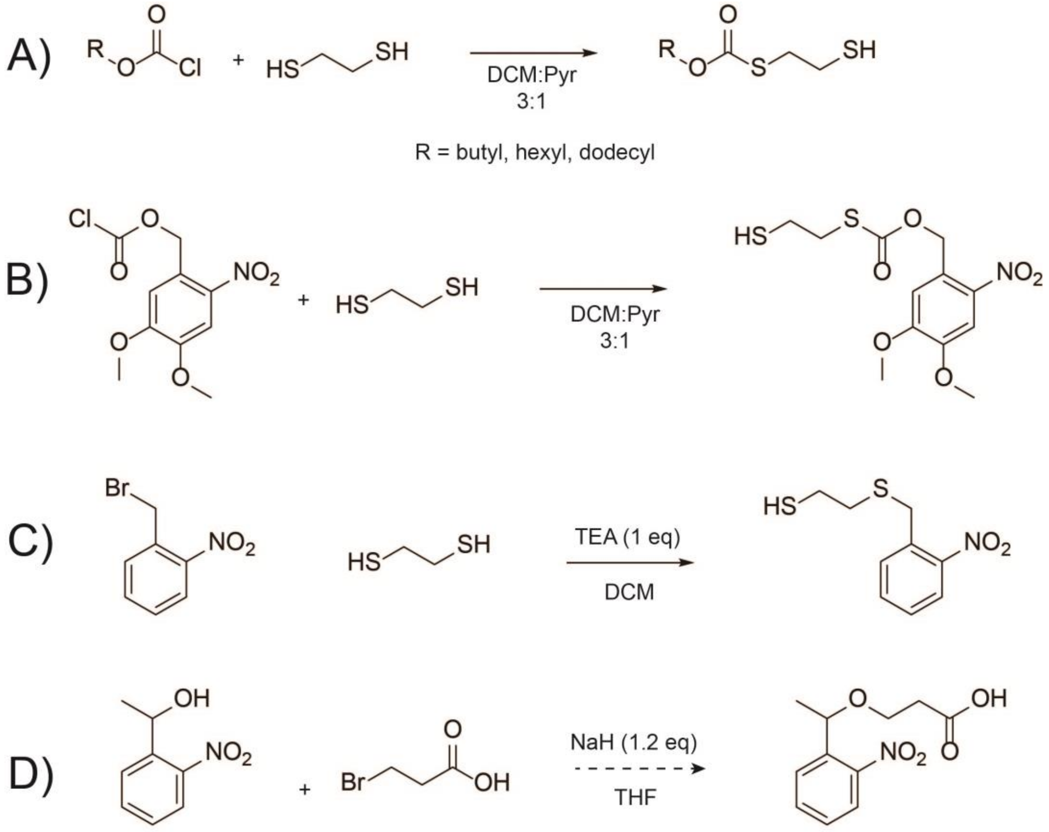

Figure 4.3. Reaction Paths; A) Alkyl thiocarbonates. B) NB thiocarbonate. C) Mono-substituted EDT with NB functionality. D) Mono-substituted 3-hydroxypropionic acid with methyl substituted benzyl position.

functionality, 2-((2-nitrobenzyl)thio)ethane-1-thiol (NET), was also synthesized via a S_N2 mechanism between 2-nitrobenzyl bromide and EDT to study the effects of methyl and thiocarbonate groups on ligand functionality. Further synthetic attempts were aimed at the synthesis of a variant of NB containing a methyl group in the benzyl position, as it has been reported that such substitution drastically improves the rate of decomposition (**Figure**

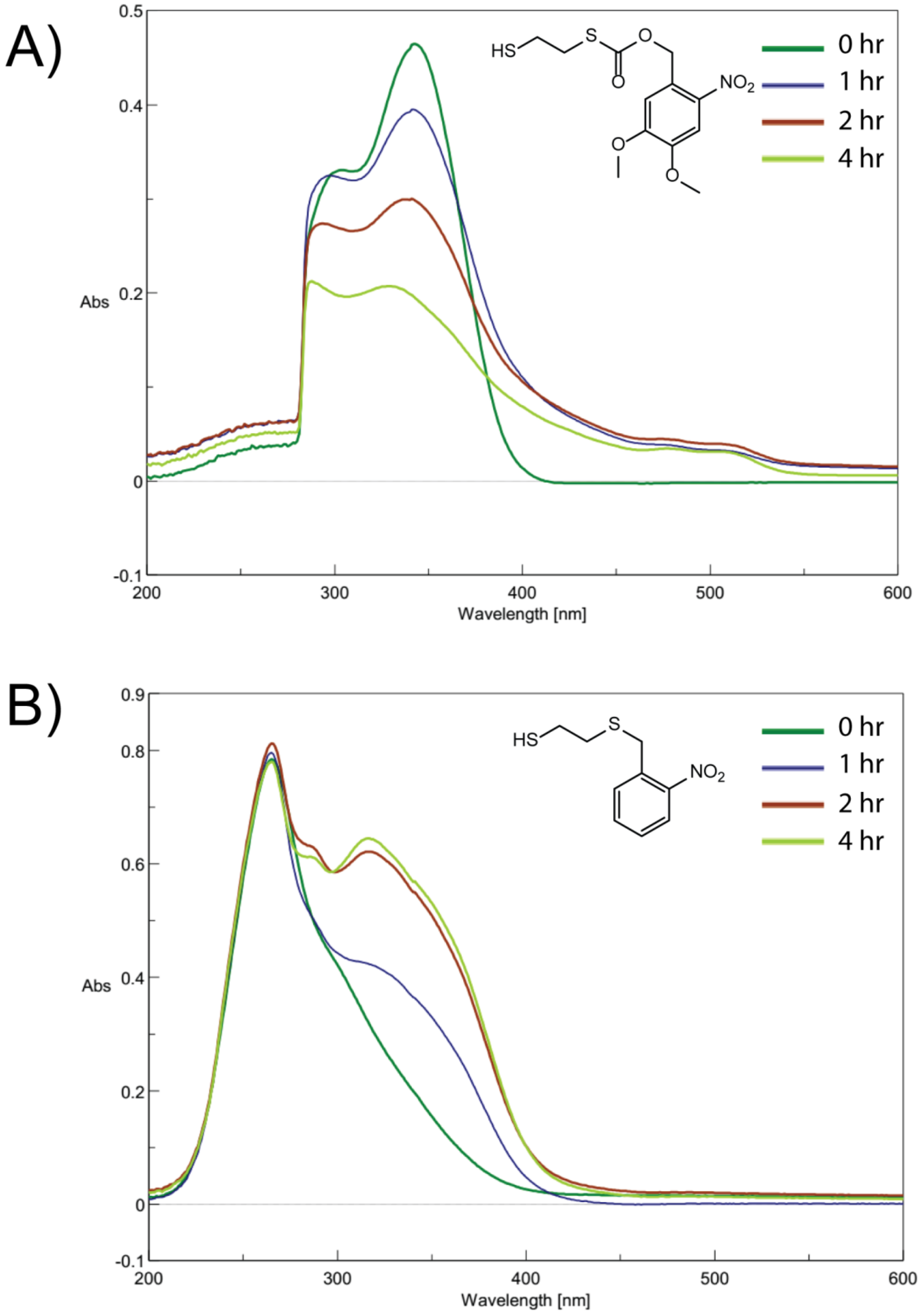

Figure 4.4. UVVis Spectra of Ligand Degradation; A) DNMC. B) NET. Both spectra were recorded in $CHCl_3$ and illuminated with a 4W 254 nm light. Spectra are not normalized.

4.3d).[185,186] While this molecule should provide interesting data, it was not completed within the timeframe of this research. Experimental data concerning these syntheses can be found in **Appendix B**.

A variety of conditions were used to affect the degradation of the ligands which were taken from previously cited literature. For alkyl thiocarbonates, mole fractions of H_2O in THF ranging from $\chi=0.60$ to $\chi=1$,[178] pure isopropanol,[184] or pure chloroform[186,187] for 0.2M concentrations of ligand were tested. When using a 4W UV light, no degradation was seen over 4 hours via GC or NMR spectroscopy. This is in contrast with studies using NB which showed upwards of 50% cleavage within 1 hour.[186] From these studies we concluded the thiocarbonate group alone is not photo-active, and focus was shifted to producing NB containing ligands.

Utilizing the same reaction scheme from alkyl chloroformates, 4,5-dimethoxy-2-nitrobenzyl chloroformate was reacted with EDT to form DNMC (**Figure 4.3b**). This molecule contains a thiocarbonate group connected to the more thoroughly studied photo-labile 2-nitrobenzyl group. When DNMC was dissolved in chloroform and subjected to UV radiation from the 4W lamp, degradation was observed, but not as expected. As shown in **Figure 4.4**, illumination of DNMC over the course of 4 hours causes a degradation of the first molecular transition, as well as appearance of a new transition around ~550 nm. This change in absorbance is saturated by 4 hours. NMR of the solution, however, did not show the symmetric single peak which would be expected from EDT; instead, two sets of peaks were observed, one from DNMC, and another from what is likely an unsymmetrical byproduct (See **Figure 4.5b**). The aromatic region of the spectra still only contains two singlet peaks, so the resulting EDT molecule is unlikely to be the product of the reaction between EDT and the resulting benzaldehyde. Instead, this may be due to the reaction of

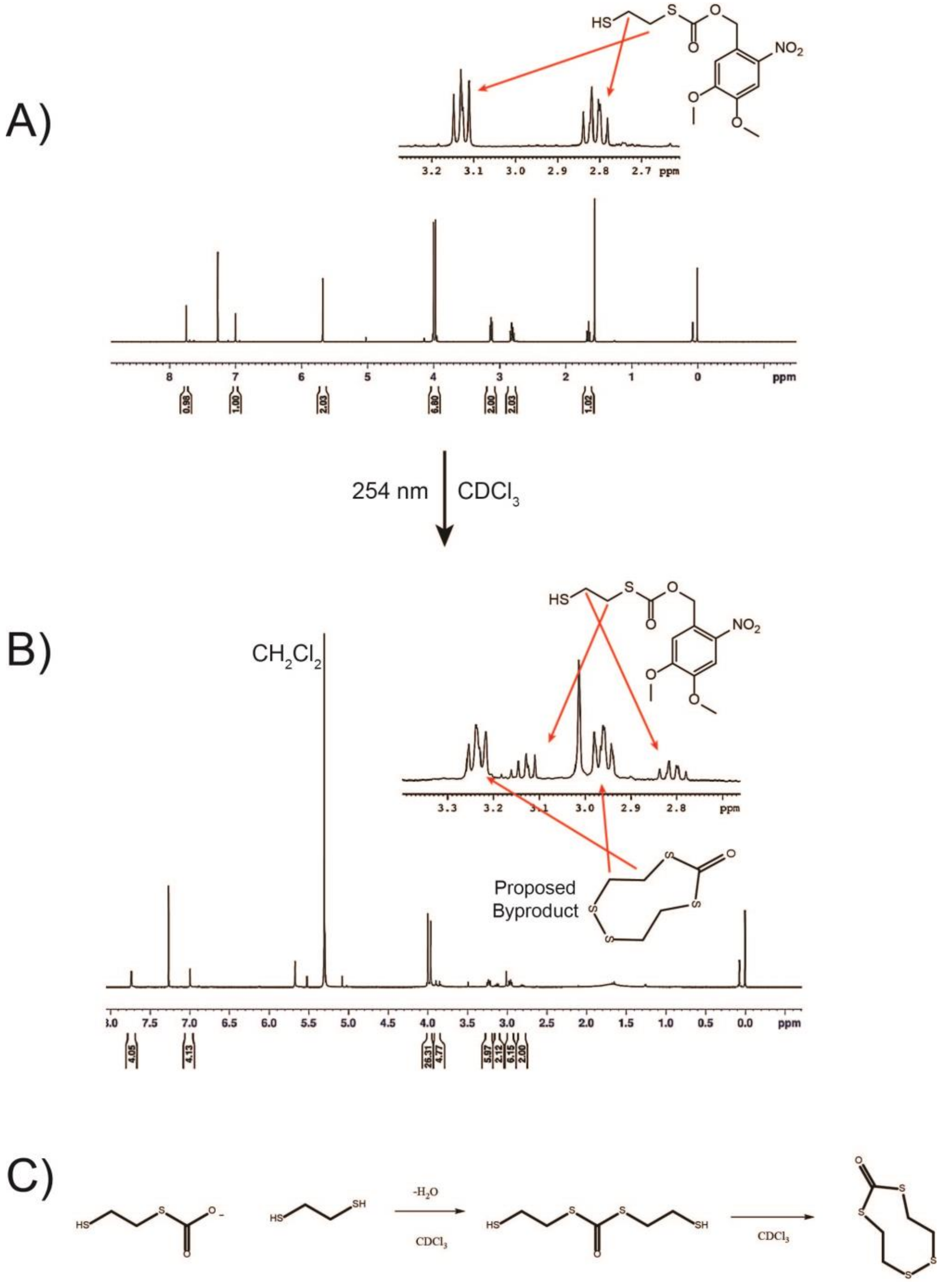

Figure 4.5. NMR of Degraded Products; A) NMR of NB thiocarbonate ligand before irradiation with UV light. B) After 4 hours of irradiation a new set of asymmetrical EDT peaks appear, along with a peak presumably from $CDCl_3$ decomposing to dichloromethane. C) Proposed byproducts from reaction of EDT with thiocarbonate.

the thiol with the intermediate thiocarbonate produced after UV degradation followed by a disulfide oxidation resulting in a ring closure (**Figure 4.5c**). This interpretation is supported by the lack of multiple aromatic species, the presence of a new unsymmetrical EDT compound, and the triplet splitting of the two methylene carbons indicating the presence of only two neighboring protons for each carbon. An additional peak at 5.3 ppm indicated these conditions were also causing the degradation of chloroform to dichloromethane.[192] In an effort to simplify the structure and determine the cause of unexpected reactivity, a molecule was made which omitted the thiocarbonate functionality (**Figure 4.3c**), but similar UVVis and NMR data was observed after degradation. Ligand exchange and subsequent degradation studies were also performed on PbS with DNMC, but NMR data was inconclusive and the strong absorbance of PbS in the UV and visible spectrum occluded any spectral transitions occurring from the ligand. This data, as well as experimental details of the ligand exchange and degradation studies can be found in Appendix B.

Given the lack of precedence in literature for NB ligands containing thiol groups connected to the benzyl position, it is likely that the reactivity of the thiol in the presence of the generated benzaldehyde is forming a hemithioacetal or thioacetal as shown in **Figure 4.6**.[193] Keeping this in mind, as well as implementing a methyl group in the benzyl position to increase photosensitivity and decrease byproduct reactivity, a reaction scheme was devised for 3-(1-phenylethoxy)propanoic acid (PEP, see **Figure 4.3d**). Due to time constraints, synthesis of this molecule was not completed.

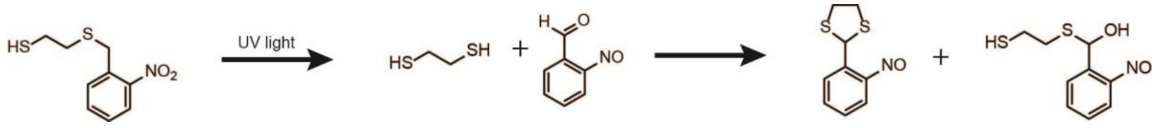

Figure 4.6. Proposed Side Reaction of thiol and aldehyde; The reactivity of the thiol and generated benzaldehyde may be producing either the hemithioacetal or thioacetal products.

4.3 Further Directions

Substantial progress was made towards determining and synthesizing a ligand suitable for photodegradation on colloidal nanoparticles. It was determined that alkyl thiocarbonates are not suitable for photodegradation. Further, thiocarbonates were deemed unnecessary, and perhaps detrimental, in the process of degradation. Their synthesis was useful, however, as degradation studies with NB containing thiocarbonates suggested the reactivity of produced thiols with generated aldehyde, suggesting the uncaging of a thiol while using this particular photolabile protecting group is a poor choice.

Another issue which presented itself through this work is the absorbance of PbS impeding the use of light to degrade the ligands. Other materials which don't absorb as strongly in the visible spectrum, such as CdSe and CdS, or materials which absorb primarily in the UV such as VO_2,[194,195] ZnO,[196] or TiO_2[197] would thus be superior choices for initial studies into implementing photo-functionalized materials for nanoscale devices. These materials would also be superior for ligand exchange with groups other than thiols, allowing for the use of more thoroughly studied photolabile groups which degrade to reveal a hydroxyl or carboxyl group. Further progress in the area of photosensitive ligands would provide exciting new possibilities in the realm of fabrication of devices utilizing colloidal QDs.

Chapter 5

5 STRATEGIES FOR CRYSTAL BOUND LEAD SULFIDE

In congruence with previous topics, the following chapter concerns itself with surface chemistry, but this time on a deeper level. While most NPs feature ligands which are bound to their surface, some reports have shown that the ligands can be embedded into the crystal lattice. This chapter focuses on these NPs which feature a robust attachment to their ligands into the crystal lattice, including synthesis and characterization.

5.1 Introduction: Crystal Bound Ligands and Hidden Functionality

Much of this dissertation—and research as a whole—has focused on manipulating surface chemistry via ligand exchange, but this portion of work shifts towards NPs which are synthesized in a manner which inhibits ligand exchange of their surfaces. A myriad of methods have been developed for the synthesis of colloidal semiconducting NPs including top-down methods,[198,199] intra-polymer and glass,[200–204], and solution phase,[142,147,205–211] the latter of which will be discussed here. The individual environments of the inorganic crystal lattice and outer organic ligands are fairly well understood, but the marriage of these two systems on the NP surface begets a unique system for each NP/ligand system. Research has been done on the dynamic nature of surface ligands in colloidal environments; some systems experience very rapid exchange of surface ligands in solution, while others remain more statically bound.[30,39–41,212] Work by Turo *et al.* has demonstrated a case where ligands remain tightly bound with Cu_2S and ZnS.[142,213] In this work, it was observed that when thiols are used as the sulfur source and ligand in reactions, the terminal layer of sulfurs on metal-sulfides seemed to remain attached to their carbon substituents. A visualization of this is seen in **Figure 5.1**.

As discussed in Chapter 1.2 (See **Figure 1.4**), several different types of ligand binding are known for ligands attached to the NP surface. These classifications (X-type [lattice termination through an anion], L-type [neutral donor], or Z-type [neutral acceptor])[214] all view the surface as a pristine surface which terminates in either a anionic or cationic atom. Such ideal conditions are likely not the case for all materials, as was demonstrated in the case of gold clusters. Single crystal data was obtained of $Au_{102(}SR)_{44}$ clusters which indicated that a “staple” motif was present.[215] In this binding mode, the surface sulfurs each bond to two gold atoms, wherein one gold atom is pulled upwards from the crystal lattice and bonds to two sulfur atoms simultaneously. An example of this is seen in **Figure 5.1b**. This motif has been verified for several other gold-thiol nanoclusters.[216–218] Since most nanocrystals do not form discrete clusters, single crystal x-ray data is not widely obtainable. However, this finding helps to illuminate the complexities of ligand binding on and in the surface. The actual surface connectivity of the semiconducting NPs discussed here has yet to be detailed on an atomic level, and general models do not apply to all systems. It is likely however, that each system possesses its own unique characteristics and cannot be adequately described by simplifications shown in **Figure 1.4** or **Figure 5.1a**.

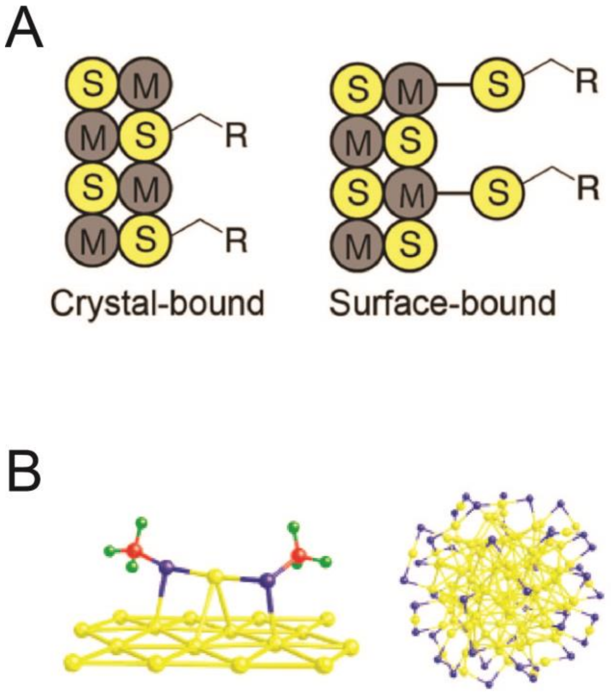

Figure 5.1. Crystal-bound versus Surface-bound ligands; A) The termination of crystal-bound ligands in metal sulfides features a thiol which has a higher coordination number than the surface-bound counterpart. Reprinted (adapted) with permission from reference 212. Copyright 2014 American Chemical Society. B) A "staple" motif adapted in gold clusters. Yellow atoms represent gold, blue atoms represent sulfur, red atoms represent carbon, and green atoms represent hydrogen. Reprinted (adapted) with permission from reference 214. Copyright 2008 American Chemical Society.

Different synthetic routes can be taken to obtain nanocrystals, and will be discussed here. Solution synthesis methods follow generally either a direct heat-up or injection pathway. Which of these two methods are utilized is dependent on the reactivity, melting point, and boiling point of precursors. In determining reagents for NP reactions, four components should be considered: metal source, chalcogenide source, solvent, and ligand. Not all of these components are independent of one another, however. For instance, a metal source such as $Pb(NO_3)_2$ may be reacted with thiobenzoic acid (TBA) separately rather than in situ to produce $Pb(TBA)_2$.[211] $Pb(TBA)_2$ can act as both the metal and chalcogenide source, meaning only an additional ligand and/or solvent are needed in the synthesis. Additionally, the ligand may be the chalcogenide source when using sulfur containing molecules such as dodecanethiol. The concentrations of these components along with stir times, temperatures, injections, and cleaning procedures all have an effect on the ultimate size, morphology, and quality of the product. An example of different morphologies obtained by varying these components to make PbS NPs can be seen in **Figure 5.2**.

The physical properties of reactants may determine reaction conditions or help to provide insight into variations of parameters which drive a desired effect. For instance, NP nucleation often requires the degradation of the metal and/or chalcogenide precursor. Information about the temperature at which this happens may be gained through differential scanning calorimetry (DSC),[219–221] or more simply through careful observation of color changes upon heating a reaction. Knowing decomposition temperature of a molecule is key to determining the temperature where active precursors can be generated. In the case of a reaction which utilizes separation of reagents through an injection, the decomposition temperature may be seen as a minimum temperature to assure rapid reaction of precursor upon injection due to the high concentration. The concentration of ligands which bind with precursors may also be varied in order to slow or expedite NP growth.[222]

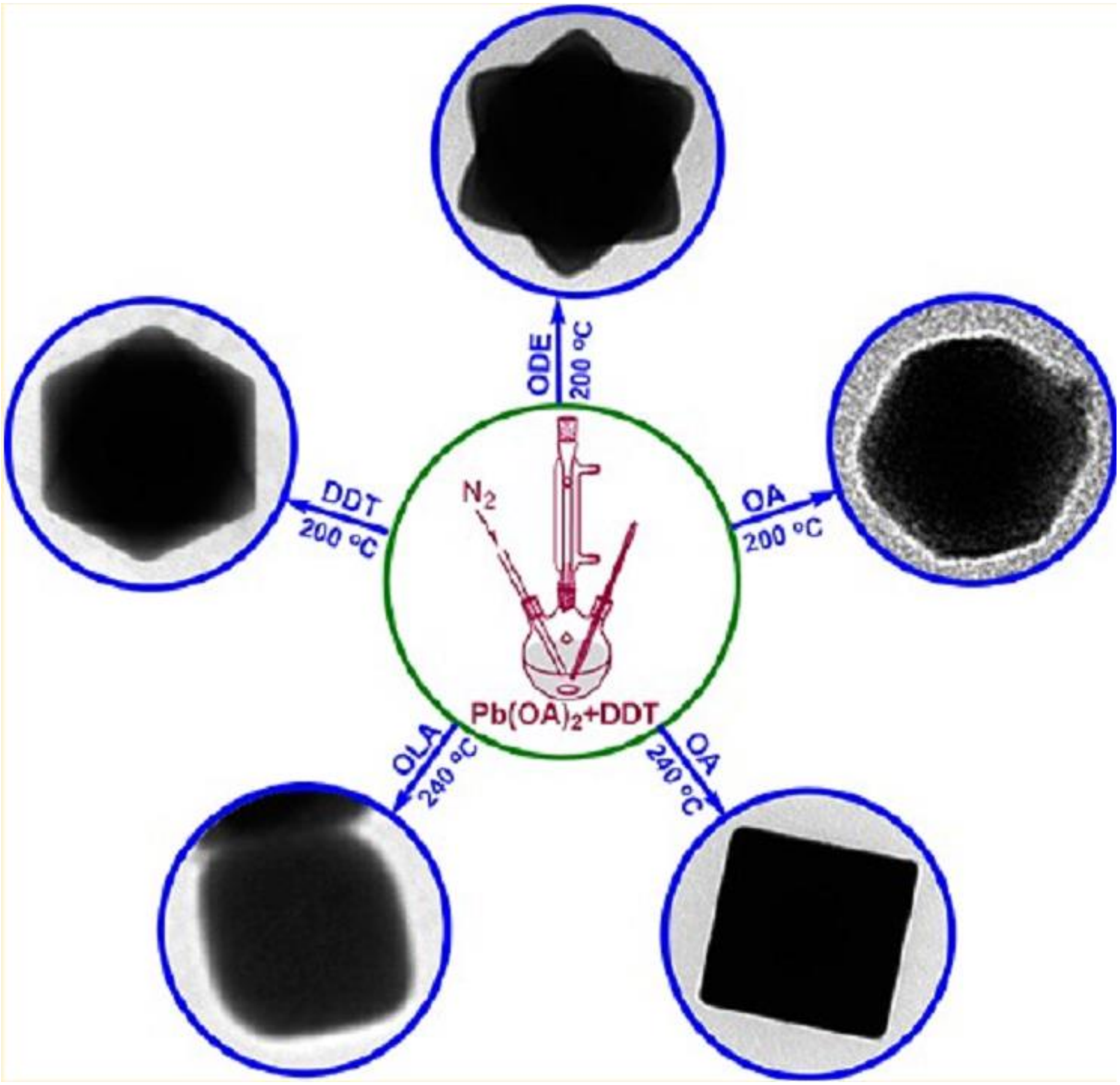

Figure 5.2. Morphology Control of PbS; Oleic acid (OA), dodecanethiol (DDT), octadecene (ODE), and oleylamine (OA) are used at various reaction temperatures to elicit different morphologies. Different binding of surfactants and surface ligands causes preferential growth of certain crystal facets. Reprinted (adapted) with permission from reference 206. Copyright 2012 American Chemical SocieFigure 5.3. Disulfide formation

Additionally, ligands may be added which bind preferentially to certain facets of a NP in order to push growth of a particle into a certain shape or crystal structure.[114]

NPs are characterized commonly via optical spectroscopy and electron microscopy; while these techniques provide important information they fail to provide an intimate surface analysis mapping the interactions on the surface. One technique which has been of importance is x-ray photoelectron spectroscopy. This surface technique bombards a sample with x-rays which causes electrons on the surface to escape the sample. The energy of the escaping electrons is measured and number of electrons counted. The specific energy of each electron is precise enough that not only can the specific element the electron originated from be determined, but also the element's oxidation state. This has been used previously in NPs to determine stoichiometric ratios,[223] oxidation states,[224] and relative coordination numbers.[142] The latter of these uses will be applied here to characterize NPs as surface bound or crystal bound. Another technique employed in our lab to test the strength of ligand binding is via the tracking of disulfide formation via NMR.[142] The surface of NPs, such as CdSe, are known to promote disulfide formation under amibient light and air exposure.[30,214,225] This can be seen visually through the agglomeration of NPs due to loss of surface ligands (see **Figure 5.3a**). It was found that if excess sulfide, in this case dodecyl-3-mercaptopropanoate (D3MP), was added to samples of CdSe NPs which were identical except for the suspected binding mode of the particles, the surface bound samples cause the formation of a significantly larger amount of disulfide due to the dynamic and exposed nature of the particle surface. This was shown in the proton NMR by a disappearance in the peak alpha to the thiol, and the appearance of a new peak corresponding the peak alpha to the disulfide. An example of this is shown in **Figure**

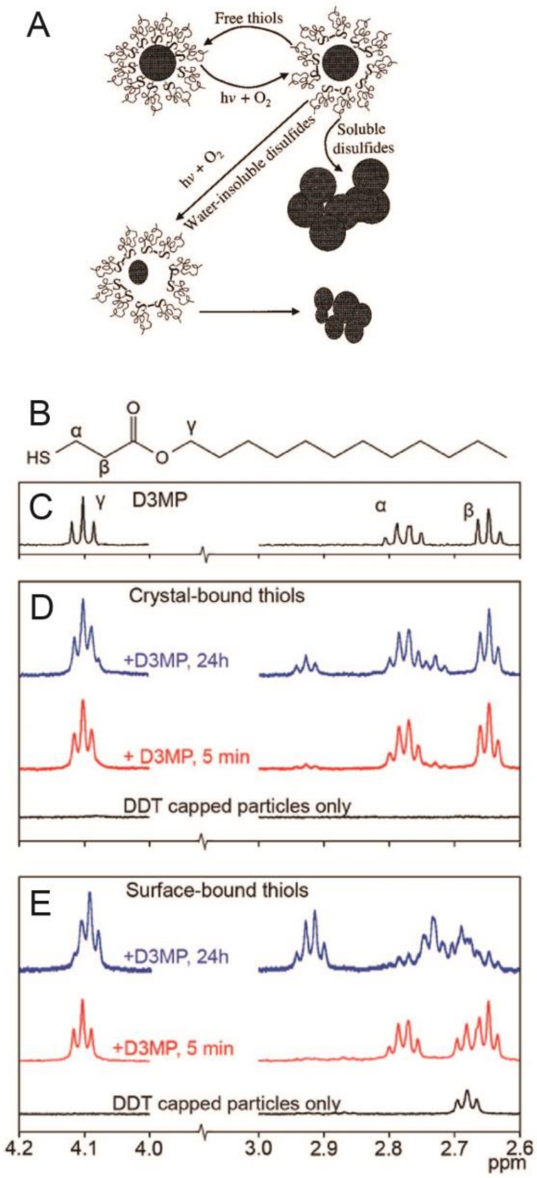

Figure 5.3. Disulfide formation on CdSe; A) Pathway of disulfide formation in ambient conditions on CdSe. Reprinted (adapted) with permission from reference 224. Copyright 2001 American Chemical Society. B) D3MP. C,D) NMR of crystal bound vs. surface bound thiols under ambient conditions after the addition of excess D3MP. Reprinted (adapted) with permission from reference 212. Copyright 2014 American Chemical SocietyFigure 5.4. Pb(OAc)$_2$ Reaction Times and Temperatures.

5.3b-e.

This chapter will focus on attempts to develop new methods of PbS synthesis which result in crystal-bound ligand systems, as well as the characterization required to differentiate between crystal and surface bound systems.

5.2 Precursors and Strategies

Two main goals were set for this project: produce and characterize PbS which display distinctly different properties related to surface bound and crystal-bound ligand systems, and design a general synthetic strategy for producing PbS with crystal bound ligands. PbS was chosen as a material of interest due to its heavy usage in devices such as solar cells. The ability to robustly and uniformly attach ligands to NP surfaces would aid in creating pristine films for photo-absorption that feature excellent charge mobility after cleavage to a short chain via a group such as D3MP. In this section various precursors will be investigated for suitability in making crystal bound PbS NPss. Syntheses will be addressed in order of Pb precursor. See Section D.1 in Appendix D for specific synthetic techniques.

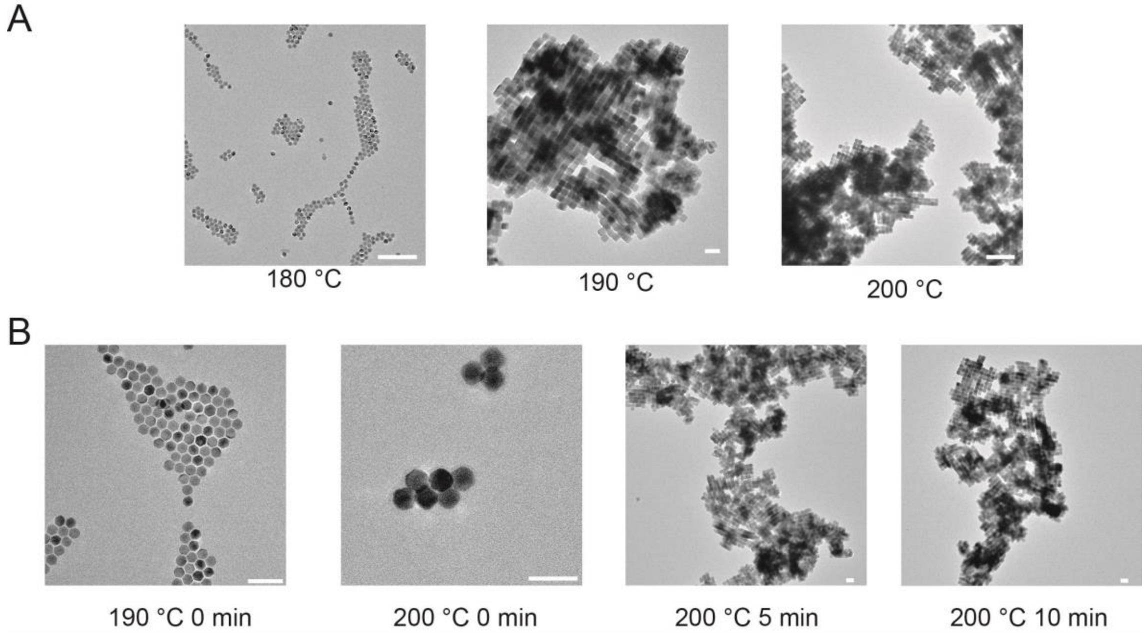

Figure 5.4. Pb(OAc)$_2$ Reaction Times and Temperatures; A) Reactions held at 10 minutes at specified temperatures. Scale bars are 200 nm. B) Reaction aliquots taken at specified times/temperatures for one experiment. Aliquots were injected into hexanes for quenching prior to washing. Scale bars are 50 Figure 5.5. TEM images of different lead

Initial attempts at PbS synthetic control were performed by directly adjusting the parameters of published methods. Mimicking a method by Hyeon *et al.*,[207] Pb(OAc)$_2$ was degassed with D3MP before heating to temperatures between 180 °C - 200 °C and being allowed to react for 0-10 min. It was observed that size and morphology could be tuned with time and temperature; shorter times and lower temperatures resulted in smaller, less distinct particles. At 10 minutes of growth time, a trend of reactions held at 180 °C produced spheres, 190 °C produced cubes, and 200 °C produced agglomerated cubes as shown in **Figure 5.4a**. Aliquots taken at 190 °C, 0 minutes at 200 °C, 5 minutes at 200 °C, and 10 minutes at 200 °C showed the progression of growth of the QDs as shown in **Figure 5.4b**. It is interesting to note that in these reactions what appear as hexagonal disks grow into cubes, which is similar to that seen in work done by Teng.[207] What is particularly important about these samples is that the earliest sample, taken at 190 °C, measured 14.1 ± 0.7 nm (n=120), which is smaller than the Bohr exciton radius of 20 nm for PbS and thus the particles are quantum confined (QC).[226] Quantum confinement is necessary for aptly tuned solar absorption and band compatibility in devices.[227–230] However, since 180 °C was the lowest temperature required for nucleation in this system yet produced particles which were still too large the desired application of solar cell fabrication. Other synthetic methods were thus sought which could produce smaller QDs.

The following strategies discussed here will use lead precursors which have been synthesized prior to the QD synthesis. A detailed procedure for lead salt synthesis can be found in **Appendix D**. $Pb(NO_3)_2$ was reacted with a thiol ligand to produce the corresponding salt, with the intent of increasing interaction between Pb and the organic counterion during NP synthesis. Initial studies were focused on $Pb(dodecanethiol)_2$ [$Pb(DDT)_2$] and $Pb(dodecyl\text{-}3\text{-}mercaptopropanoate)_2$ [$Pb(D3MP)_2$]. It was shown that reactions of these lead precursors alone in non-coordinating solvent lead to large particles, so additional reagents needed to be added. Bis-trimethylsilyl sulfide (TMSS) is known as a very volatile and reactive sulfur source which is used at relatively low temperatures (~125 °C) to produce very small quantum confined PbS QDs used in solar cells. Since the reaction of TMSS and Pb oleate resulted in nucleation followed by growth with Pb oleate, the Pb oleate was replaced with the lead salt of the ligand desired for the final product. The intention of this method was to produce a synthesis in which the only coordinating ligand was also a sulfur source. This method was successful in making small, colloidal, spherical PbS using D3MP and DDT as seen in **Figure 5.5a and b**. However, this method did not prove fruitful in providing a method in which size or surface chemistry can be controlled. Many variables were altered for particles prepared from $Pb(D3MP)_2$ including Pb precursor concentration, sulfur precursor concentration, surfactant concentration, amount of TMS, reaction temperature, and reaction time, but all resulting particles were of a similar size (2-5 nm) and morphology (see **Appendix D**). Indeed, it can be said that this reaction was reliable in terms of reproducibility, but was not adaptable. This method was

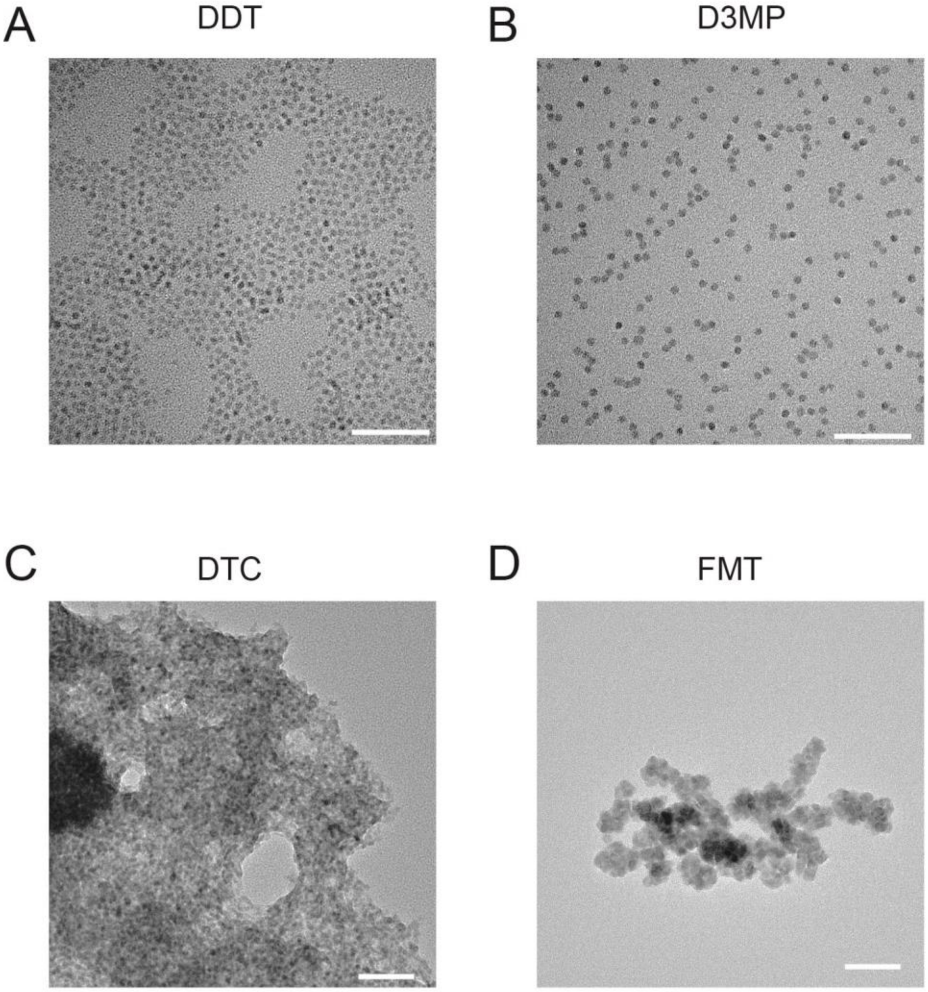

Figure 5.5. TEM images of different lead salt QDs; A) $Pb(DDT)_2$ B) $Pb(D3MP)_2$ C) $Pb(DTC)_2$ D) $Pb(FMT)_2$. All scale bars are 50 nmFigure 5.6. TEM images of tested PbS QDs.

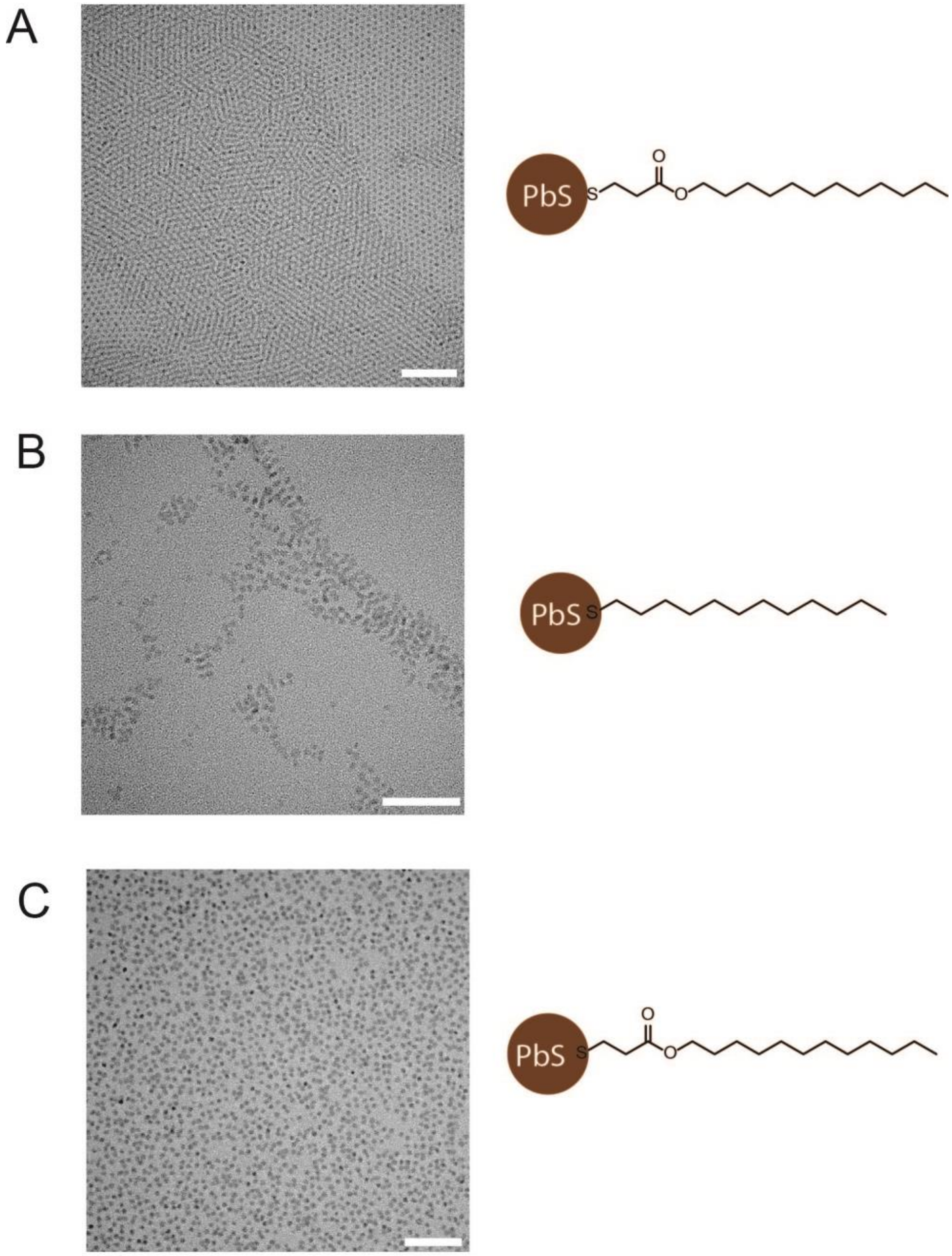

Figure 5.6. TEM images of tested PbS QDs; A) Surface bound D3MP (diameter = 3.6 nm) on PbS NPs, B) Crystal bound DDT (diameter = 1.9 nm) on PbS NPs, and C) Crystal bound D3MP (diameter = 4.0 nm) on PbS NPs. All scale bars are 50 nm. Sizes were calculated using an equation from reference 14Figure 5.7. NMR test of ligand dynamics.7.

also attempted with O-((9H-fluoren-9-yl)methyl) S-(2-mercaptoethyl) carbonothioate

(FMT) and dithiocarbamate (DTC) lead salts, but these ligands proved to be too reactive and only produced PbS agglomerates as seen in **Figure 5.5c and d**.

5.3 Surface Analaysis

After developing a method which reliably produced PbS QDs with possible crystal bound surface chemistry, NMR and XPS were used to evaluate the surface activity and bonding nature. For the following surface bound particles, the well-studied reaction between Pb-oleate and bis-trimethylsilyl sulfide (TMS) was performed, followed by a ligand exchange with dodecanethiol (DDT).[147] For crystal-bound ligand PbS QDs, the reaction of $Pb(D3MP)_2$ or $Pb(DDT)_2$ and TMS at 180 °C per conditions developed in lab (*vide infra*) was employed. TEM images of these NPs can be seen in **Figure 5.6.** All particles were spherical and exhibited a narrow size distribution as evidenced by a sharp first exciton peak in the near-IR absorbance (**Figure D.2**).

A surface exchange NMR experiment was undertaken to observe the surface reactivity of the different PbS samples. In these experiments DDT surface-bound and crystal-bound ligand PbS QDs were used. After synthesis and/or ligand exchange the samples were washed thoroughly by precipitation with acetone until the proton NMR spectra of the samples showed only the peaks from DDT bound to the surface, which consists of a methyl peak and alkyl chain peaks. An excess of D3MP was then added to the QDs and the spectra recorded once more. After addition, only D3MP peaks were visible; the excess of ligand and overlapping chemical shift with the QD ligands occluded

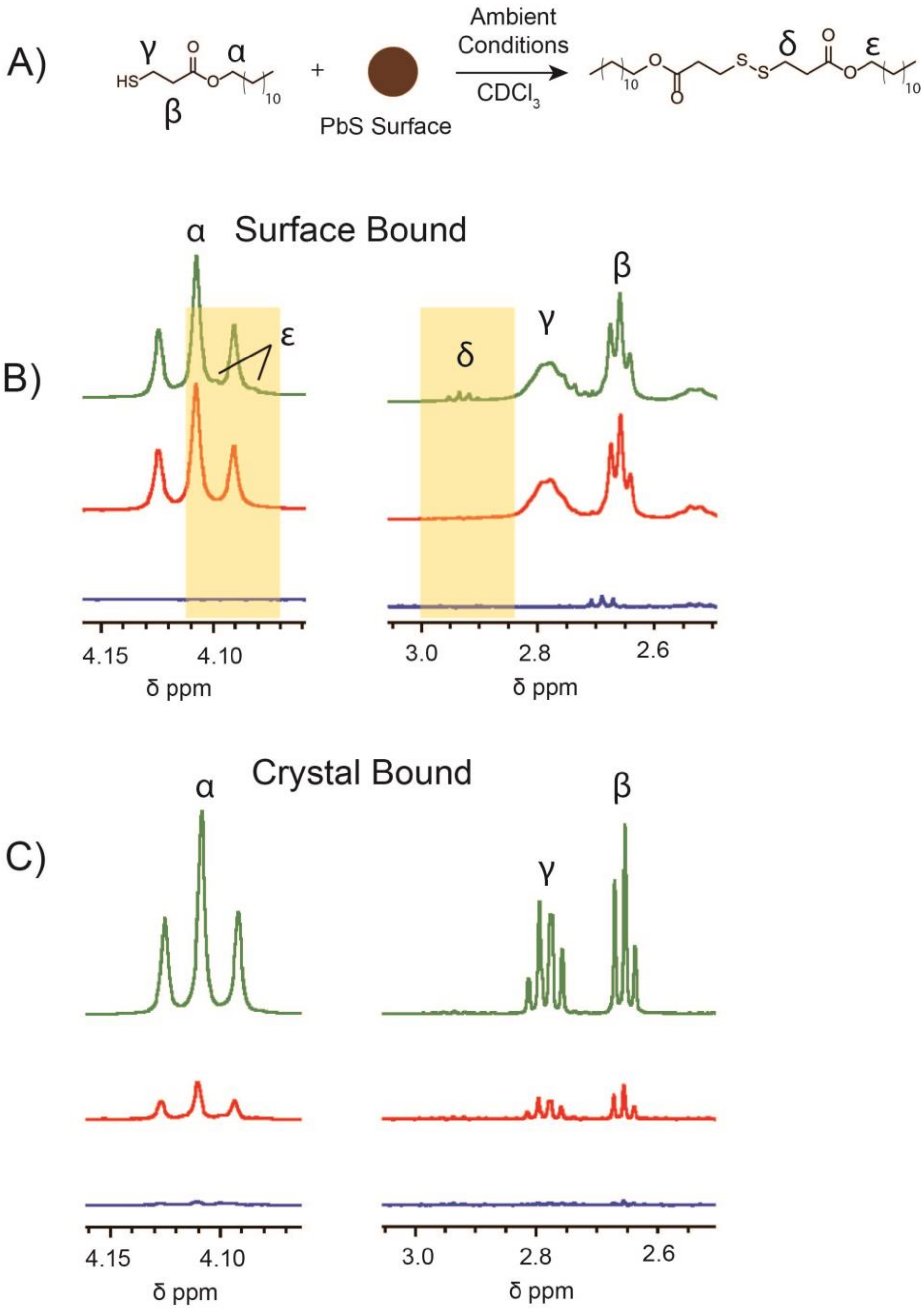

Figure 5.7. NMR test of ligand dynamics.; A) Expected reaction from surface bound particles. B, C) Resulting NMR from surface bound DDT coated QDs: Before D3MP addition (blue), directly after D3MP addition (red), 24 hours after D3MP addition (green).

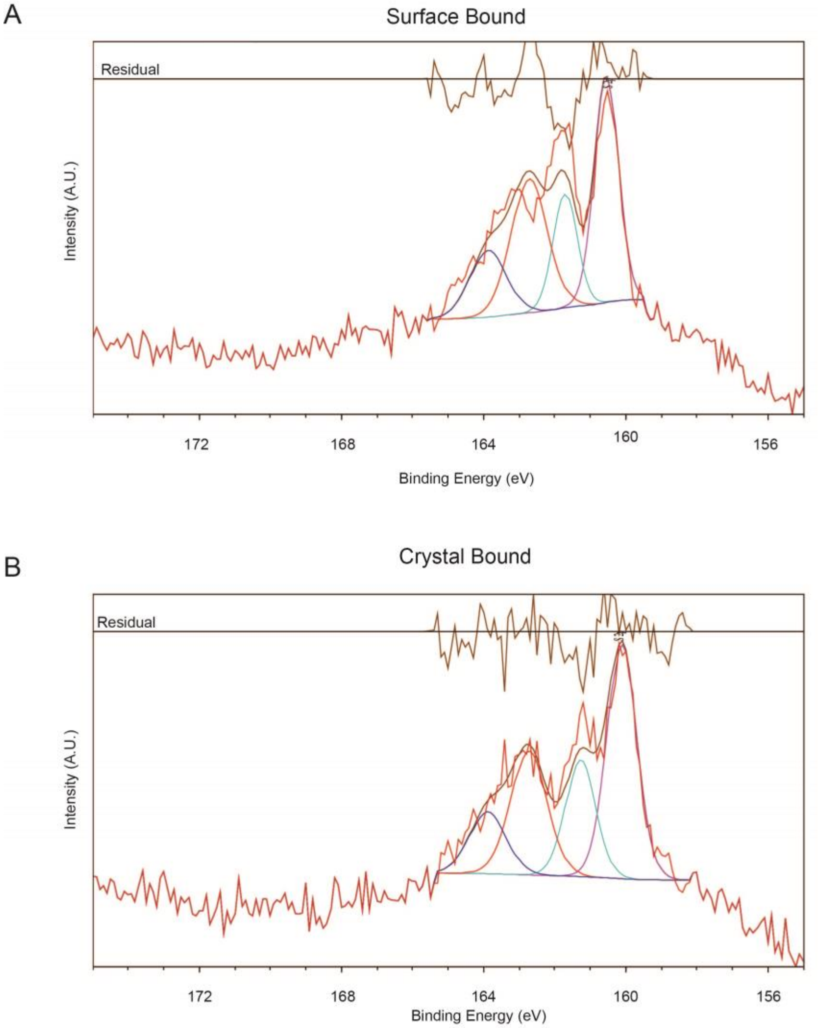

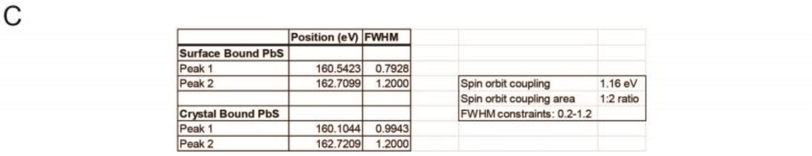

	Position (eV)	FWHM
Surface Bound PbS		
Peak 1	160.5423	0.7928
Peak 2	162.7099	1.2000
Crystal Bound PbS		
Peak 1	160.1044	0.9943
Peak 2	162.7209	1.2000

Spin orbit coupling	1.16 eV
Spin orbit coupling area	1:2 ratio
FWHM constraints: 0.2-1.2	

Figure 5.8. XPS Measurements of PbS QDs.; A) XPS of S2p orbitals for surface bound PbS QDs. B) XPS of S2p orbitals for crystal bound PbS QDs. C) Peak positions and FWHM along with constraints. Data was analyzed using CasaXPS.

visibility of DDT ligands (**Figure 5.7)**. Of particular interest on D3MP in this study were the peaks alpha to the ester and alpha to the thiol, as their downfield chemical shift makes them readily identifiable. After 24 hours in solution under ambient conditions the proton NMR was recorded again. At this point in time, signals could be seen appearing in the surface bound signal denoted as δ and ε in **Figure 5.7**, but not in the crystal bound sample. This is due to the oxidative nature of the QD surface coupled with the dynamic nature of surface bound ligands in comparison to crystal bound ligands.[142,214,231] The new signals are attributed to the formation of the disulfide of D3MP, which was shown experimentally previously by other group members.[142] This reaction is occurring due to the dynamic nature of surface-bound ligand systems; ligands are able to detach and reattach from the surface, allowing for photo-oxidation to occur.

Given promising NMR results, XPS was undertaken as a secondary characterization technique to verify the possibility of a different binding mode. These samples were prepared by drop casting surface bound or crystal bound PbS QDs onto a silicon wafer and allowing the solvent to evaporate. The XPS signal for sulfur 2p orbitals were examined closely, as shown in **Figure 5.8**, as these orbitals are the ones which are responsible for bonding between the sulfur and other carbon or lead atoms. Unfortunately, these results were not conclusive as a way to classify the character of two types of distinct surfaces. The 2p region of sulfur XPS shows one sulfur signal as a doublet of peaks due to spin-orbit coupling. In both samples run through XPS, two sets of doublets were observed, corresponding to sulfur in two different oxidation states (in this case, it can be thought of as different coordination numbers). Previous work has shown that in crystal-bound samples, only one doublet is expected, as all sulfur is integrated into the crystal lattice.

Given the relative success of the NMR experiment, it is possible that the crystal-bound sample possesses some facets which are ligated on the surface while others are crystal bound, causing multiple signals in the XPS. Ultimately these results further press the critical issue with nanoparticle characterization which limits understanding of structure-property relationships: surface analysis.

5.4 Further Directions

Multiple synthetic methods were used to synthesize and characterize PbS QDs in hopes of producing a system that could be definitively considered crystal-bound. Two pressing issues in synthesis were that of size and colloidal stability; the QDs had to be maintained small enough that they were quantum confined and useful for device fabrication, and colloidal stability is required to produce a uniform film. While new methods were developed that produced monodisperse PbS at appropriate size, very little control was gained over varying size or ligand chemistry. Further, while NMR data showed reduced dynamic ligand activity for crystal bound samples, XPS data was inconclusive.

QD synthesis has reached a point where analysis of surface on an atomic level is of importance for understanding and exploiting the unique properties of these materials. Further advancements in the areas of spectroscopy and microscopy will allow for these materials to be understood in terms of catalytic properties on the nanoscale and larger after device fabrication, which will in turn guide research into advanced synthetic methods to achieve desired goals.

Chapter 6

6 CONCLUSION

6.1 Summary

As energy demand across the globe continues to rise, the demand for new methods of producing clean energy will continue to increase. Renewable energy sources such as solar are particularly suited to this because of their limited carbon footprint,[232] but also their ability to be deployed in remote areas without the need for energy transport services. The work herein shows incremental steps towards the development of new technology which can meet these needs, and also provides a deeper insight into the fundamental materials properties of colloidal semiconducting NP systems.

The second chapter addressed the need to be able to efficiently trap charges outside of NP cores to perform oxidative or reductive reactions. This area of research is crucial to the application of colloidal NPs in catalytic systems such as the reduction and oxidation of H_2O to H_2 and O_2 gas, respectively. Application can also be found in the catalytic production of chemical feedstocks.[233,234] In this work, a functional group known to chelate and interact electronically with common metal-chalcogenide semiconducting NPs, a dithiocarbamate, was appended to a common ligand, 2-2,-bipyridine, used in catalytic processes. It was shown that ligand exchange from native ligands to the new ligand followed by addition of an iron salt allowed for the metal complex to be anchored to the NP surface. This interaction caused a quench in the photoluminescence and fluorescence lifetime, indicating the extraction of charges to new molecular states caused by the interaction of the complex with the NP as shown from DFT calculations. These fundamental studies show the possibility of harnessing the power of visible light through semiconducting NPs for catalytic reactions.

These studies were promising in that the expected QY quench and decrease in fluorescence lifetime are indicative of the transfer of a charge out into the ligands where radiative recombination no longer occurs. It is even more exciting that the modeling performed by Andrew O’hara from the group of Sokrates Pantelides was able to predict not only that charge transfer would occur, but also accurately predict the timescale on which it would occur. However, it is necessary for charges to remain at catalytic sites long enough for a catalytic process to happen. In the case of water splitting, oxidation reactions occur on substantially slower timescales than reduction reactions. The indication that a charge has been removed from the inorganic NP is exciting, but further studies to determine the stability of the oxidized catalyst would be needed to validate the possibility of harnessing the charge transfer for a chemical reaction. Further, in this study, it was discovered that the ligand which had been designed for water oxidation was itself sensitive to water. More work needs to be invested in designing functional groups which are stable to more harsh conditions while maintaining hole transfer functionality.

Moving forward, there are two majors challenges which need to be addressed: ligand stability and reaction rate management. Dithiocarbamate ligands are known to be susceptible to degradation in acidic conditions after protonation of the amine as seen in **Figure 6.1a**.[118] This results in the generation of CS_2 and the corresponding amine. This pathway could possibly be hindered through the replacement of the nitrogen proton with a bulkier group such as –methyl or –t-butyl (**Figure 6.1b**). Addition of these groups would increase steric hindrance around the lone nitrogen pair, as well as lend electron density towards the nitrogen group. This would make the amine a more active nucleophile, and strengthen the N-C(S)$_2$ bond. Another possible route towards improving stability could be found in xanthates (**Figure 6.1c**). While these ligands have yet to be studied in regards to their hole extracting qualities on metal chalcogenide NPs, they may possess similar electronic properties while showing greater stability; however, they are also known to degrade in acidic conditions. Ultimately, it may be necessary to utilize basic or slightly basic conditions for ligand stability when attempting to use these types of ligands.

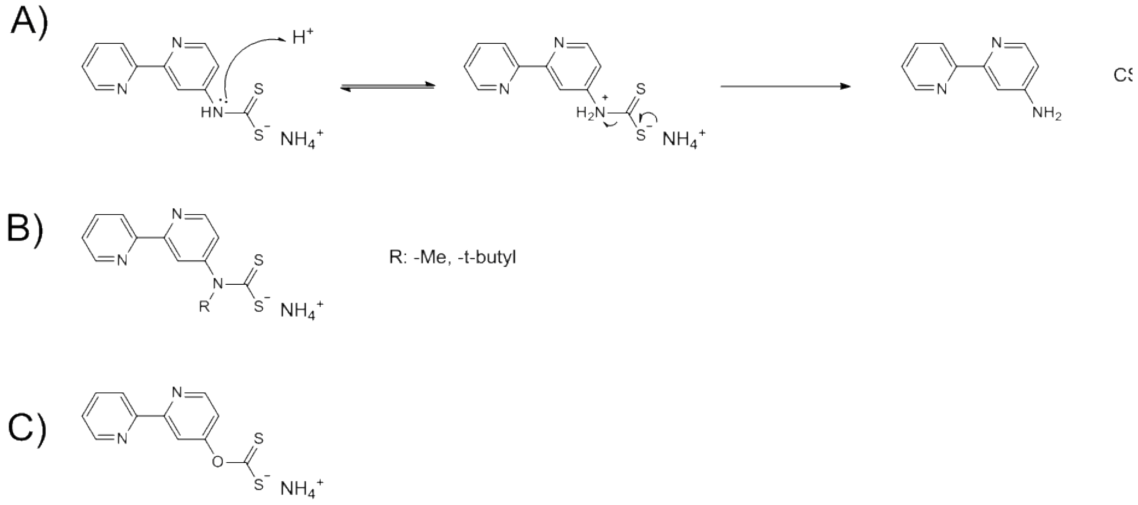

Figure 6.1. DTCBipy Challenges and Opportunities; A) Degradation pathway of DTCBipy in acidic medium. B) DTCBipy alternatives C) Xanthate derivation of DTCBipy.

Further efforts must also be made to address the difference in time scales of the water reduction and water oxidation reactions. Previous reports have shown that by using a hydroxyl anion-radical redox couple at high pH can result in almost unity H_2 production quantum efficiency,[16] but these conditions are not optimal for a fast rate of hydrogen production. The idea of using a redox shuttle, however, could prove beneficial, as if holes remain attached to a NP for too long newly promoted electrons may still recombine with holes in the ligands.[235] Other research has shown that hydrogen production can be performed by shuttling electrons from CdSe NPs,[236] so further research should be focused towards performing water oxidation via shuttling the hole from the NP to a catalyst in solution. After this process and related timescales are understood, it may be possible to optimize a system in which water is directly reduced on the photoabsorber, while water is oxidized by holes shuttled from the photoabsorber to a catalyst in solution.

In chapter 3, the improvement of fabrication methods for solar cells was addressed by looking at the nature of solid state ligand exchange. Since colloidal NPs are grown in organic solvent, they ultimately are covered in long chain organic ligands. These ligands are charge insulating, and must be removed before the NPs are suitable for solar cells. The most common method of doing this involves a solid state exchange whereby lead oleate is ripped from the particle surface and replaced with a short chain ligand such as ethane dithiol. This chapter focused on the design and synthesis of a short molecule mono-functionally protected with a protecting group which could be easily removed. After a complete ligand exchange—something which can only be verified in solution—was performed, the NPs were used to make a pristine film. This film could then be deprotected to produce a film made from entirely short-ligand coated NPs, which demonstrated a more p-type behavior. The film was then used in a solar cell to show improved efficiency over controls, indicating that typical solid state exchange methods are not completely treating the surface of NPs used in colloidal NP devices.

This collaboration in this work brought together groups focusing at very different levels to uncover synergistic results. I proposed that by incorporating a peptide protecting group into the surface ligands of NPs, a superior film could be produced for devices such as solar cells. After I tackled the challenge of synthesizing the ligand and verifying the colloidal stability of NPs after ligand exchange with it, the Sargent group took up the application of this absorber to devices. Such a proposal—of using peptide chemistry in solar cell designs—had never occurred to them, and highlights the transformative role a diverse knowledge of chemistry can play in device engineering. While I was focused on the interface between particle and environment, they focused on the interface between disparate layers of material. This allowed them to apply their engineering and fabrication knowledge which was needed but I was not personally able to complete. The resulting p-type film provided an excellent stepping stone in a graded architecture which resulted in the end goal of a more efficient device.

Incorporating the knowledge that band position can be changed by ligand coverage, and that this can be altered by changing from solid state to colloidal exchange methods, further fabrication studies could provide continued improvements into device architecture. Since one additional layer increased device efficiency, it is likely that controlling multiple layers to fabricate a more gradual energy level gradient from the depletion zone of the solar cell through the absorbing layer to the hole transport layer and metal contact would further optimize charge transport to improve efficiency. This would require the collaboration between synthetic, computational, and device fabrication scientists to determine what ligands are likely to alter the energy alignment of PbS when bound to the surface, how to make and apply the ligands, and how to incorporate the new methodologies into fabrication.

Chapter 4 dealt with manipulating NP surfaces to transition from long, charge-insulating ligands to very short chain ligands, but sought to achieve the goal through photocatalytic reactions. Whereas chapter 3 used chemical treatment of ligands to transform colloidally stable ligands to short-chain charge transfer capable ligands, this chapter dealt with light sensitive ligands. With solid state exchange or previous functional group cleavage, acids or bases must be employed which disturb or damage NP surfaces. This interference may result in trap states which hinder charge transfer, and thus device performance. Several different photo-labile targets were identified and synthesized, as well as tested for photo-activity. While some activity was seen with the ligands isolated, it was not in a controlled manner as reported previously. Further, it was found that during the photodegradation process the generation of a free thiol and benzaldehyde group would lead to further undesirable side reactions. Future targets for photodegradable colloidal semiconducting NPs were also discussed.

One possible application of these ligands is the incorporation of them into devices such as solar cells as discussed in chapter 3. A fabrication method in which pristine QD films can be deposited, followed by a deprotection with no added reagents would take extra variables out of the process and allow for films optimal for charge transfer. Such a method would prove useful, though it is conceivable that their use for colloidal semiconductors may be limited. The UV light typically used to degrade ligands is strongly absorbed by most semiconductors, so the amount of incident light making it to the ligands may be too small. Further, side reactions occurring from released byproducts could cause issues just as cleavage reagents do. The idea has however been demonstrated on non-colloidal materials, and merits further research.

The final research chapter of this work delved into the binding mode of NPs, specifically PbS. There are many different modes in which ligands can be bound to the surface (mono or bidentate, as a negative, positive, or neutral donor), but this chapter focused on work previously from our lab: ligands which are bound into the crystal lattice of the NP. It was previously shown by other members that for Cu_2S when using a sulfur source that is the same as the surfactant, the surface ligands become bound in the final layer of crystal lattice and feature a higher coordination number. Several synthetic schemes were devised to adapt this idea to PbS. NMR tests showed that the surface activity of possible crystal bound PbS was indeed altered through comparison with surface bound PbS, but XPS failed to show significant changes to the oxidation states of the sulfur on the surfaces of the NPs. Continued XPS experiments to ascertain the oxidation states of surface atoms would be useful. Another technique that could provide interesting information is elemental analysis, performed either by quantitative EDS or inductively coupled plasma experiments. This would provide data on the composition of lead and sulfur in the particles, which could prove interesting since the reactions ran were rich in sulfur. The proper balance of reactivity for each precursor still needs to be determined for these reactions. Further synthesis and surface analysis is necessary to implement these NPs in catalytic systems or devices.

This segment of research highlighted highly exploratory research. The area of surface chemistry is hotly debated, and the suggestion of a new ligand system, such as crystal-bound, is likely to spark debate with those in the field. Though some studies have documented such systems, proposing a new binding mode for any material requires highly corroborated data. This relies heavily on spectroscopic data acquisition and proper analysis. Though data were not collected to clearly indicate that which was sought, other interesting aspects of PbS growth, including smaller sizes/dimensions of crystals than previously reported were found. These new syntheses could perhaps be tuned to favor certain crystal facets for reactivity or film packing.

The driving purpose for developing QD applications in device fabrication and renewable energy utilization is to not only improve our environment, but to shift the paradigm of resource utilization for a sustainable future. The need for renewable energy comes not only from increased energy demand, but the negative impacts of burning fossil fuels. The increase of greenhouse gases in the environment not only causes an increase of temperature, but also alters environments by changing the biogeography of forests resulting in increased wildfires, changing precipitation patterns resulting in species die-off, and increased flood risk.[237–239] These problems will ultimately degrade the foundations of developed life as it is currently known by severely restricting the availability of all resources.[240] It can thus be seen that new paths must be taken to support human growth.

Many directions can be taken in attempting to begin to shift energy production or consumption towards a more sustainable future. This dissertation has focused on the surface chemistry of QDs to aid in both of these goals. A thorough understanding of this area will lead to precision control of syntheses to manipulate the size, shape, and morphology of these systems, which will lead to pushing the application of these materials into practical use. Further development of application-specific ligand systems will push these materials into the next generation of green energy devices.

REFERENCES

(1) Stocker, T. F.; Qin, D.; Plattner, G.-K.; Tignor, M.; Allen, S. K.; Boschung, J.; Nauels, A.; Xia, Y.; Bex, V.; Midgley, P. M. *Climate Change 2013: The Physical Science Basis. Contribution of Working Group I to the Fifth Assessment Report of the Intergovernmental Panel on Climate Change*; Cambridge, United Kingdom, 2013.

(2) Shafiee, S.; Topal, E. When Will Fossil Fuel Reserves Be Diminished? *Energy Policy* **2009**, *37*, 181–189.

(3) BP. Statistical Review of World Energy. *BP Stat. Rev. World Energy* **2016**, 1–48.

(4) Debije, M. G.; Verbunt, P. P. C. Thirty Years of Luminescent Solar Concentrator Research: Solar Energy for the Built Environment. *Adv. Energy Mater.* **2012**, *2*, 12–35.

(5) Goetzberger, A.; Hebling, C.; Schock, H.-W. Photovoltaic Materials, History, Status and Outlook. *Mater. Sci. Eng. R* **2003**, *40*, 1–46.

(6) Carey, G. H.; Abdelhady, A. L.; Ning, Z.; Thon, S. M.; Bakr, O. M.; Sargent, E. H. Colloidal Quantum Dot Solar Cells. *Chem. Rev.* **2015**, *115*, 12732–12763.

(7) Shockley, W.; Queisser, H. J. Detailed Balance Limit of Efficiency of P-n Junction Solar Cells. *J. Appl. Phys.* **1961**, *32*, 510–519.

(8) Graetzel, M. Photoelectrochemical Cells. *Nature* **2001**, *338-344*.

(9) Aggarwal, V. What are the most efficient solar panels on the market? https://news.energysage.com/what-are-the-most-efficient-solar-panels-on-the-market/ (accessed Aug 9, 2018).

(10) Alivisatos, A. P. Perspectives on the Physical Chemistry of Semiconductor Nanocrystals. *J. Phys. Chem.* **1996**, *100*, 13226–13239.

(11) Arico, A. S.; Bruce, P.; Scrosati, B.; Tarascon, J.; Schalkwijk, W. V. A. N. Nanostructured Materials for Advanced Energy Conversion and Storage Devices. *Nat. Mater.* **2005**, *4*, 366–377.

(12) Amirav, L.; Alivisatos, A. P. Photocatalytic Hydrogen Production with Tunable Nanorod Heterostructures. *J. Phys. Chem. Lett.* **2010**, 1051–1054.

(13) Liu, C.; Qiu, F.; Peterson, J. J.; Krauss, T. D. Aqueous Photogeneration of H_2 with

CdSe Nanocrystals and Nickel Catalysts: Electron Transfer Dynamics. *J. Phys. Chem. B* **2015**, *119*, 7349–7357.

(14) Hong, D.; Yamada, Y.; Nagatomi, T.; Takai, Y.; Fukuzumi, S. Catalysis of Nickel Ferrite for Photocatalytic Water Oxidation Using $[Ru(Bpy)_3]^{2+}$ and $S_2O_8^{2-}$. **2012**, 3–6.

(15) Kalisman, P.; Kauffmann, Y.; Amirav, L.; Maeda, K.; Teramura, K.; Lu, D.; Takata, T.; Saito, N.; Inoue, Y.; Domen, K.; *et al.* Photochemical Oxidation on Nanorod Photocatalysts. *J. Mater. Chem. A* **2015**, *3*, 3261–3265.

(16) Kalisman, P.; Nakibli, Y.; Amirav, L. Perfect Photon-to-Hydrogen Conversion Efficiency. *Nano Lett.* **2016**, *16*, 1776–1781.

(17) Kodama, R. . Magnetic Nanoparticles. *J. Magn. Magn. Mater.* **1999**, *200*, 359–372.

(18) Barnes, W. L.; Dereux, A.; Ebbesen, T. W. Surface Plasmon Subwavelength Optics. *Nature* **2003**, *424*, 824–830.

(19) Willets, K. A.; Van Duyne, R. P. Localized Surface Plasmon Resonance Spectroscopy and Sensing. *Annu. Rev. Phys. Chem.* **2007**, *58*, 267–297.

(20) Feynman, R. P. There's (Still) Plenty of Room at the Bottom. In *Annual Meeting of the American Physical Society at Caltech*; Pasadena, CA, 1960.

(21) Strehlow, W. H.; Cook, E.L. Compilation of Energy Band Gaps in Elemental and Binary Compound Semiconductors and Insulators. *J. Phys. Chem. Ref.* **1973,** *2*, 163-199.

(22) Kaupp, G. Mechanochemistry: The Varied Applications of Mechanical Bond-Breaking. *CrystEngComm* **2009**, *11*, 388–403.

(23) Suryanarayana, C. Mechanical Alloying and Milling. *Prog. Mater. Sci.* **2001**, *46*, 1–184.

(24) Fecht, H. J. Nanostructure Formation by Mechanical Attrition. *Nanostructured Mater.* **1995**, *6*, 33–42.

(25) Barth, S.; Hernandez-Ramirez, F.; Holmes, J. D.; Romano-Rodriguez, A. Synthesis and Applications of One-Dimensional Semiconductors. *Prog. Mater. Sci.* **2010**, *55*, 563–627.

(26) Lu, W.; Lieber, C. M. Semiconductor Nanowires. *J. Phys. D. Appl. Phys.* **2006**, *39*.

(27) Wang, X.; Zhuang, J.; Peng, Q.; Li, Y. A General Strategy for Nanocrystal Synthesis. *Nature* **2005**, *437*, 121–124.

(28) Chhowalla, M.; Shin, H. S.; Eda, G.; Li, L. J.; Loh, K. P.; Zhang, H. The Chemistry of Two-Dimensional Layered Transition Metal Dichalcogenide Nanosheets. *Nat. Chem.* **2013**, *5*, 263–275.

(29) Bahrig, L.; Hickey, S. G.; Eychmüller, A. Mesocrystalline Materials and the Involvement of Oriented Attachment-a Review. *CrystEngComm* **2014**, *16*, 9408–9424.

(30) Owen, J. S.; Park, J.; Trudeau, P.-E.; Alivisatos, A. P. Reaction Chemistry and Ligand Exchange at Cadmium−Selenide Nanocrystal Surfaces. *J. Am. Chem. Soc.* **2008**, *130*, 12279–12281.

(31) Anderson, N. C.; Hendricks, M. P.; Choi, J. J.; Owen, J. S. Ligand Exchange and the Stoichiometry of Metal Chalcogenide Nanocrystals: Spectroscopic Observation of Facile Metal-Carboxylate Displacement and Binding. *J. Am. Chem. Soc.* **2013**, *135*, 18536–18548.

(32) Morrison, C. E.; Wang, F.; Rath, N. P.; Wieliczka, B. M.; Loomis, R. A.; Buhro, W. E. Cadmium Bis(Phenyldithiocarbamate) as a Nanocrystal Shell-Growth Precursor. *Inorg. Chem.* **2017**, *56*, 12920–12929.

(33) Reiss, P.; Protière, M.; Li, L. Core/Shell Semiconductor Nanocrystals. *Small* **2009**, *5*, 154–168.

(34) Lead, J. R.; Batley, G. E.; Alvarez, P. J. J.; Croteau, M. N.; Handy, R. D.; McLaughlin, M. J.; Judy, J. D.; Schirmer, K. Nanomaterials in the Environment: Behavior, Fate, Bioavailability, and Effects—An Updated Review. *Environ. Toxicol. Chem.* **2018**, *37*, 2029–2063.

(35) Murray, C. B.; Norris, D. J.; Bawendi, M. G. Synthesis and Characterization of Nearly Monodisperse CdE (E = Sulfur, Selenium, Tellurium) Semiconductor Nanocrystallites. *J. Am. Chem. Soc.* **1993**, *115*, 8706–8715.

(36) Xia, Y.; Yang, P.; Sun, Y.; Wu, Y.; Mayers, B.; Gates, B.; Yin, Y.; Kim, F.; Yan, H. One-Dimensional Nanostructures: Synthesis, Characterization, and Applications. *Adv. Mater.* **2003**, *15*, 353–389.

(37) Sun, S.; Zeng, H.; Robinson, D. B.; Raoux, S.; Rice, P. M.; Wang, S. X.; Li, G. Monodisperse MFe_2O_4 (M = Fe, Co, Mn) Nanoparticles. *J. Am. Chem. Soc.* **2004**, *126*, 273–279.

(38) Spicer, C. D.; Jumeaux, C.; Gupta, B.; Stevens, M. M. Peptide and Protein

Nanoparticle Conjugates: Versatile Platforms for Biomedical Applications. *Chem. Soc. Rev.* **2018**, *47*, 3574–3620.

(39) Hens, Z.; Martins, J. C. A Solution NMR Toolbox for Characterizing the Surface Chemistry of Colloidal Nanocrystals. *Chem. Mater.* **2013**, *25*, 1211–1221.

(40) Gomes, R.; Hassinen, A.; Szczygiel, A.; Zhao, Q.; Vantomme, A.; Martins, J. C.; Hens, Z. Binding of Phosphonic Acids to CdSe Quantum Dots: A Solution NMR Study. *J. Phys. Chem. Lett.* **2011**, *2*, 145–152.

(41) Fritzinger, B.; Capek, R. K.; Lambert, K.; Martins, J. C.; Hens, Z. Utilizing Self-Exchange to Address the Binding of Carboxylic Acid Ligands to CdSe Quantum Dots. *J. Am. Chem. Soc.* **2010**, *132*, 10195–10201.

(42) Biesinger, M. C.; Payne, B. P.; Grosvenor, A. P.; Lau, L. W. M.; Gerson, A. R.; Smart, R. S. C. Resolving Surface Chemical States in XPS Analysis of First Row Transition Metals, Oxides and Hydroxides: Cr, Mn, Fe, Co and Ni. *Appl. Surf. Sci.* **2011**, *257*, 2717–2730.

(43) Rogach, A. L.; Franzl, T.; Klar, T. A.; Feldmann, J.; Gaponik, N.; Lesnyak, V.; Shavel, A.; Eychmüller, A.; Rakovich, Y. P.; Donegan, J. F. Aqueous Synthesis of Thiol-Capped CdTe Nanocrystals: State-of-the-Art. *J. Phys. Chem. C* **2007**, *111*, 14628–14637.

(44) Dabbousi, B. O.; Rodriguez-Viejo, J.; Mikulec, F. V.; Heine, J. R.; Mattoussi, H.; Ober, R.; Jensen, K. F.; Bawendi, M. G. (CdSe)ZnS Core−Shell Quantum Dots: Synthesis and Characterization of a Size Series of Highly Luminescent Nanocrystallites. *J. Phys. Chem. B* **1997**, *101*, 9463–9475.

(45) Medintz, I. L.; Uyeda, H. T.; Goldman, E. R.; Mattoussi, H. Quantum Dot Bioconjugates for Imaging, Labelling and Sensing. *Nat. Mater.* **2005**, *4*, 435–446.

(46) Khanna, V. K. *Nanomaterials and Their Properties*; Springer, New Delhi, 2016.

(47) Baskoutas, S.; Terzis, A. F. Size-Dependent Band Gap of Colloidal Quantum Dots. *J. Appl. Phys.* **2006**, *99*.

(48) McKittrick, J.; Shea-Rohwer, L. E. Review: Down Conversion Materials for Solid-State Lighting. *J. Am. Ceram. Soc.* **2014**, *97*, 1327–1352.

(49) Brus, L. Electronic Wave Functions in Semiconductor Clusters: Experiment and Theory. *J. Phys. Chem.* **1986**, *90*, 2555–2560.

(50) Zhang, J. Z. Interfacial Charge Carrier Dynamics of Colloidal Semiconductor Nanoparticles. *J. Phys. Chem. B* **2000**, *104*, 7239–7253.

(51) Jain, P. K.; Lee, K. S.; El-Sayed, I. H.; El-Sayed, M. A. Calculated Absorption and Scattering Properties of Gold Nanoparticles of Different Size, Shape, and Composition: Applications in Biological Imaging and Biomedicine. *J. Phys. Chem. B* **2006**, *110*, 7238–7248.

(52) Yohan, D.; Chithrani, B. D. Applications of Nanoparticles in Nanomedicine. *J. Biomed. Nanotechnol.* **2014**, *10*, 2371–2392.

(53) Zhang, Y.; Grady, N. K.; Ayala-Orozco, C.; Halas, N. J. Three-Dimensional Nanostructures as Highly Efficient Generators of Second Harmonic Light. *Nano Lett.* **2011**, *11*, 5519–5523.

(54) Brown, D. J.; Morishige, N.; Neekhra, A.; Minckler, D. S.; Jester, J. V. Application of Second Harmonic Imaging Microscopy to Assess Structural Changes in Optic Nerve Head Structure Ex Vivo. *J. Biomed. Opt.* **2007**, *12,* 024029-1 - 024029-5

.

(55) Li, Y.; Wang, H.; Xie, L.; Liang, Y.; Hong, G.; Dai, H. MoS_2 Nanoparticles Grown on Graphene: An Advanced Catalyst for the Hydrogen Evolution Reaction. *J. Am. Chem. Soc.* **2011**, *133*, 7296–7299.

(56) Liang, Y.; Li, Y.; Wang, H.; Zhou, J.; Wang, J.; Regier, T.; Dai, H. Co_3O_4 Nanocrystals on Graphene as a Synergistic Catalyst for Oxygen Reduction Reaction. *Nat. Mater.* **2011**, *10*, 780–786.

(57) Khan, S. U. M.; Mofareh, A.; Ingler, W. B. Efficient Photochemical Water Splitting by a Chemically Modified n-TiO_2. *Science.* **2013**, *297*, 2243–2245.

(58) Pelaez, M.; Nolan, N. T.; Pillai, S. C.; Seery, M. K.; Falaras, P.; Kontos, A. G.; Dunlop, P. S. M.; Hamilton, J. W. J.; Byrne, J. A.; O'Shea, K.; *et al.* A Review on the Visible Light Active Titanium Dioxide Photocatalysts for Environmental Applications. *Appl. Catal. B Environ.* **2012**, *125*, 331–349.

(59) Macdonald, J. E.; Veinot, J. G. C.; Macdonald, J. E.; Veinot, J. G. C. Removal of Residual Metal Catalysts with Iron/Iron Oxide Nanoparticles from Coordinating Environments. **2008**, *20*, 7169–7177.

(60) Kim, S. H.; Kwak, S. Y.; Sohn, B. H.; Park, T. H. Design of TiO2nanoparticle Self-Assembled Aromatic Polyamide Thin-Film-Composite (TFC) Membrane as an Approach to Solve Biofouling Problem. *J. Memb. Sci.* **2003**, *211*, 157–165.

(61) Sobana, N.; Muruganadham, M.; Swaminathan, M. Nano-Ag Particles Doped TiO2for Efficient Photodegradation of Direct Azo Dyes. *J. Mol. Catal. A Chem.* **2006**, *258*, 124–132.

(62) Chong, M. N.; Jin, B.; Chow, C. W. K.; Saint, C. Recent Developments in Photocatalytic Water Treatment Technology: A Review. *Water Res.* **2010**, *44*, 2997–3027.

(63) Kamat, P. V. Quantum Dot Solar Cells. Semiconductor Nanocrystals as Light Harvesters. *J. Phys. Chem. C* **2008**, *112*, 18737–18753.

(64) Nam, M.; Lee, T.; Kim, S.; Kim, S.; Kim, S. W.; Lee, K. K. Two Strategies to Enhance Efficiency of PbS Quantum Dot Solar Cells: Removing Surface Organic Ligands and Configuring a Bilayer Heterojunction with a New Conjugated Polymer. *Org. Electron. physics, Mater. Appl.* **2014**, *15*, 391–398.

(65) Carey, G. H.; Kramer, I. J.; Kanjanaboos, P.; Moreno-Bautista, G.; Voznyy, O.; Rollny, L.; Tang, J. A.; Hoogland, S.; Sargent, E. H. Electronically Active Impurities in Colloidal Quantum Dot Solids. *ACS Nano* **2014**, *8*, 11763–11769.

(66) Woong Jo, J.; Choi, J.; Pelayo García de Arquer, F.; Seifitokaldani, A.; Sun, B.; Kim, Y.; Ahn, H.; Fan, J.; Quintero-Bermudez, R.; Kim, J.; *et al.* Acid-Assisted Ligand Exchange Enhances Coupling in Colloidal Quantum Dot Solids. **2018**.

(67) Carey, G. H.; Yuan, M.; Comin, R.; Voznyy, O.; Sargent, E. H. Cleavable Ligands Enable Uniform Close Packing in Colloidal Quantum Dot Solids. *ACS Appl. Mater. Interfaces* **2015**, *7*, 21995–22000.

(68) Woong Jo, J.; Choi, J.; Pelayo García de Arquer, F.; Seifitokaldani, A.; Sun, B.; Kim, Y.; Ahn, H.; Fan, J.; Quintero-Bermudez, R.; Kim, J.; *et al.* Acid-Assisted Ligand Exchange Enhances Coupling in Colloidal Quantum Dot Solids. *Nano Lett.* **2018**, *16*, 4417–4423.

(69) La Croix, A. D.; O'Hara, A.; Reid, K. R.; Orfield, N. J.; Pantelides, S. T.; Rosenthal, S. J.; Macdonald, J. E. Design of a Hole Trapping Ligand. *Nano Lett.* **2017**, *17*, 909–914.

(70) Crowley, T. J. Causes of Climate Change Over the Past 1000 Years. *Science.* **2014**, *289*, 270–277.

(71) Dunn, S. Hydrogen Futures: Toward a Sustainable Energy System. *Int. J. Hydrogen Energy* **2002**, *27*, 235–264.

(72) Bak, T.; Nowotny, J.; Rekas, M.; Sorrell, C. . Photo-Electrochemical Hydrogen Generation from Water Using Solar Energy. Materials-Related Aspects. *Int. J. Hydrogen Energy* **2002**, *27*, 991–1022.

(73) Chen, X.; Shen, S.; Guo, L.; Mao, S. S. Semiconductor-Based Photocatalytic

Hydrogen Generation. **2010**, 6503–6570.

(74) Han, Z.; Qiu, F.; Eisenberg, R.; Holland, P. L.; Krauss, T. D. Robust Photogeneration of H_2 in Water Using Semiconductor Nanocrystals and a Nickel Catalyst. *Science..* **2012**, *338*.

(75) McCarthy, C. L.; Downes, C. A.; Schueller, E. C.; Abuyen, K.; Brutchey, R. L. Method for the Solution Deposition of Phase-Pure $CoSe_2$ as an Efficient Hydrogen Evolution Reaction Electrocatalyst. *ACS Energy Lett.* **2016**, *1*, 607–611.

(76) Lifshitz, E. Evidence in Support of Exciton to Ligand Vibrational Coupling in Colloidal Quantum Dots. *J. Phys. Chem. Lett.* **2015**, *6*, 4336–4347.

(77) Amirav, L.; Alivisatos, A. P. Photocatalytic Hydrogen Production with Tunable Nanorod Heterostructures. *J. Phys. Chem. Lett.* **2010**, *1*, 1051–1054.

(78) Wu, K.; Zhu, H.; Liu, Z.; Rodríguez-Córdoba, W.; Lian, T. Ultrafast Charge Separation and Long-Lived Charge Separated State in Photocatalytic CdS–Pt Nanorod Heterostructures. *J. Am. Chem. Soc.* **2012**, *134*, 10337–10340.

(79) Kato, H.; Asakura, K.; Kudo, A. Highly Efficient Water Splitting into H_2 and O_2 over Lanthanum-Doped $NaTaO_3$ Photocatalysts with High Crystallinity and Surface Nanostructure. *J. Am. Chem. Soc.* **2003**, *125*, 3082–3089.

(80) Kato, H.; Asakura, K.; Kudo, A. Highly Efficient Water Splitting into H_2 and O_2 over Lanthanum-Doped $NaTaO_3$ Photocatalysts with High Crystallinity and Surface Nanostructure. *J. Am. Chem. Soc.* **2003**, *125*, 3082–3089.

(81) Bao, N.; Shen, L.; Takata, T.; Domen, K. Self-Templated Synthesis of Nanoporous CdS Nanostructures for Highly Efficient Photocatalytic Hydrogen Production under Visible Light. *Chem. Mater..* **2008**, *20*, 110–117.

(82) Berr, M.; Vaneski, A.; Susha, A. S.; Rodríguez-Fernández, J.; Döblinger, M.; Jäckel, F.; Rogach, A. L.; Feldmann, J. Colloidal CdS Nanorods Decorated with Subnanometer Sized Pt Clusters for Photocatalytic Hydrogen Generation. *Appl. Phys. Lett.* **2010**, *97*, 093108-1 - 093108-3.

(83) Tarafder, K.; Surendranath, Y.; Olshansky, J. H.; Alivisatos, A. P.; Wang, L. Hole Transfer Dynamics from a CdSe/CdS Quantum Rod to a Tethered Ferrocene Derivative. **2014**, *136*, 5121-5131.

(84) Veinot, J. G. C.; Galloro, J.; Pugliese, L.; Pestrin, R.; Pietro, W. J. Surface Functionalization of Cadmium Sulfide Quantum-Confined Nanoclusters. 5. Evidence of Facile Surface-Core Electronic Communication in the

Photodecomposition Mechanism of Functionalized Quantum Dots †. *Chem. Mater.* **1999**, *11*, 642–648.

(85) Barnett, S. M.; Goldberg, K. I.; Mayer, J. M. A Soluble Copper-Bipyridine Water-Oxidation Electrocatalyst. *Nat. Chem.* **2012**, 1–5.

(86) Connor, T. O.; Panov, M. S.; Mereshchenko, A.; Tarnovsky, A. N.; Lorek, R.; Perera, D.; Diederich, G.; Lambright, S.; Moroz, P.; Zamkov, M. The Effect of the Charge-Separating Interface on Exciton Dynamics in Photocatalytic Colloidal Heteronanocrystals. **2012**, 8156–8165.

(87) Amirav, L.; Alivisatos, A. P. Luminescence Studies of Individual Quantum Dot Photocatalysts. *J. Am. Chem. Soc.* **2013**, *135*, 13049–13053.

(88) Lian, S.; Weinberg, D. J.; Harris, R. D.; Kodaimati, M. S.; Weiss, E. A. Subpicosecond Photoinduced Hole Transfer from a CdS Quantum Dot to a Molecular Acceptor Bound Through an Exciton-Delocalizing Ligand. *ACS Nano* **2016**, *10*, 6372–6382.

(89) Frederick, M. T.; Weiss, E. A. Relaxation of Exciton Confinement in CdSe Quantum Dots by Modification with a Conjugated Dithiocarbamate Ligand. *ACS Nano* **2010**, *4*, 3195–3200.

(90) Frederick, M. T.; Amin, V. A.; Cass, L. C.; Weiss, E. A. A Molecule to Detect and Perturb the Confinement of Charge Carriers in Quantum Dots. **2011**, *11*, 5455–5460.

(91) Frederick, M. T.; Amin, V. A.; Weiss, E. A. Optical Properties of Strongly Coupled Quantum Dot–Ligand Systems. *J. Phys. Chem. Lett.* **2013**, *4*, 634–640.

(92) Frederick, M. T.; Amin, V. A.; Swenson, N. K.; Ho, A. Y.; Weiss, E. A. Control of Exciton Confinement in Quantum Dot–Organic Complexes through Energetic Alignment of Interfacial Orbitals. *Nano Lett.* **2013**, *13*, 287–292.

(93) Wickramasinghe, L. D.; Zhou, R.; Zong, R.; Vo, P.; Gagnon, K. J.; Thummel, R. P. Iron Complexes of Square Planar Tetradentate Polypyridyl-Type Ligands as Catalysts for Water Oxidation. *J. Am. Chem. Soc.* **2015**, *137*, 13260–13263.

(94) Fillol, J. L.; Codolà, Z.; Garcia-Bosch, I.; Gàmez, L.; Pla, J. J.; Costas, M. Efficient Water Oxidation Catalysts Based on Readily Available Iron Coordination Complexes. *Nat. Chem.* **2011**, *3*, 807–813.

(95) Kresse, G.; Furthmüller, J. Efficient Iterative Schemes for *Ab Initio* Total-Energy Calculations Using a Plane-Wave Basis Set. *Phys. Rev. B* **1996**, *54*, 11169–11186.

(96) Yan, Y.; Chen, G.; Van Patten, P. G. Ultrafast Exciton Dynamics in CdTe

Nanocrystals and Core/Shell CdTe/CdS Nanocrystals. *J. Phys. Chem. C* **2011**, *115*, 22717–22728.

(97) Keene, J. D.; McBride, J. R.; Orfield, N. J.; Rosenthal, S. J. Elimination of Hole-Surface Overlap in Graded CdS_xSe_{1-x} Nanocrystals Revealed by Ultrafast Fluorescence Upconversion Spectroscopy. *ACS Nano* **2014**, *8*, 10665–10673.

(98) Xing, G.; Liao, Y.; Wu, X.; Chakrabortty, S.; Liu, X.; Yeow, E. K. L.; Chan, Y.; Sum, T. C. Ultralow-Threshold Two-Photon Pumped Amplified Spontaneous Emission and Lasing from Seeded CdSe/CdS Nanorod Heterostructures. *ACS Nano* **2012**, *6*, 10835–10844.

(99) Zavelani-Rossi, M.; Lupo, M. G.; Krahne, R.; Manna, L.; Lanzani, G. Lasing in Self-Assembled Microcavities of CdSe/CdS Core/Shell Colloidal Quantum Rods. *Nanoscale* **2010**, *2*, 931–935.

(100) Lupo, M. G.; Sala, F. Della; Carbone, L.; Zavelani-rossi, M.; Fiore, A.; Lu, L.; Polli, D.; Cingolani, R.; Manna, L.; Lanzani, G.; *et al.* Ultrafast Electron-Hole Dynamics in Core / Shell CdSe / CdS Dot / Rod Nanocrystals. *Nano Lett.* **2008**, *8*, 4582-4587.

(101)Wang, L., and Wang, Z. Efficient Cross-Coupling of Aryl Chlorides with Arylzinc Reagents Catalyzed be Amido Pincer Complexes of Nickel. *Org. Lett.* **2007.** *9*, 4335-4338.

(102) Krasovskiy, A.; Malakhov, V.; Gavryushin, A.; Knochel, P. Efficient Synthesis of Functionalized Organozinc Compounds by the Direct Insertion of Zinc into Organic Iodides and Bromides. *Angew. Chemie - Int. Ed.* **2006**, *45*, 6040–6044.

(103) Zhang, B.; Breslow, R. Ester Hydrolysis by a Catalytic Cyclodextrin Dimer Enzyme Mimic with a Metallobipyridyl Linking Group. *J. Am. Chem. Soc.* **1997**, *119*, 1676–1681.

(104) Sakamoto, T.; Kondo, Y.; Murata, N.; Yamanaka, H. Pyridinylzinc halides by oxidative addition of active zinc with halopyridines. **1992**, *33*, 5373–5374.

(105) Zhu, L.; Wehmeyer, R. M.; Rieke, R. D. The Direct Formation of Functionalized Alkyl (Aryl) Zinc Halides by Oxidative Addition of Highly Reactive Zinc with Organic Halides and Their Reactions with Acid Chlorides, α, β-Unsaturated Ketones, and Allylic, Aryl, and Vinyl Halides. *J. Org. Chem.* **1991**, *56*, 1445–1453.

(106) Bruno, N. C.; Tudge, M. T.; Buchwald, S. L. Design and Preparation of New Palladium Precatalysts for C-C and C-N Cross-Coupling Reactions. *Chem. Sci.* **2013**, *4*, 916–920.

(107) Chankeshwara, S. V.; Chakraborti, A. K. Catalyst-Free Chemoselective N-Tert-

Butyloxycarbonylation of Amines in Water. *Org. Lett.* **2006**, *8*, 3259–3262.

(108) Hodgson, P. B.; Salingue, F. H. The Preparation of a Stable 2-Pyridylboronate and Its Reactivity in the Suzuki-Miyaura Cross-Coupling Reaction. *Tetrahedron Lett.* **2004**, *45*, 685–687.

(109) Gütz, C.; Lützen, A. Synthesis of 2,2-Bipyridines via Suzuki-Miyaura Cross-Coupling. *Synthesis (Stuttg).* **2010**, 85–90.

(110) Munson, M. C.; Albericio, F.; Barany, G.; García-Echevería, C.; Albericio, F.; Albericio, F. S-2,4,6-Trimethoxybenzyl (Tmob): A Novel Cysteine Protecting Group for the Nα-(9-Fluorenylmethoxycarbonyl) (Fmoc) Strategy of Peptide Synthesis. *J. Org. Chem.* **1992**, *57*, 3013–3018.

(111) Bair, J. S.; Harrison, R. G. Synthesis and Optical Properties of Bifunctional Thiophene Molecules Coordinated to Ruthenium. *J. Org. Chem.* **2007**, *72*, 6653–6661.

(112) Aoyagi, Y., Abe, T., Ohta, A. Facile and Efficient Deoxygenation of Aromatic N-Oxides with Zinc and Aqueous Ammonium Chloride. *Synthesis (Stuttg).* **1997**, 891–894.

(113) Humeres, E.; Debacher, N. A.; Franco, J. D.; Lee, B. S.; Martendal, A. Mechanisms of Acid Decomposition of Dithiocarbamates. 3. Aryldithiocarbamates and the Torsional Effect. *J. Org. Chem.* **2002**, *67*, 3662–3667.

(114) Hill, L. J.; Bull, M. M.; Sung, Y.; Simmonds, A. G.; Dirlam, P. T.; Richey, N. E.; DeRosa, S. E.; Shim, I.; Guin, D.; Costanzo, P. J.; Pinna, N.; Willinger, M.; Vogel, W.; Char, K; Pyun, J. Directing the Deposition of Ferromagnetic Cobalt onto Pt-Tipped CdSe@CdS Nanorods : Synthetic and Mechanistic Insights.. *ACS Nano*. **2012,** *6*, 8632-8645.

(115) Demortière, A.; Schaller, R. D.; Li, T.; Chattopadhyay, S.; Krylova, G.; Shibata, T.; Dos Santos Claro, P. C.; Rowland, C. E.; Miller, J. T.; Cook, R.; *et al.* In Situ Optical and Structural Studies on Photoluminesence Quenching in CdSe/CdS/Au Heterostructures. *J. Am. Chem. Soc.* **2014**, *136*, 2342–2350.

(116) Talapin, D. V.; Koeppe, R.; Goetzinger, S.; Kornowski, A.; Lupton, J. M.; Rogach, A. L.; Benson, O.; Feldmann, J.; Weller, H. Highly Emissive Colloidal CdSe/CdS Heterostructures of Mixed Dimensionality. *Nano Lett.* **2003**, *3*, 1677–1681.

(117) Knowles, K. E.; McArthur, E. A.; Weiss, E. A. A Multi-Timescale Map of Radiative and Nonradiative Decay Pathways for Excitons in CdSe Quantum Dots. *ACS Nano* **2011**, *5*, 2026–2035.

(118) Humeres, E.; Debacher, N. A.; Franco, J. D.; Lee, B. S.; Martendal, A. Mechanisms of Acid Decomposition of Dithiocarbamates. 3. Aryldithiocarbamates and the Torsional Effect. *J. Org. Chem.* **2002**, *67*, 3662–3667.

(119) Leatherdale, C.; Kagan, C.; Morgan, N.; Empedocles, S.; Kastner, M.; Bawendi, M. Photoconductivity in CdSe Quantum Dot Solids. *Phys. Rev. B - Condens. Matter Mater. Phys.* **2000**, *62*, 2669–2680.

(120) Liu, I.-S.; Lo, H.-H.; Chien, C.-T.; Lin, Y.-Y.; Chen, C.-W.; Chen, Y.-F.; Su, W.-F.; Liou, S.-C.; Bruchez, M.; Moronne, M.; *et al.* Enhancing Photoluminescence Quenching and Photoelectric Properties of CdSe Quantum Dots with Hole Accepting Ligands. *J. Mater. Chem.* **2008**, *18*, 675.

(121) García de Arquer, F. P.; Armin, A.; Meredith, P.; Sargent, E. H. Solution-Processed Semiconductors for next-Generation Photodetectors. *Nat. Rev. Mater.* **2017**, *2*, 16100.

(122) Fan, F.; Voznyy, O.; Sabatini, R. P.; Bicanic, K. T.; Adachi, M. M.; McBride, J. R.; Reid, K. R.; Park, Y.-S.; Li, X.; Jain, A.; *et al.* Continuous-Wave Lasing in Colloidal Quantum Dot Solids Enabled by Facet-Selective Epitaxy. *Nature* **2017**, *544*, 75–79.

(123) Dai, X.; Zhang, Z.; Jin, Y.; Niu, Y.; Cao, H.; Liang, X.; Chen, L.; Wang, J.; Peng, X. Solution-Processed, High-Performance Light-Emitting Diodes Based on Quantum Dots. *Nature* **2014**, *515*.

(124) Ip, A. H.; Thon, S. M.; Hoogland, S.; Voznyy, O.; Zhitomirsky, D.; Debnath, R.; Levina, L.; Rollny, L. R.; Carey, G. H.; Fischer, A.; *et al.* Hybrid Passivated Colloidal Quantum Dot Solids. *Nat. Nanotechnol.* **2012**, *7*, 577–582.

(125) Lan, X.; Voznyy, O.; García De Arquer, F. P.; Liu, M.; Xu, J.; Proppe, A. H.; Walters, G.; Fan, F.; Tan, H.; Liu, M.; *et al.* 10.6% Certified Colloidal Quantum Dot Solar Cells via Solvent-Polarity-Engineered Halide Passivation. *Nano Lett.* **2016**, *16*, 4630–4634.

(126) Zhang, N.; Neo, D. C. J.; Tazawa, Y.; Li, X.; Assender, H. E.; Compton, R. G.; Watt, A. A. R. Narrow Band Gap Lead Sulfide Hole Transport Layers for Quantum Dot Photovoltaics. *ACS Appl. Mater. Interfaces* **2016**, *8*, 21417–21422.

(127) Zhang, X.; Zhang, J.; Phuyal, D.; Du, J.; Tian, L.; Öberg, V. A.; Johansson, M. B.; Cappel, U. B.; Karis, O.; Liu, J.; *et al.* Inorganic $CsPbI_3$ Perovskite Coating on PbS Quantum Dot for Highly Efficient and Stable Infrared Light Converting Solar Cells. *Adv. Energy Mater.* **2017**, *1702049*, 1702049.

(128) Cao, Y.; Stavrinadis, A.; Lasanta, T.; So, D.; Konstantatos, G. The Role of Surface

Passivation for Efficient and Photostable PbS Quantum Dot Solar Cells. *Nat. Energy* **2016**, *1*, 16035.

(129) Bi, Y.; Pradhan, S.; Gupta, S.; Akgul, M. Z.; Stavrinadis, A.; Konstantatos, G. Infrared Solution-Processed Quantum Dot Solar Cells Reaching External Quantum Efficiency of 80% at 1.35 Mm and J_{sc} in Excess of 34 mA cm^{-2}. *Adv. Mater.* **2018**, *30*, 1–6.

(130) Gao, J.; Perkins, C. L.; Luther, J. M.; Hanna, M. C.; Chen, H. Y.; Semonin, O. E.; Nozik, A. J.; Ellingson, R. J.; Beard, M. C. N-Type Transition Metal Oxide as a Hole Extraction Layer in PbS Quantum Dot Solar Cells. *Nano Lett.* **2011**, *11*, 3263–3266.

(131) Carey, G. H.; Levina, L.; Comin, R.; Voznyy, O.; Sargent, E. H. Record Charge Carrier Diffusion Length in Colloidal Quantum Dot Solids via Mutual Dot-To-Dot Surface Passivation. *Adv. Mater.* **2015**, *27*, 3325–3330.

(132) Chuang, C.-H. M.; Brown, P. R.; Bulović, V.; Bawendi, M. G. Improved Performance and Stability in Quantum Dot Solar Cells through Band Alignment Engineering. *Nat. Mater.* **2014**, *13*, 1–6.

(133) Brown, P. R.; Kim, D.; Lunt, R. R.; Zhao, N.; Bawendi, M. G.; Grossman, J. C.; Bulović, V. Energy Level Modification in Lead Sulfide Quantum Dot Thin Films through Ligand Exchange. *ACS Nano* **2014**, *8*, 5863–5872.

(134) Liu, M.; Voznyy, O.; Sabatini, R.; García De Arquer, F. P.; Munir, R.; Balawi, A. H.; Lan, X.; Fan, F.; Walters, G.; Kirmani, A. R.; *et al.* Hybrid Organic-Inorganic Inks Flatten the Energy Landscape in Colloidal Quantum Dot Solids. *Nat. Mater.* **2017**, *16*, 258–263.

(135) Chuang, C.-H. M.; Brown, P. R.; Bulović, V.; Bawendi, M. G. Improved Performance and Stability in Quantum Dot Solar Cells through Band Alignment Engineering. *Nat. Mater.* **2014**, *13*, 1–6.

(136) Zherebetskyy, D.; Scheele, M.; Zhang, Y.; Bronstein, N.; Thompson, C.; Britt, D.; Salmeron, M.; Alivisatos, P.; Wang, L.-W. Hydroxylation of the Surface of PbS Nanocrystals Passivated with Oleic Acid. *Science.* **2014**, *344*, 1380-1384.

(137) Boles, M. A.; Ling, D.; Hyeon, T.; Talapin, D. V. The Surface Science of Nanocrystals. *Nat. Mater.* **2016**, *15*, 141–153.

(138) Bagiyan, G. A.; Koroleva, I. K.; Soroka, N. V.; Ufimtsev, A. V. Oxidation of Thiol Compounds by Molecular Oxygen in Aqueous Solutions. *Russ. Chem. Bull.* **2003**, *52*, 1135–1141.

(139) Ip, A. H.; Labelle, A. J.; Sargent, E. H. Efficient, Air-Stable Colloidal Quantum Dot Solar Cells Encapsulated Using Atomic Layer Deposition of a Nanolaminate Barrier. *Appl. Phys. Lett.* **2013**, *103*, 1–4.

(140) Carey, G. H.; Yuan, M.; Comin, R.; Voznyy, O.; Sargent, E. H. Cleavable Ligands Enable Uniform Close Packing in Colloidal Quantum Dot Solids. *ACS Appl. Mater. Interfaces* **2015**, *7*, 21995–22000.

(141) Ip, A. H.; Labelle, A. J.; Sargent, E. H. Efficient, Air-Stable Colloidal Quantum Dot Solar Cells Encapsulated Using Atomic Layer Deposition of a Nanolaminate Barrier. *Appl. Phys. Lett.* **2013**, *103*, 1–4.

(142) Turo, M. J.; Macdonald, J. E. Crystal-Bound *vs* Surface-Bound Thiols on Nanocrystals. *ACS Nano* **2014**, *8*, 10205–10213.

(143) Ralhan, K.; KrishnaKumar, V. G.; Gupta, S. Piperazine and DBU: A Safer Alternative for Rapid and Efficient Fmoc Deprotection in Solid Phase Peptide Synthesis. *RSC Adv.* **2015**, *5*, 104417–104425.

(144) Tickler, A. K.; Barrow, C. J.; Wade, J. D. Improved Preparation of Amyloid-Peptides Using DBU As N-Fmoc Deprotection Reagent. *J. Pept. Sci.* **2001**, *7*, 488–494.

(145) Behrendt, R.; White, P.; Offer, J. Advances in Fmoc Solid-Phase Peptide Synthesis. *J. Pept. Sci.* **2016**, *22*, 4–27.

(146) Yong, X.; Schoonen, M. A. A. The Absolute Energy Positions of Conduction and Valence Bands of Selected Semiconducting Minerals. *Am. Mineral.* **2000**, *85*, 543–556.

(147) Hines, M. A.; Scholes, G. D. Colloidal PbS Nanocrystals with Size-Tunable Near-Infrared Emission: Observation of Post-Synthesis Self-Narrowing of the Particle Size Distribution. *Adv. Mater.* **2003**, *15*, 1844–1849.

(148) Miller, E. M.; Kroupa, D. M.; Zhang, J.; Schulz, P.; Marshall, A. R.; Kahn, A.; Lany, S.; Luther, J. M.; Beard, M. C.; Perkins, C. L.; *et al.* Revisiting the Valence and Conduction Band Size Dependence of PbS Quantum Dot Thin Films. *ACS Nano* **2016**, *10*, 3302–3311.

(149) Ip, A. H.; Kiani, A.; Kramer, I. J.; Voznyy, O.; Movahed, H. F.; Levina, L.; Adachi, M. M.; Hoogland, S.; Sargent, E. H. Infrared Colloidal Quantum Dot Photovoltaics via Coupling Enhancement and Agglomeration Suppression. *ACS Nano* **2015**, *9*, 8833–8842.

(150) Tang, J.; Wang, X.; Brzozowski, L.; Barkhouse, D. A. R.; Debnath, R.; Levina, L.;

Sargent, E. H. Schottky Quantum Dot Solar Cells Stable in Air under Solar Illumination. *Adv. Mater.* **2010**, *22*, 1398–1402.

(151) Crist, V. B. *Handbook of Monochromatic XPS Spectra*; John Wiley & Sons, Ltd.: West Sussex, England, 2000.

(152) Biniak, S.; Szymański, G.; Siedlewski, J.; Świątkowski, A. The Characterization of Activated Carbons with Oxygen and Nitrogen Surface Groups. *Carbon N. Y.* **1997**, *35*, 1799–1810.

(153) Feng, Q.; Zhao, W.; Wen, S.; Cao, Q. Activation Mechanism of Lead Ions in Cassiterite Flotation with Salicylhydroxamic Acid as Collector. *Sep. Purif. Technol.* **2017**, *178*, 193–199.

(154) Kundu, B.; Pal, A. J. Ligand-Mediated Energy-Level Modification in PbS Quantum Dots as Probed by Density of States (DOS) Spectra. *J. Phys. Chem. C* **2018**, *122*, 11570–11576.

(155) Yang, Z.; Janmohamed, A.; Lan, X.; García De Arquer, F. P.; Voznyy, O.; Yassitepe, E.; Kim, G. H.; Ning, Z.; Gong, X.; Comin, R.; *et al.* Colloidal Quantum Dot Photovoltaics Enhanced by Perovskite Shelling. *Nano Lett.* **2015**, *15*, 7539–7543.

(156) Owen, J. S.; Park, J.; Trudeau, P. E.; Alivisatos, A. P. Reaction Chemistry and Ligand Exchange at Cadmium-Selenide Nanocrystal Surfaces. *J. Am. Chem. Soc.* **2008**, *130*, 12279–12281.

(157) Morris-Cohen, A. J.; Donakowski, M. D.; Knowles, K. E.; Weiss, E. A. The Effect of a Common Purification Procedure on the Chemical Composition of the Surfaces of Cdse Quantum Dots Synthesized with Trioctylphosphine Oxide. *J. Phys. Chem. C* **2010**, *114*, 897–906.

(158) Böhm, M. L.; Kist, R. J. P.; Morgenstern, F. S. F.; Ehrler, B.; Zarra, S.; Kumar, A.; Vaynzof, Y.; Greenham, N. C. The Influence of Nanocrystal Aggregates on Photovoltaic Performance in Nanocrystal-Polymer Bulk Heterojunction Solar Cells. *Adv. Energy Mater.* **2014**, *4*, 1–8.

(159) Zhijun, N.; David, Z.; Valerio, A.; Brandon, S.; Jixian, X.; Oleksandr, V.; Pouya, M.; Xinzheng, L.; Sjoerd, H.; Yuan, R.; *et al.* Graded Doping for Enhanced Colloidal Quantum Dot Photovoltaics. *Adv. Mater.* **2013**, *25*, 1719–1723.

(160) Kloxin, A. M.; Kasko, A. M.; Salinas, C. N.; Anseth, K. S. Photodegradable hydrogels for dynamic tuning of physical and chemical properties. *Science*, **2009**, *324*, 59–63.

(161) DeForest, C. A.; Anseth, K. S. Cytocompatible Click-Based Hydrogels with Dynamically Tunable Properties through Orthogonal Photoconjugation and Photocleavage Reactions. *Nat. Chem.* **2011**, *3*, 925–931.

(162) Dong, Y.; Jin, G.; Hong, Y.; Zhu, H.; Lu, T. J.; Xu, F.; Bai, D.; Lin, M. Engineering the Cell Microenvironment Using Novel Photoresponsive Hydrogels. *ACS Appl. Mater. Interfaces* **2018**, *10*, 12374–12389.

(163) Han, D.; Tong, X.; Zhao, Y. Fast Photodegradable Block Copolymer Micelles for Burst Release. *Macromolecules* **2011**, *44*, 437–439.

(164) Walker, J. W.; Reid, G. P.; McCray, J. A.; Trentham, D. R. Photolabile 1-(2-Nitrophenyl)Ethyl Phosphate Esters of Adenine Nucleotide Analogues. Synthesis and Mechanism of Photolysis. *J. Am. Chem. Soc.* **1988**, *110*, 7170–7177.

(165) Furuta, T.; Wang, S. S.-H.; Dantzker, J. L.; Dore, T. M.; Bybee, W. J.; Callaway, E. M.; Denk, W.; Tsien, R. Y. Brominated 7-Hydroxycoumarin-4-Ylmethyls: Photolabile Protecting Groups with Biologically Useful Cross-Sections for Two Photon Photolysis. *Proc. Natl. Acad. Sci.* **1999**, *96*, 1193–1200.

(166) Pellicciolі, A. P.; Wirz, J. Photoremovable Protecting Groups: Reaction Mechanisms and Applications. *Photochem. Photobiol. Sci.* **2002**, *1*, 441–458.

(167) Zhao, H.; Sterner, E. S.; Coughlin, E. B.; Theato, P. O-Nitrobenzyl Alcohol Derivatives: Opportunities in Polymer and Materials Science. *Macromolecules* **2012**, *45*, 1723–1736.

(168) Iriondo-Alberdi, J.; Greaney, M. F. Photocycloaddition in Natural Product Synthesis. *European J. Org. Chem.* **2007**, 4801–4815.

(169) Ullman, E. F.; Singh, B. Photochemical Transposition of Ring Atoms in Five-Membered Heterocycles. The Photorearrangement of 3,5-Diphenylisoxazole. *J. Am. Chem. Soc.* **1966**, *88*, 1844–1845.

(170) Yoon, T. P.; Ischay, M. A.; Du, J. Visible Light Photocatalysis as a Greener Approach to Photochemical Synthesis. *Nat. Chem.* **2010**, *2*, 527–532.

(171) Schultz, D. M.; Yoon, T. P.; Solar Synthesis: Prospects in Visible Light Photocatalysis. *Science,* **2015**, *6174*.

(172) Prier, C. K.; Rankic, D. A.; MacMillan, D. W. C. Visible Light Photoredox Catalysis with Transition Metal Complexes: Applications in Organic Synthesis. *Chem. Rev.* **2013**, *113*, 5322–5363.

(173) Xuan, J.; Xiao, W. J. Visible-Light Photoredox Catalysis. *Angew. Chemie - Int. Ed.*

2012, *51*, 6828–6838.

(174) Ammala, A.; Bateman, S.; Dean, K.; Petinakis, E.; Sangwan, P.; Wong, S.; Yuan, Q.; Yu, L.; Patrick, C.; Leong, K. H. *An Overview of Degradable and Biodegradable Polyolefins*; Elsevier Ltd, 2011; Vol. 36.

(175) Cho, S.; Choi, W. Solid-Phase Photocatalytic Degradation of PVC–TiO_2 Polymer Composites. *J. Photochem. Photobiol. A Chem.* **2001**, *143*, 221–228.

(176) Kyrikou, I.; Briassoulis, D. Biodegradation of Agricultural Plastic Films: A Critical Review. *J. Polym. Environ.* **2007**, *15*, 125–150.

(177) Johnson, J. A.; Baskin, J. M.; Bertozzi, C. R.; Koberstein, J. T.; Turro, N. J. Copper-Free Click Chemistry for the in Situ Crosslinking of Photodegradable Star Polymers. *Chem. Commun.* **2008**, 3064–3066.

(178) Patchornik, A.; Amit, B.; Woodward, R. B. Photosensitive Protecting Groups. *JACS* **1970**, 6333–6335.

(179) Green, T. W.; Wuts, P. G. M. *Protecting Groups in Organic Synthesis*; Wiley-Interscience: New York, 1999.

(180) Johnson, E. C. B.; Kent, S. B. H. Synthesis, Stability and Optimized Photolytic Cleavage of 4-Methoxy-2-Nitrobenzyl Backbone-Protected Peptides. *Chem. Commun.* **2006**, 1557–1559.

(181) Aujard, I.; Benbrahim, C.; Gouget, Ma.; Ruel, O.; Baudin, J.-B.; Neveu, P.; Jullien, L. O-Nitrobenzyl Photolabile Protecting Groups with Red-Shifted Absorption: Syntheses and Uncaging Cross-Sections for One- and Two-Photon Excitation. *Chem. Eur. J.* **2006**, *12*, 6865–6879.

(182) Atilgan, A.; Tanriverdi Eçik, E.; Guliyev, R.; Uyar, T. B.; Erbas-Cakmak, S.; Akkaya, E. U. Near-IR-Triggered, Remote-Controlled Release of Metal Ions: A Novel Strategy for Caged Ions. *Angew. Chemie - Int. Ed.* **2014**, *53*, 10678–10681.

(183) Yuri V. Il'ichev, †; Markus A. Schwörer, ‡ and; Wirz*, J. Photochemical Reaction Mechanisms of 2-Nitrobenzyl Compounds: Methyl Ethers and Caged ATP. **2004**.

(184) Hoffmann, N. Photochemical Reactions as Key Steps in Organic Synthesis. *Chem. Rev.* **2008**, *108*, 1052–1103.

(185) Hu, X.; Qureishi, Z.; Thomas, S. W. Light-Controlled Selective Disruption, Multilevel Patterning, and Sequential Release with Polyelectrolyte Multilayer Films Incorporating Four Photocleavable Chromophores. *Chem. Mater.* **2017**, *29*, 2951–2960.

(186) Kim, M. S.; Diamond, S. L. Photocleavage of O-Nitrobenzyl Ether Derivatives for Rapid Biomedical Release Applications. *Bioorganic Med. Chem. Lett.* **2006**, *16*, 4007–4010.

(187) Kevwitch, R. M.; McGrath, D. V. Synthesis and Degradation of Photolabile Dendrimers Based on O-Nitrobenzyl Ether Photolabile Cores. *New J. Chem.* **2007**, *31*, 1332–1336.

(188) Shi, L.; Santhanakrishnan, S.; Cheah, Y. S.; Li, M.; Chai, C. L. L.; Neoh, K. G. One-Pot UV-Triggered o-Nitrobenzyl Dopamine Polymerization and Coating for Surface Antibacterial Application. *ACS Appl. Mater. Interfaces* **2016**, *8*, 33131–33138.

(189) Berr, M. J.; Wagner, P.; Fischbach, S.; Vaneski, A.; Schneider, J.; Susha, A. S.; Rogach, A. L.; Jäckel, F.; Feldmann, J. Hole Scavenger Redox Potentials Determine Quantum Efficiency and Stability of Pt-Decorated CdS Nanorods for Photocatalytic Hydrogen Generation. *Appl. Phys. Lett.* **2012**, *100*, 223903.

(190) Pocker, Y.; Davison, B. L.; Deits, T. L. Decarboxylation of Monosubstituted Derivatives of Carbonic Acid. Comparative Studies of Water- and Acid-Catalyzed Decarboxylation of Sodium Alkyl Carbonates1 in H_2O and D_2O_2. *J. Am. Chem. Soc.* **1978**, *100*, 3564–3567.

(191) Tavasli, M.; Moore, T. N.; Zheng, Y.; Bryce, M. R.; Fox, M. A.; Griffiths, G. C.; Jankus, V.; Al-Attar, H. A.; Monkman, A. P. Colour Tuning from Green to Red by Substituent Effects in Phosphorescent Tris-Cyclometalated Iridium(III) Complexes of Carbazole-Based Ligands: Synthetic, Photophysical, Computational and High Efficiency OLED Studies. *J. Mater. Chem.* **2012**, *22*, 6419–6428.

(192) Watts, P.; Long, G.; Meek, M. E. Concise International Chemical Assessment Document (CICAD): A New Chemical Safety Series in IPCS, Internationalizing National Reviews. *Concise Int. Chem. Assess. Doc. 58* **2004**, 1–64.

(193) Baert, J. J.; Clippeleer, J. De; Cooman, L. De; Aerts, G.; Leuven, K. U. Exploring the Binding Behavior of Beer Staling Aldehydes in Model Systems. *J. Am. Soc. Brew. Chem.* **2015**.

(194) Eranna, G.; Joshi, B. C.; Runthala, D. P.; Gupta, R. P. Oxide Materials for Development of Integrated Gas Sensors—A Comprehensive Review. *Crit. Rev. Solid State Mater. Sci.* **2004**, *29*, 111–188.

(195) Meyer, J.; Hamwi, S.; Kröger, M.; Kowalsky, W.; Riedl, T.; Kahn, A. Transition Metal Oxides for Organic Electronics: Energetics, Device Physics and Applications. *Adv. Mater.* **2012**, *24*, 5408–5427.

(196) Özgür, Ü.; Alivov, Y. I.; Liu, C.; Teke, A.; Reshchikov, M. A.; Doğan, S.; Avrutin, V.; Cho, S. J.; Morkọ, H. A Comprehensive Review of ZnO Materials and Devices. *J. Appl. Phys.* **2005**, *98*, 1–103.

(197) Diebold, U. The Surface Science of Titanium Dioxide. *Surf. Sci. Rep.* **2003**, *48*, 53–229.

(198) Yang, J.; Ling, T.; Wu, W. T.; Liu, H.; Gao, M. R.; Ling, C.; Li, L.; Du, X. W. A Top-down Strategy towards Monodisperse Colloidal Lead Sulphide Quantum Dots. *Nat. Commun.* **2013**, *4*, 1695–1696.

(199) Bierman, M. J.; Lau, Y. K. A.; Jin, S. Hyperbranched PbS and PbSe Nanowires and the Effect of Hydrogen Gas on Their Synthesis. *Nano Lett.* **2007**, *7*, 2907–2912.

(200) Kane, R. S.; Cohen, R. E.; Silbey, R. Synthesis of PbS Nanoclusters within Block Copolymer Nanoreactors. *Chem. Mater.* **1996**, *8*, 1919–1924.

(201) Dutta, A. K.; Ho, T.; Zhang, L.; Stroeve, P. Nucleation and Growth of Lead Sulfide Nano- and Microcrystallites in Supramolecular Polymer Assemblies. *Chem. Mater.* **2000**, *12*, 1042–1048.

(202) Parvathy, N. N.; Pajonk, G. M.; Rao, A. V. Synthesis and Study of Quantum Size Effect, XRD and IR Spectral Properties of PbS Nanocrystals Doped in SiO_2 Xerogel Matrix. *J. Cryst. Growth* **1997**, *179*, 249–257.

(203) Schneider, T.; Haase, M., Kornowski, A., Naused, S., and Wller, H. Synthesis and Characterization of PbS Nanoparticles in Block Copolymer Micelles. *Ber, Bunsenges. Phys. Chem.* **1997**. *101*, 1654–1656.

(204) Lipovskii, a. Synthesis of Monodisperse PbS Quantum Dots in Phosphate Glass. *Phys. E Low-dimensional Syst. Nanostructures* **1999**, *5*, 157–160.

(205) Cao, H.; Wang, G.; Zhang, S.; Zhang, X. Growth and Photoluminescence Properties of PbS Nanocubes. *Nanotechnology* **2006**, *17*, 3280–3287.

(206) Wang, N.; Cao, X.; Guo, L.; Yang, S.; Wu, Z. Facile Synthesis of PbS Truncated Octahedron Crystals with High Symmetry and Their Large-Scale Assembly into Regular Patterns by a Simple Solution Route. *ACS Nano* **2008**, *2*, 184–190.

(207) Wang, Y.; Tang, A.; Li, K.; Yang, C.; Wang, M.; Ye, H.; Hou, Y.; Teng, F. Shape-Controlled Synthesis of Pbs Nanocrystals via a Simple One-Step Process. *Langmuir* **2012**, *28*, 16436–16443.

(208) Liu, Z.; Liang, J.; Xu, D.; Lu, J.; Qian, Y. A Facile Chemical Route to Semiconductor Metal Sulfide Nanocrystal.Pdf. *Chem. Commun.* **2004**, 2724–2725.

(209) Joo, J.; Na, H. Bin; Yu, T.; Yu, J. H.; Kim, Y. W.; Wu, F.; Zhang, J. Z.; Hyeon, T. Generalized and Facile Synthesis of Semiconducting Metal Sulfide Nanocrystals. *JACS*. **2003**. *125*, 11100-11105.

(210) Chintso, T.; Ajibade, P. A. Synthesis and Structural Studies of Hexadecylamine Capped Lead Sulfide Nanoparticles from Dithiocarbamate Complexes Single Source Precursors. *Mater. Lett.* **2015**, *141*, 1–6.

(211) Zhang, Z.; Lee, S. H.; Vittal, J. J.; Chin, W. S. A Simple Way to Prepare PbS Nanocrystals with Morphology Tuning at Room Temperature. *J. Phys. Chem. B* **2006**, *110*, 6649–6654.

(212) Moreels, I.; Martins, J. C.; Hens, Z. Ligand Adsorption/Desorption on Sterically Stabilized InP Colloidal Nanocrystals: Observation and Thermodynamic Analysis. *ChemPhysChem* **2006**, *7*, 1028–1031.

(213) Turo, M. J.; Shen, X.; Brandon, N. K.; Castillo, S.; Fall, A. M.; Pantelides, S. T.; Macdonald, J. E.; Yin, Y.; Alivisatos, A. P.; Owen, J. S.; *et al.* Dual-Mode Crystal-Bound and X-Type Passivation of Quantum Dots. *Chem. Commun.* **2016**, *52*, 12214–12217.

(214) Anderson, N. C.; Hendricks, M. P.; Choi, J. J.; Owen, J. S. Ligand Exchange and the Stoichiometry of Metal Chalcogenide Nanocrystals: Spectroscopic Observation of Facile Metal-Carboxylate Displacement and Binding. *J. Am. Chem. Soc.* **2013**, *135*, 18536–18548.

(215) Jiang, D. E.; Tiago, M. L.; Luo, W.; Dai, S. The “Staple” Motif: A Key to Stability of Thiolate-Protected Gold Nanoclusters. *J. Am. Chem. Soc.* **2008**, *130*, 2777–2779.

(216) Qian, H.; Eckenhoff, W. T.; Zhu, Y.; Pintauer, T.; Jin, R. Total Structure Determination of Thiolate-Protected Au_{38} Nanoparticles. *J. Am. Chem. Soc.* **2010**, *132*, 8280–8281.

(217) Zeng, C.; Li, T.; Das, A.; Rosi, N. L.; Jin, R. Chiral Structure of Thiolate-Protected 28-Gold-Atom Nanocluster Determined by X-Ray Crystallography. *J. Am. Chem. Soc.* **2013**, *135*, 10011–10013.

(218) Heaven, M. W.; Dass, A.; White, P. S.; Holt, K. M.; Murray, R. W. Crystal Structure of the Gold Nanoparticle $[N(C_8H_{17})_4][Au_{25}(SCH_2CH_2Ph)_{18}]$. *J. Am. Chem. Soc.* **2008**, *130*, 3754–3755.

(219) Watson, E. S.; O’Neill, M. J.; Justin, J.; Brenner, N. A Differential Scanning Calorimeter for Quantitative Differential Thermal Analysis. *Anal. Chem.* **1964**, *36*, 1233–1238.

(220) O'Neill, M. J. The Analysis of a Temperature-Controlled Scanning Calorimeter. *Anal. Chem.* **1964**, *36*, 1238–1245.

(221) Silva, L. A.; Matos, J. R.; De Andrade, J. B. Synthesis, Identification and Thermal Decomposition of Double Sulfites like $Cu_2SO_3 \cdot MSO_3 \cdot 2H_2O$ (M = Cu, Fe, Mn or Cd). *Thermochim. Acta* **2000**, *360*, 17–27.

(222) Ahrenstorf, K.; Heller, H.; Kornowski, A.; Broekaert, J. A. C.; Weller, H. Nucleation and Growth Mechanism of NixPt1-x Nanoparticles. *Adv. Funct. Mater.* **2008**, *18*, 3850–3856.

(223) Li, H.; Brescia, R.; Povia, M.; Prato, M.; Bertoni, G.; Manna, L.; Moreels, I. Synthesis of Uniform Disk-Shaped Copper Telluride Nanocrystals and Cation Exchange to Cadmium Telluride Quantum Disks with Stable Red Emission. *J. Am. Chem. Soc.* **2013**, *135*, 12270–12278.

(224) Xie, Y.; Riedinger, A.; Prato, M.; Casu, A.; Genovese, A.; Guardia, P.; Sottini, S.; Sangregorio, C.; Miszta, K.; Ghosh, S.; *et al.* Copper Sulfide Nanocrystals with Tunable Composition by Reduction of Covellite Nanocrystals with Cu+ions. *J. Am. Chem. Soc.* **2013**, *135*, 17630–17637.

(225) Jose Aldana; Y. Andrew Wang, and; Peng*, X. Photochemical Instability of CdSe Nanocrystals Coated by Hydrophilic Thiols. *JACS.* **2001**. *123*, 8844-8850.

(226) Wise, F. W. Lead Salt Quantum Dots: The Limit of Strong Quantum Confinement. *Acc. Chem. Res.* **2000**, *33*, 773–780.

(227) Pattantyus-Abraham, A. G.; Kramer, I. J.; Barkhouse, A. R.; ... Depleted-Heterojunction Colloidal Quantum Dot Solar Cells. *Acs ...* **2010**, *4*, 3374–3380.

(228) Mcdonald, S. A.; Konstantatos, G.; Zhang, S.; Cyr, P. W.; Klem, E. J. D.; Levina, L.; Sargent, E. H. Solution-Processed PbS Quantum Dot Infrared Photodetectors and Photovoltaics. *Nat. Mater.* **2005**, *4*, 138–142.

(229) Lee, H.; Leventis, H. C.; Moon, S. J.; Chen, P.; Ito, S.; Haque, S. A.; Torres, T.; Nüesch, F.; Geiger, T.; Zakeeruddin, S. M.; *et al.* PbS and CdS Quantum Dot-Sensitized Solid-State Solar Cells: "Old Concepts, New Results." *Adv. Funct. Mater.* **2009**, *19*, 2735–2742.

(230) Hyun, B. R.; Zhong, Y. W.; Bartnik, A. C.; Sun, L. F.; Abruna, H. D.; Wise, F. W.; Goodreau, J. D.; Matthews, J. R.; Leslie, T. M.; Borrelli, N. F. Electron Injection from Colloidal PbS Quantum Dots into Titanium Dioxide Nanoparticles. *ACS Nano* **2008**, *2*, 2206–2212.

(231) Aldana, J.; Wang, Y. A.; Peng, X. Photochemical Instability of CdSe Nanocrystals Coated by Hydrophilic Thiols. *J. Am. Chem. Soc.* **2001**, *123*, 8844–8850.

(232) Jacobson, M. Z. Review of Solutions to Global Warming, Air Pollution, and Energy Security. *Energy Environ. Sci.* **2009**, *2*, 148–173.

(233) Naik, S. N.; Goud, V. V.; Rout, P. K.; Dalai, A. K. Production of First and Second Generation Biofuels: A Comprehensive Review. *Renew. Sustain. Energy Rev.* **2010**, *14*, 578–597.

(234) Lunsford, J. H. Catalytic Conversion of Methane to More Useful Chemicals and Fuels:A Challenge for the 21st Century. *Catal. Today* **2000**, *63*, 165–174.

(235) Tseng, H. W.; Wilker, M. B.; Damrauer, N. H.; Dukovic, G. Charge Transfer Dynamics between Photoexcited CdS Nanorods and Mononuclear Ru Water-Oxidation Catalysts. *J. Am. Chem. Soc.* **2013**, *135*, 3383–3386.

(236) Das, A.; Han, Z.; Haghighi, M. G.; Eisenberg, R. Photogeneration of Hydrogen from Water Using CdSe Nanocrystals Demonstrating the Importance of Surface Exchange. *Proc. Natl. Acad. Sci. U. S. A.* **2013**, *110*, 16716–16723.

(237) Barnett P., T.; Adam C., J.; Lettenmaier P., D. Potential Impacts of a Warming Climate on Water Availability in Snow-Dominated Regions. *Nature* **2005**, *438*, 303–309.

(238) R.J. Charlson, S.E. Schwartz, J.M. Hales, R.D. Cess, J.A. Coakley, Jr. and J.E. Hansen . Climate Forcing by Anthropogenic Aerosols. *Onefile.* **2018**, *5043*, 1–13.

(239) Allen, C. D.; Macalady, A. K.; Chenchouni, H.; Bachelet, D.; McDowell, N.; Vennetier, M.; Kitzberger, T.; Rigling, A.; Breshears, D. D.; Hogg, E. H. Ted.; *et al.* A Global Overview of Drought and Heat-Induced Tree Mortality Reveals Emerging Climate Change Risks for Forests. *For. Ecol. Manage.* **2010**, *259*, 660–684.

(240) McMichael, A. J.; Woodruff, R. E.; Hales, S. Climate Change and Human Health: Present and Future Risks. *Lancet* **2006**, *367*, 859–869.

(241) I.Moreels; K.Lambert; D.Smeets; D.DeMuynck; T.Nollet; Martins, J. C.; F.Vanhaecke; A.Vantomme; C.Delerue; G.Allan; *et al.* Size-Dependent Optical Properties of Colloidal {PbS} Quantum Dots. *ACS Nano* **2009**, *3*, 3023–3030.

(242) Cademartiri, L.; Montanari, E.; Calestani, G.; Migliori, A.; Guagliardi, A.; Ozin, G. A. Size-Dependent Extinction Coefficients of PbS Quantum Dots. *J. Am. Chem. Soc.* **2006**, *128*, 10337–10346.

(243) Coblentz Society, Inc., "Evaluated Infrared Reference Spectra" in **NIST Chemistry**

WebBook, NIST Standard Reference Database Number 69, Eds. P.J. Linstrom and W.G. Mallard. National Institute of Standards and Technology, Gaithersburg MD, 20899, doi:10.18434/T4D303, (retrieved September 18, 2018).

APPENDICES

A. Additional Synthetic Procedures for Chapter 2

General Notes

All glassware was thoroughly dried in an oven before use. Schlenk line technique with Argon was used in all reactions. A J-KEM Scientific Model 210 temperature controller was used to control the temperature of all reactions unless otherwise noted. All solvents and reagents were used as received unless otherwise noted.

UV/Vis spectra were recorded on a Jasco V-670 spectrophotometer using quartz cuvettes. A baseline was first recorded without any reference cuvette, and then samples were recorded with a background of the appropriate neat solvent in the reference cuvette. Fluorescence spectra were recorded on a Jasco FP-3800 spectrofluorometer. QY measurements were made using rhodamine B as a standard. TEM images were taken on a Phillips CM-20 TEM and sized using ImageJ. NMR spectra were taken using a Bruker DRX-400 (400 MHz) spectrometer. Spectra were calibrated to residual solvent signals of 7.26 and 77.0 ppm for ^{1}H and ^{13}C NMR spectra, respectively, in CDCl3. Spectra were calibrated to 4.79 ppm for ^{1}H in D2O.

Materials

Selenium Powder (99.99%) and cadmium oxide (99.999%) were purchased from Strem Chemicals Inc. Trioctylphosphine (TOP, 90%), Trioctylphosphine oxide (TOPO, 99%), Sulfur, 2,2'-dipyridiyl-n-oxide (98%), methylene chloride (≥99.8%), anhydrous magnesium sulfate (≥97%), anhydrous tetrahydrofuran (THF, ≥99.9%), zinc dust (<10 μm, ≥98%), hydrochloric acid (37%), ammonium chloride (≥99.5%), ethyl acetate (≥99.7%), ammonium hydroxide (28.0-30.0%), iron (III) acetylacetonate (≥99.9%), and anhydrous pyridine (99.8%) were purchased from Sigma-Aldrich. HPLC grade toluene, concentrated nitric acid, sodium hydroxide (98.9%), 2-propanol, and anhydrous ethyl ether were purchased from Fisher Scientific. Octadecylphosphonic acid and hexylphosphonic acid were purchased from PCI Synthesis. Ethylenediaminetetraacetic acid (99%) and carbon disulfide (99.9+%) were purchased from Alfa-Aesar. 200 proof ethanol was purchased from Decon Laboratories Inc. Concentrated sulfuric acid was purchased from EMD chemicals. All chemicals were used without further purification unless otherwise noted.

Synthesis of CdSe Nanoparticles

Preparation of Se Precursor: In a glove box, Se (0.058 g, 0.734 mmol) was added to a 1 dram vial containing TOP (0.430 ml, 0.964 mmol) and a stir bar. The Se was dissolved with heat and stirring. Prior to injection, the optically clear, colorless solution was drawn into a 10 ml polypropylene syringe with an 18 gauge needle and plugged into a septa for removal from the glove box

In a typical synthesis, TOPO (3.0 g, 7.76 mmol), ODPA (0.28 g, 0.84 mmol), and CdO (0.06 g, 0.47 mmol) were added to a 25 ml three-neck round bottom flask equipped with a stir bar, two rubber septa, condenser, and inlet adapter attached to a Schlenk line. The mixture was degassed at 150 °C under vigorous stirring for 1 hour. The reaction was then flushed with Ar and heated to 310 °C where the CdO dissolved to form an optically clear, colorless solution. TOP (1.8 ml, 4.03 mmol) was injected into the flask, and the reaction was heated to 380 °C. The heating mantle was removed and replaced by an evaporating dish. As the temperature fell past 370 °C, the Se precursor was injected. The flask was immediately sprayed with acetone until the temperature fell below 200 °C, were 10 ml of toluene were injected. The solution was split between two 6 dram vials and particles cleaned via three successive crashes using ethanol as a bad solvent and toluene for particle dispersion (centrifugation for 5 minutes at 4400 rpm).

Synthesis of CdSe/CdS Nanorods

Preparation of Seed/Sulfur Precursor: Sulfur (0.06 g, 1.87 mmol) was added to a 1 dram vial, followed by 8 x 10^{-8} mol of CdSe seeds, as determined by the absorbance of the stock seed solution at the first absorption peak.[1] The solution was evacuated and flushed with Ar 3 times on a Schlenk line, and then TOP was added (1.8 ml, 4.03 mmol). The sulfur was dissolved with vortexing.

In a typical synthesis, TOPO (3.0 g, 7.76 mmol), ODPA (0.29 g, 0.67 mmol), and CdO (0.075 g, 0.584 mmol) were added to a 25 ml three-neck round bottom flask equipped with a stir bar, two rubber septa, condenser, and inlet adapter attached to a Schlenk line. The reaction was degassed at 150 °C for 30 minutes. The flask was then flushed with Ar and heated to 355 °C. A clear, colorless solution was observed. TOP (1.8 ml, 4.03 mmol) was injected and the temperature was allowed to recover. The aluminum foil was removed and cotton wrapped around the glass wool (cotton was necessary for quick temperature recovery, but was watched closely as it was an inherent fire hazard). The reaction was allowed to equilibrate for 5 minutes past the cotton swaddling. The seed/sulfur solution was then quickly injected into the flask. Temperature recovery above 350 °C was observed within 90 seconds of injection. After 6 minutes of growth time the heating mantle was removed and reaction allowed to cool. At 100 °C 10 ml of toluene was injected. The solution was split between two 6 dram vials and precipitated via three successive crashes using ethanol as a bad solvent and toluene for particle dispersion (centrifugation for 5 minutes at 4400 rpm). QY 85.3%, length 45.7 ± 5.2 nm, diameter 6.0 ± 0.8 nm n=120

Synthesis of ammonium-[2,2'-bipyridin]-4-ylcarbamodithioate (**1**)

*4-nitro-[2,2'-bipyridine] 1-oxide (***3***).* 2,2'-dipyridyl *N*-oxide, **2**, (1.72 g, 10 mmol) was added to a 50 ml three-neck round bottom flask. 20 ml of concentrated H_2SO_4 was added and the reaction vessel was flushed with Ar for 1 min. The solid was dissolved with stirring at 100°C in an oil bath. Concentrated HNO_3 (4.2 ml, 100 mmol) was added over 17 h via a syringe pump using a disposable polypropylene syringe and PTFE tubing. The reaction was allowed to continue for an additional 2 h at 100°C, and then the reaction flask was removed from the oil bath and allowed to cool. 30 g of NaOH dissolved in 30 ml of H_2O was used to render the solution slightly basic in an ice bath. As the pH of the solution rose, solid formed which prevented the reaction from stirring; the addition of extra H_2O alleviated this problem. The basic solution was extracted with dichloromethane (3 x 30 ml), and the combined organics were washed with 1 M NaOH (2 x 25 ml) and brine (1 x 25 ml) before being dried over $MgSO_4$. The solvent was removed under reduced pressure to produce yellow crystals which were recrystallized from isopropanol (Yield 41%). Spectra shown below (Figure S6a). ^1H NMR (400MHz, $CDCl_3$) δ 9.18 (d, 1H, J=3.3Hz), 8.90 (d, 1H, J=8.1 Hz), 8.80 (dm, 1H, J=4.9 Hz), 8.37 (d, 1H, J=7.2 Hz), 8.07 (dd, 1H J=3.9, 7.2 Hz), 7.89 (td, 1H, J=1.8, 7.8 Hz), 7.44 (ddd, 1H, J=1.1, 4.8, 7.5 Hz). ^{13}C NMR (100 MHz, $CDCl_3$) δ 149.8, 147.5, 141.9, 136.6, 125.3, 125.0, 122.6, 118.8 ppm (ArC).

*4-amino-2,2'-bipyridine (***4***).* 4-nitro-2,2'-dipyridyl *N*-oxide, **3**, (0.217 g, 1 mmol) was added to a 50 ml three-neck round bottom flask. The flask was evacuated and flushed with Ar three times. 15 ml of THF was added to the flask and the solid dissolved. Zn dust (0.9807 g, 15 mmol) was activated via successive washes with 2% HCl, H_2O, EtOH, and Et_2O. 15 ml 30% (w/v) NH_4Cl solution was added followed by the Zn dust. The reaction was brought to 60°C under Ar for 3 h. The reaction was removed from heat, and 25 ml of 1 M EDTA was added to quench the reaction. Excess Zn dust was removed via vacuum filtration with a Büchner funnel. THF was removed under reduced pressure. The remaining aqueous layer was made basic with 1 M NaOH, then extracted with ethyl acetate (3 x 25 ml). The combined organics were washed with 1 M NaOH (2 x 15 ml) and brine (1 x 15 ml) before being dried over $MgSO_4$. The solvent was removed under reduced pressure to produce an off-white crystal (Yield 76%). Spectra shown below (Figure S6b). ^1H NMR (400 MHz, $CDCl_3$) δ 8.60 (d, 1H, J=4.6 Hz), 8.31 (d, 1H, J=8 Hz), 8.25 (d, 1H, J=5.5 Hz), 7.75 (tm, 1H, J=6.9 Hz), 7.63 (s, 1H), 7.24 (tm, 1H, J=5.9 Hz), 6.50 (m, 1H), 4.43 (br, 2H, -NH2). ^{13}C NMR (100 MHz, CDCl3) δ 156.5, 156.2, 153.8, 149.7, 148.8, 136.9, 123.5, 121.2, 109.5, 106.8 ppm (ArC).

*Ammonium-[2,2'-bipyridin]-4-ylcarbamodithioate (**1**).* 4-amino-2,2'-bipyridine (**4**) (0.085 g, 0.5 mmol) was added to a 6 dram vial and capped with a septa. The vial was evacuated and flushed with Ar three times. 1.5 ml of EtOH was added and the solid was dissolved. NH_4OH (0.04 ml) was added, followed by CS_2 (0.09 ml, 1.5 mmol). After no reaction had occurred for several minutes, an excess of CS_2 (0.36 ml, 6 mmol) was added, followed by NH_4OH (0.55 ml). Within 1 min, the reaction turned from tan to yellow, and white precipitate formed. After 5 min, the supernatant was clear and orange. After one hour, the solvents were removed under reduced pressure, and the resulting solid was triturated with EtOH (3 x 3 ml) to produce a pale yellow solid (Yield 77%). Spectra shown below (Figure S6C-D).

^1H NMR (400 MHz, DMSO-d6) δ 8.75 (d, 1H, J=4.4 Hz) 8.22 (d, 1H, J=8.0 Hz), 8.13 (d, 1H, J=6.5 Hz), 8.03 (td, 1 H, J=1.7, 7.8 Hz), 7.69 (br, 4H, NH_4), 7.60 (d, 1H, J=2.3 Hz), 7.57 (dd, 1H, J=5.4, 7.2 Hz), 6.76 (dd, 1H, J=2.3, 6.5 Hz), 3.36 (br, 1H, NH).

^{13}C NMR (100 MHz, DMSO) δ 217.7 (CS2), 157.3, 149.6, 146.7, 137.8, 130.3, 125.0, 121.2, 109.3, 106.1 (ArC) ppm. Anal. Calcd. for $C_{11}H_{12}N_4S_2$: C, 49.98; H, 4.58; N, 21.19; S, 24.25. Found: C, 49.85; H, 4.90; N, 21.08; S, 24.02.

Coordination of Ligands to Nanostructures

In a typical exchange, $2.26 * 10^{-10}$ moles of rods (as determined by previously established methods)[1] were taken from a stock solution and added to 2.5 ml of toluene in a quartz fluorescence cuvette. Fluorescence and UV-Vis spectra of the NP were recorded. A solution of DTCBipy and toluene was prepared (typically ~0.5mM) and DTCBipy was added in solution with toluene so that 4.5 ligands were introduced per nm^2 of NP surface area. Spectra were recorded again before the vial was flushed with Ar and allowed to stir in the dark for 16 hours. After 16 hours the spectra were recorded again, and $Fe(acac)_3$ three was added from a solution of toluene in an equimolar amount to the added DTCBipy. The vial was then flushed with Ar and allowed to stir under Ar in the dark for 24 hours. Spectra were then recorded, and the particles were precipitated from solution via centrifugation for 5 minutes at 4.4k rpm. The NP were redispersed in toluene, then precipitated again via centrifugation for 5 minutes at 4.4k rpm. The NP were then redispersed in toluene with a sonicator. Upon standing, the particles would precipitate from solution, but further sonication would afford an optically clear solution.

Formation of DTCBipy Complex in the absence of nanorods

A solution of 11.2 mg ($3.17 * 10^{-5}$ moles) of $Fe(acac)_3$ in 10 ml of toluene was added to a 25 ml three neck round bottom flask. A stir bar was added and the reaction was capped with a septa and flushed with Ar. Separately 13.2 mg ($5.0 * 10^{-5}$ moles) of DTCBipy was dissolved in 10 ml of toluene. 6.35 ml of the DTCBipy solution was added to the $Fe(acac)_3$ solution to form an equimolar amount of iron to DTCBipy. The solution was allowed to stir overnight (16 hours). The next morning the pink crystals were collected via centrifugation and allowed to dry. Analysis of the compound via UV-Vis (Figure S2A) produced the redshift seen in nanorod DTCBipy-Fe formation. NMR (Figure S1) verified the existence of a low spin complex, since when considering Fe^{3+} LS, Fe^{3+} HS, Fe^{2+} LS, and Fe^{2+} HS only Fe^{2+} LS offers a diamagnetic spin state. ^{1}H NMR (400 MHz, MeOD) δ 8.75 (d, 1H, J=4.88 Hz), 8.14 (d, 1H, J=8.12 Hz), 8.10 (d, 1H, J=6.6 Hz), 8.02 (td, 1H, J=1.6, 7.76 Hz), 7.56 (dd, 1H, J=4.8 Hz, 7.4 Hz), 7.48 (d, 1H, J=2.32 Hz), 6.82 (dd, 1H, J=2.32, 6.64 Hz)

A.1. Quantitative TEM-EDS Procedures

EDS Spectra were acquired using a Tecnai Osiris operating at 200 kV. Rods were drop cast onto a Ni TEM grid. A collection of rods was located, and EDS spectra were acquired for 5 minutes. Using Bruker Espirit software the resulting spectra was matched for all elements present, and deconvoluted to exclude all elements except for Cd, S, Se, and Fe to give the atomic % of the elements present. This procedure was repeated ten times in different grid boxes each time. To calculate the number of Fe atoms per nm^2, it was assumed that the observed sample was representative of the entire NR population, and thus the data was representative of a single rod. The number of Cd present in a single rod was calculated based off of rod volume and unit cell volume as determined by measuring via ImageJ. This number was then used to calculate total atoms present, then the number of Fe present was taken from this number. The number of Fe per rod was divided by the surface area of the rod to deduce Fe coverage. The raw data can be seen in Table B.1. below.

Table A. 1.

Sample	% Cd	% Cd decimal form	atoms per rod	% Fe	% Fe decimal form	Fe per rod	Fe/nm^2
1	49.2	0.492	5.34E+04	4.79	0.0479	2.56E+03	2.77
2	49.6	0.496	5.30E+04	3.74	0.0374	1.98E+03	2.14
3	49.6	0.496	5.30E+04	4.10	0.0410	2.18E+03	2.36
4	49.7	0.497	5.29E+04	4.51	0.0451	2.39E+03	2.58
5	49.6	0.496	5.31E+04	4.55	0.0455	2.41E+03	2.61
6	51.6	0.516	5.09E+04	3.75	0.0375	1.91E+03	2.07
7	51.8	0.518	5.08E+04	4.03	0.0403	2.05E+03	2.22
8	51.0	0.510	5.16E+04	3.91	0.0391	2.02E+03	2.18
9	50.7	0.507	5.19E+04	3.80	0.0380	1.97E+03	2.13
10	50.8	0.508	5.18E+04	5.37	0.0537	2.78E+03	3.01
	Cd per rod		SA rod (nm^2)			Average	2.41E+00
	2.63E+04		923.92			Std. dev	3.20E-01

A.2. Additional Computational Procedures

Density functional theory calculations were performed using the Vienna *ab initio* Simulation Package (VASP).[4] The projector augmented wave method[5, 6] was used to describe the interactions between valence and core electrons and the plane-wave basis cutoff was taken to be 950 eV. For molecules, only the Γ was used, while surface slabs used a $2\times2\times1$ Γ-centered Monkhorst-Pack grid[7] during relaxations. Integration was performed with Gaussian broadening with σ = 0.05 eV for all calculations, while absorption spectra were calculated with σ = 0.2 eV. At least 10 Å of vacuum were used to minimize interactions between periodic images. The structures were relaxed using the conjugant gradient method until forces were less than 0.02 eV/Å. During structural optimization, the Perdew-Burke-Ernzerhof (PBE)[8] version of the generalized gradient approximation (GGA) was used to describe the exchange-correlation functional, while the HSE06 range separated hybrid functional[9, 10] was used for calculation of the electronic structure.

Simple calculations of the ligand system alone were performed to predict if there is good spatial and energetic alignment of the ligand states with CdS valence and conduction band energies, before attempting more computationally costly calculations of the hybridized system. We find that the HOMO and HOMO-1 energy levels of [2,2'-bipyridin]-4-ylcarbamodithioic acid (HDTCBipy) comprise primarily the sulfur orbitals of the dithiocarbamate functional group, and are energetically 0.03 eV and 0.24 eV higher than the CdS valence band relative to the vacuum level. The calculations indicate there is a good energetic and spatial alignment of the HOMO levels of DTCBipy for hybridization with the CdS valence band. Calculations were also performed for HDTCBipyFe(acac)$_2$. Two filled dithiocarbamate orbitals, similar to HDTCBipy, lie 0.05 eV below and 0.04 eV above the CdS valence band. Additionally, there are two filled molecular states with contribution from the dithiocarbamate and bipyridine at 0.50 and 0.83 eV above the valence band. Above this, are three new additional occupied orbitals comprised primarily of Fe-related states. The calculations again predict the plausibility of advantageous hybridization of the iron chelated ligand system with CdS for hole transfer.

In order to determine the ability for hole transfer from the valence band to the ligand to occur, we use density functional theory to calculate the dipole transition oscillator strengths. Then, the rate of spontaneous emission can be evaluated as:

$$\Gamma_R = \frac{(\Delta E_{21})^3}{3\pi\varepsilon_0\hbar^4c^3}|\mu_{21}|^2, \tag{1}$$

where the dipole matrix element can be extracted from the DFT computed oscillator strength via:

$$f_{21} = \frac{2m_e}{3\hbar^2e^2}\Delta E_{21}|\mu_{21}|^2. \tag{2}$$

The lifetime for an excitation is given by $\tau = 1/\Gamma$. The oscillator strengths themselves can be computed through the use of the optical routines implemented in VASP in one of two ways. The first is from the matrix elements obtained through calculation of the frequency-dependent dielectric matrix. In a typical calculation done this way, however, the matrix elements and oscillator strengths are not readily readable. The alternative way is to use what essentially amounts to the TD-DFT derived version of the Bethe-Salpeter equation for the optical absorption. These routines can be applied in the single-particle framework and yield the same values as the previous method, but with the desired oscillator strengths user-accessible. Ordinarily, the use of these routines is for determining the optical properties from the electronic ground state and hence calculated between the valence states (or HOMO-n levels) and conduction states (or LUMO+m levels). In order to determine the oscillator strength between levels that are all ordinarily occupied prior to photoexcitation (in our case the CdS valence band and the molecular states), VASP allows for the wave functions to be constrained or "frozen" to their original form and the occupations to be set manually. This is done after the self-consistent optimization and before the calculation of the oscillator strengths for valence to molecular transitions. For example, in our pristine CdS surface with no adsorbed ligands, we can calculate the lifetime to be 0.8 ns. This is in relative agreement with measurements on large sample CdS systems.[11] For the purposes of testing for hole transfer to the molecular states, the comparison for radiative decay rates should actually be made not to pure CdS, but rather DTC-ligand free CdSe-CdS core-shell nanorods. The measured lifetime for these is ~20 ns resulting in a radiative decay rate of ~0.05 ns^{-1} (this is consistent with lifetime measurements for similar systesm).[12] Since we are interested if the hole can transfer to any of the midgap molecular states, we calculate the total rate for hole transfer as a sum of the individual rates.

The surface of the nanorods was modeled using a six-layer thick slab of $(10\bar{1}0)$-oriented wurtzite CdS terminated with pseudohydrogen. This surface is both the lowest energy surface termination of CdS[13] and CdSe[14] as well as a dominant facet for wurtzite nanorods. The chosen slab has minimal quantum confinement effects and a band gap of 2.53 eV. Relative to the vacuum level, the valence band is -6.47 eV, while the conduction bands is -3.94 eV. For calculations including the absorption of DTC-complexes to the surface, a 3×2 supercell of the 45°-rotated primitive surface cell was utilized resulting in a density of 0.34 molecules per nm^2. Such a density was chosen in order to isolate the interaction between neighboring images of the molecule in order to focus on understanding how the molecule interacts with the CdS. We model surface attachment with a chelating geometry at the cadmium site by the dithiocarbamate group consistent with the prior studies.[15, 16]

As a benchmark to our calculation, we use the deprotonated forms of DTCBipy and DTCBipyFe(acac)$_2$ to compute the optical absorption and compare them with the experimental results. The calculated optical absorption of surface-free DTCBipy (Figure S2B) shows two primary features at 275 nm (4.51 eV) and 345 nm (3.59 eV) with a smaller feature around 530 nm (2.34 eV). Compared to the experimental absorption shown in Figure S4A, we see that there is a systematic blueshift of the primary peaks due to a slight overestimation of the HOMO-n/LUMO+m gap. In the experimental figure, the first primary peak is cutoff as this peak merges with the solvent peak and becomes difficult to interpret. The smaller intensity feature may be related to the signal at the limit of detection around 600 nm in Figure S4A. In both Fe(acac)$_3$ and Fe(bipy)$_3$, the iron is octahedrally coordinated and can be stabilized as either Fe^{3+} or Fe^{2+} where both oxidation states have both low-spin and high-spin configurations. Computationally, for DTCBipyFe(acac)$_2$ with Fe^{3+} the energetically preferred spin-state is the high-spin (μ=5) state and for Fe^{2+}, the energetically preferred state is the low-spin (μ=0). This result combined with the NMR data for DTCBipyFe(acac)$_2$ (Figure S5) suggests that our system contains Fe^{2+}. Furthermore, the optical absorption spectra calculated using Fe^{2+} provides a qualitative match to the experimental absorption spectra (see Figs. S2A and S2B); whereas the spectra calculated using Fe^{3+} contains an extra feature around 750 nm with no corresponding feature in experimental spectra (see Figure S4C).

A.3. Additional TRPL Procedures

Time-resolved photoluminescence measurements were performed using a home built confocal microscope. Dilute solutions of QDs in toluene were excited at low fluence with a 400 nm pulsed laser at 250 kHz repetition rate. The fluorescence from the QD solution was collected by a single photon avalanche diode. Lifetime data were acquired in the form of photon arrival events using a time-correlated single photon counting system (Picoharp 300) with a time bin of 128 ps. Decays were fit to bi- or tri-exponentials of the form: $y = y_0 + \sum_{i=1}^{n} A_i \exp(\frac{-(x-x_0)}{\tau_i})$, where n = 2, 3. Average lifetimes were calculated using the lifetime and amplitude coefficients: $\tau_{avg} = \sum_i^n \frac{A_i \tau_i}{\sum_i A_i}$.

A.4. Calculated absorption spectrum for slab calculations

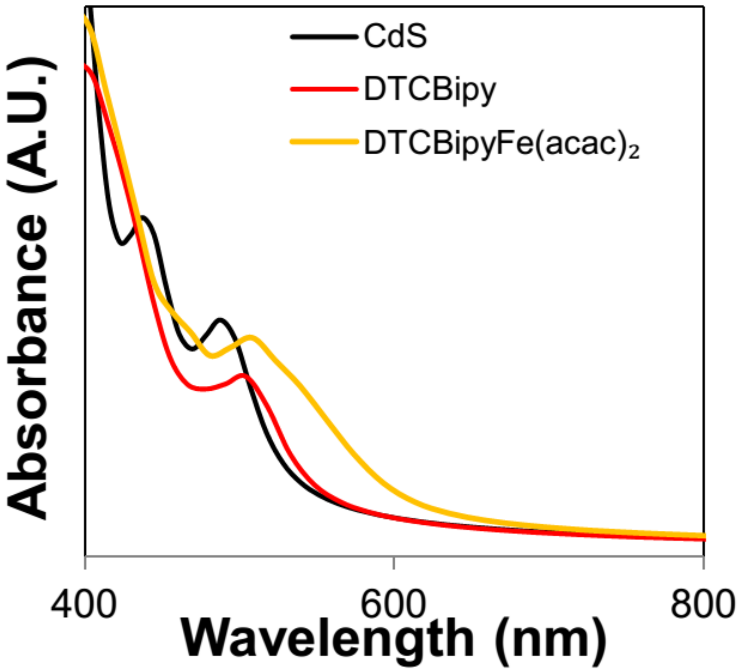

Figure A. 1. Calculated absorption spectrum for the CdS surface ; bare (black), the surface with DTCBipy (red), and the surface with DTCBipyFe(acac)$_2$ shows the redshift of the band edge as well as the introduction of discernable intramolecular excitations. This complements Figure 2. of the main text.

A.5. Orbital Charge Density Plots

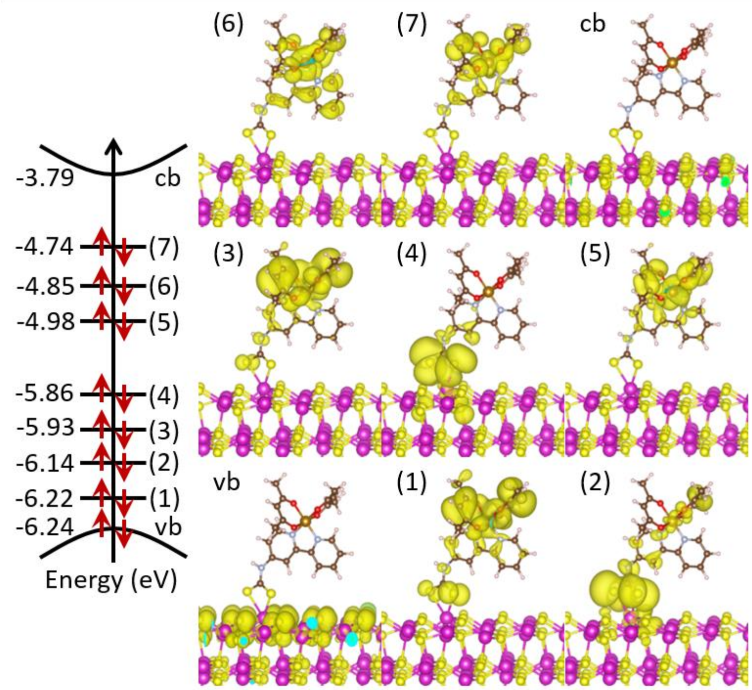

Figure A.2. Orbital charge density plots ; Orbital charge density plots for DTCBipyFe(acac)$_2$ on CdS showing all seven mid-gap as well as the valence and conduction band (extension of Figure 4 from the main text).

A.6. Theoretical absorbance spectra of DTCBipy and DTCBipy-Fe complexes

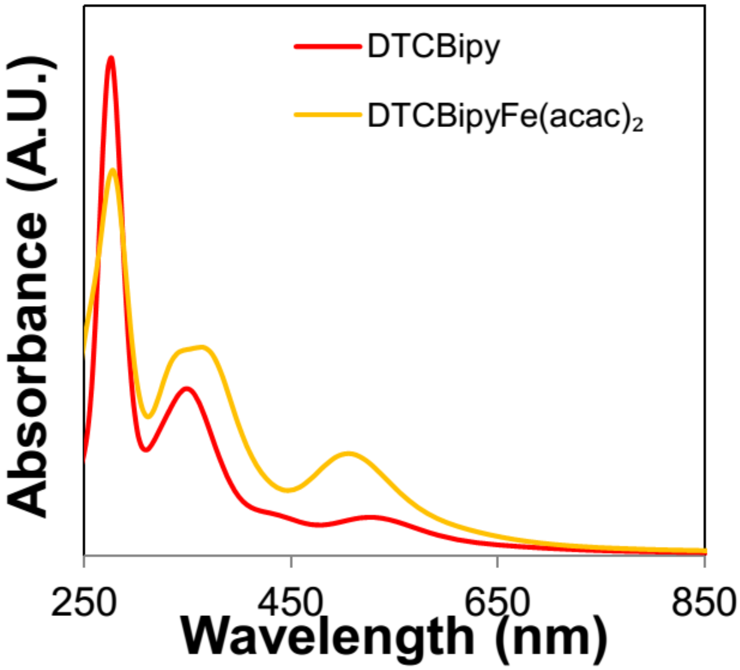

Figure A.3. DTCBipy and DTCBipyFe$(acac)_2$ theoretical absorbance.

A.7. Theoretical absorbance of DTCBipyFe(acac)2 (Fe2+) and DTCBipyFe(acac)2 (Fe3+)

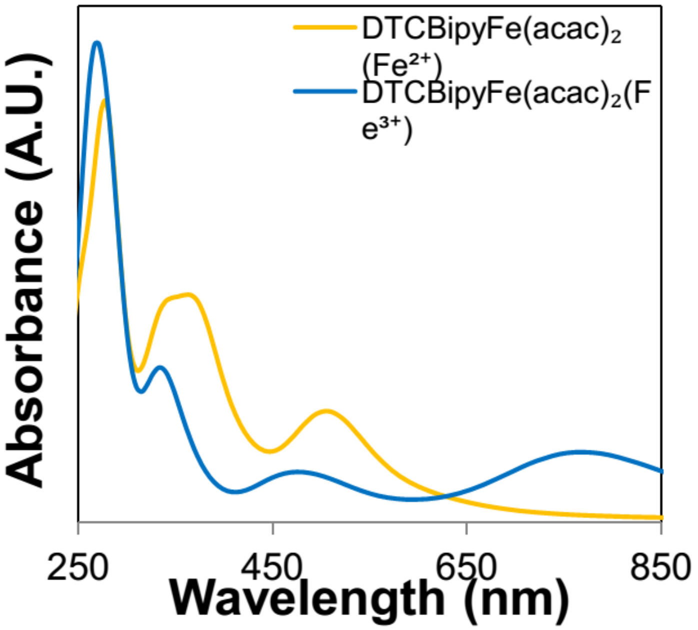

Figure A. 4.Theoretical absorbance of DTCBipyFe(acac)$_2$ (Fe^{2+}) and DTCBipyFe(acac)$_2$ (Fe$^{3+)}$

A.8. ^{1}H NMR of DTCBipyFe complex

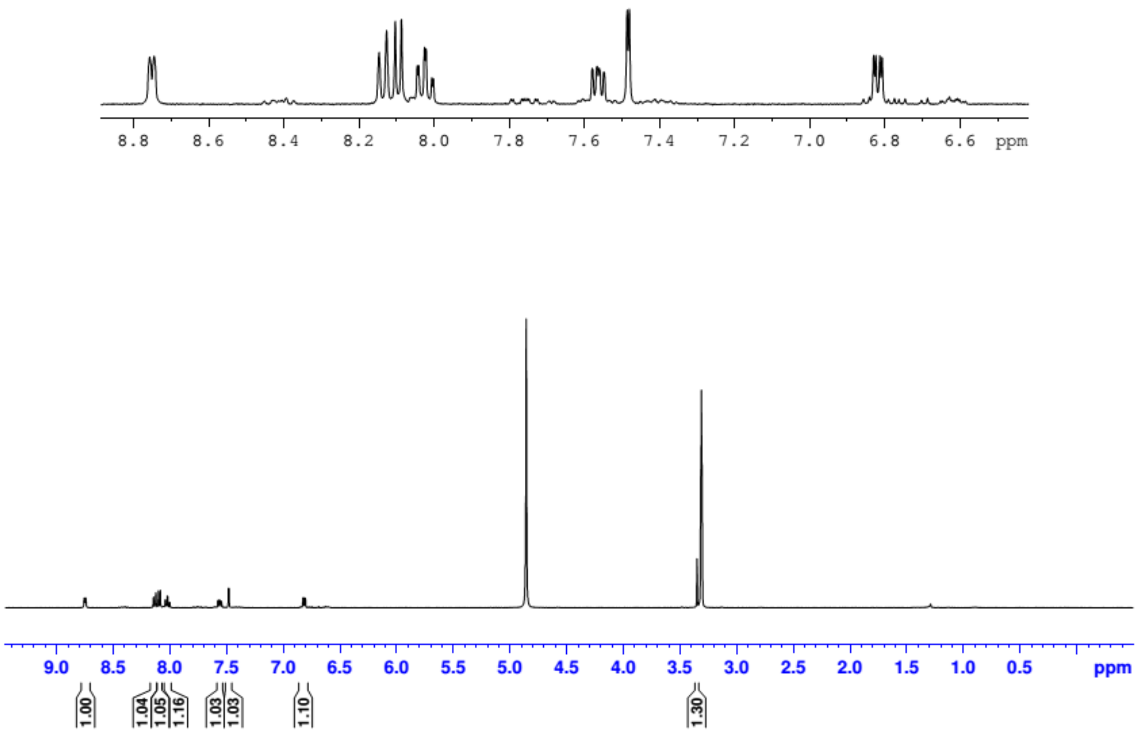

Figure A. 5.^{1}H NMR of DTCBipy-Fe complex

A.9. Wide-field STEM-EDS map

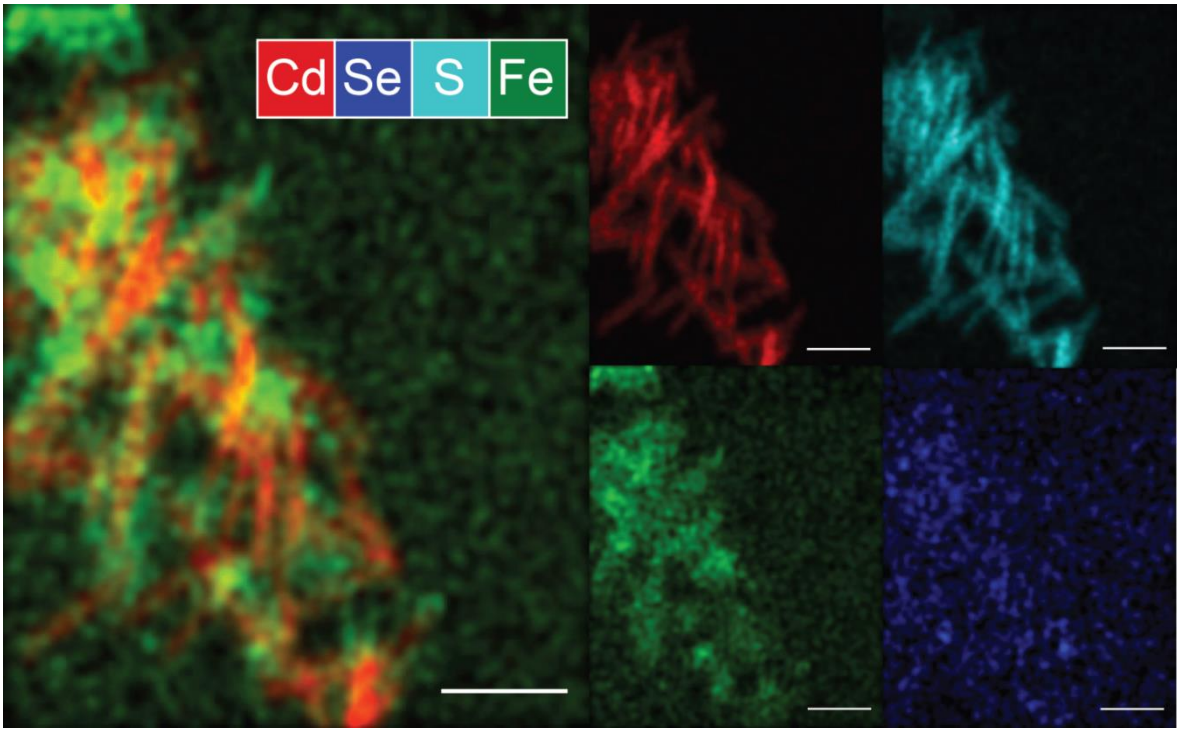

Figure A.6. Wide field STEM-EDS Map ; An image showing a group of CdSe/CdS NRs after ligand exchange with DTCBipy, treatment with Fe(acac)$_3$, and cleaning. Red is Cd, green is Fe, turquoise is S, and blue is Se. S and Se are omitted from the overall picture for clarity. The scale bar is 40 nm.

A.10. STEM-EDS Map of Fe control

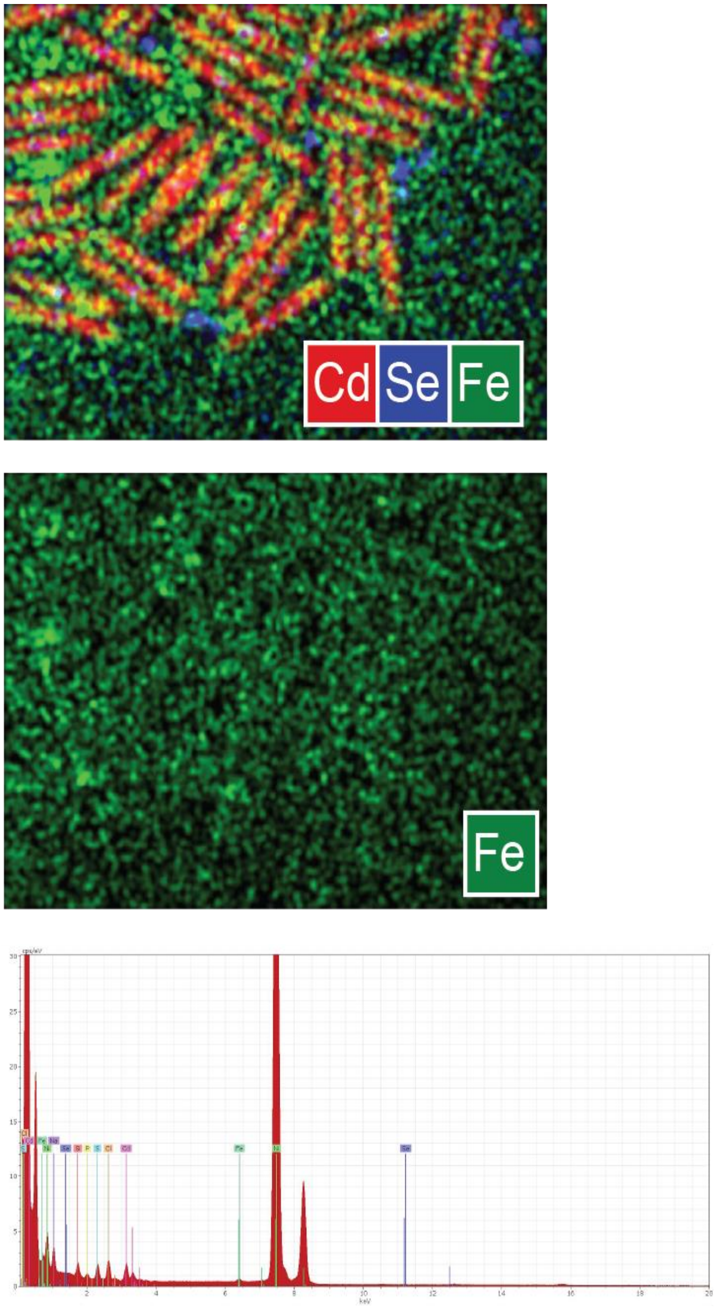

Figure A. 7.STEM-EDS Map of Fe control ; native ligand capped CdSe/CdS rods after being stirred for 16 hours, then precipitated twice as in the DTCBipy ligand capped CdSe/CdS procedure.

A.11. UVVis and Fluorescene Spectroscopy of Fe Control

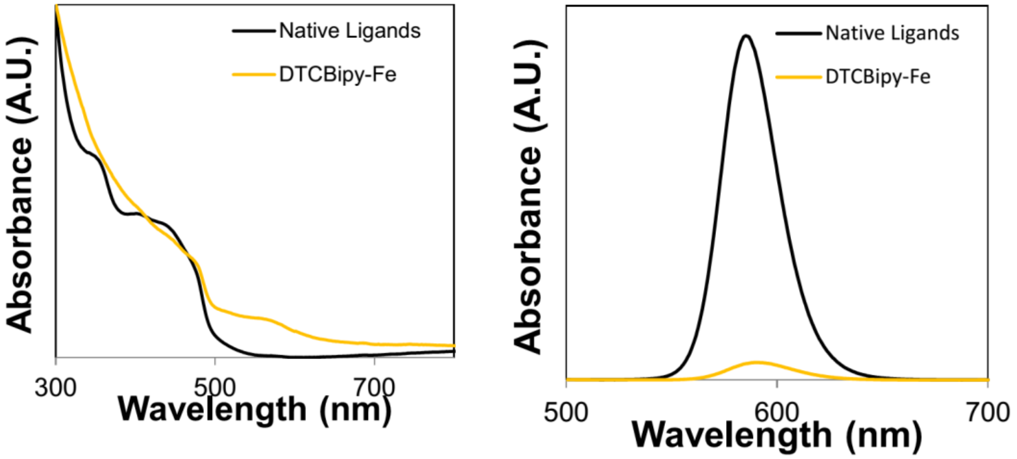

Figure A.8. UVVis and Fluorescene Spectroscopy of Fe Control ; UVVis and fluorescence spectrum of CdSe/CdS rods (native ligands) and Fe(acac)$_3$ stirred overnight (black, QY 2.2%) and CdSe/CdS rods (DTCBipy LE) and Fe(acac)$_3$ stirred overnight (yellow, QY 0.16%).

A.12. Varying wavelength excitation experiments

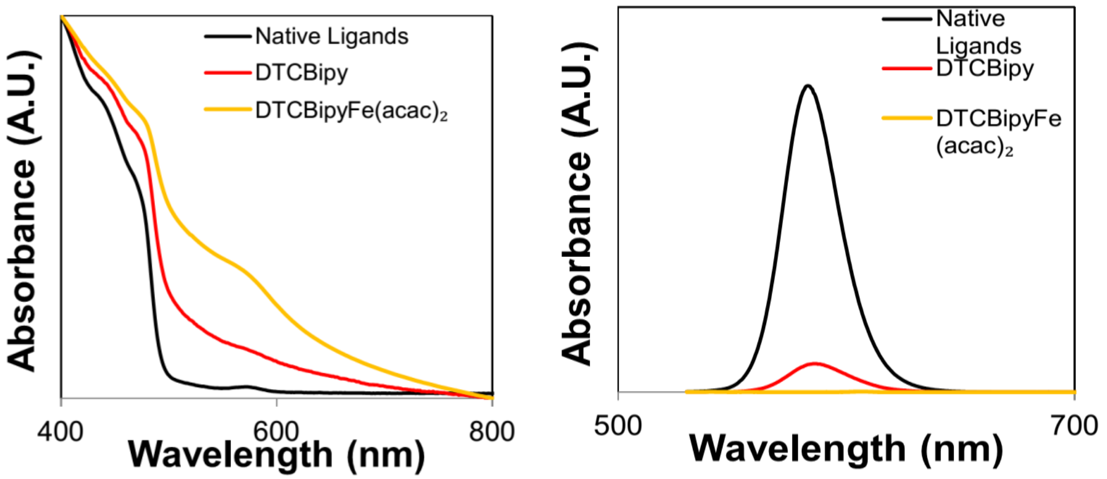

Figure A.9. Varying wavelength excitation experiments ; (Left) Absorbance spectra of CdSe/CdS rods in excitation experiments performed at 514 nm. 514 nm was chosen as a suitable wavelength as it lay in between the CdS and CdSe absorptions, and a known laser standard (Rhodamine B) is suitable for this wavelength. (Right) Excitation experiments performed at 514 nm: Native ligands (black, QY 5.4%), DTCBipy exchanged rods (red, QY 0.3%), and DTCBipyFe exchanged rods (yellow, QY 0.001%). These quenches were expected as ligand exchange can cause the formation of trap states,[17] even in systems which have a passivated core[18]. Further, the mid-gap states presented from DTCBipy could also be serving to quench fluorescence. Secondly, there is no region between the onset of the CdS bandgap and CdSe absorption that would completely negate CdS absorption, so effects of the CdS quenching are always present to a degree.

A.13. Bi-exponential fit of CdSe/CdS NRs capped with native ligands.

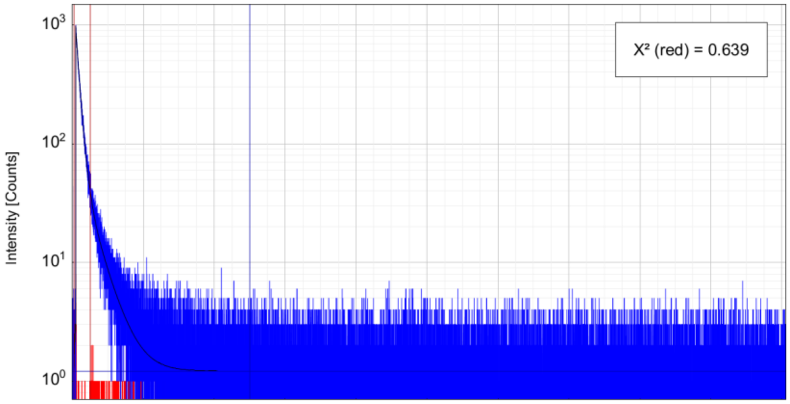

Fractional Amplitudes of the Positive Decay Components:

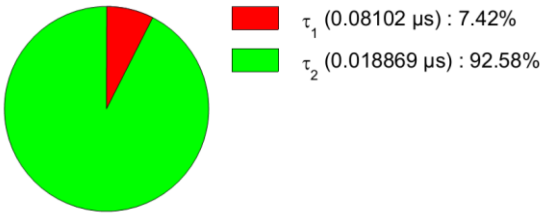

Figure A.10. Bi-exponential fit of CdSe/CdS NRs capped with native ligands.

A.14. Bi-exponential fit of CdSe/CdS NRs capped with native ligands.

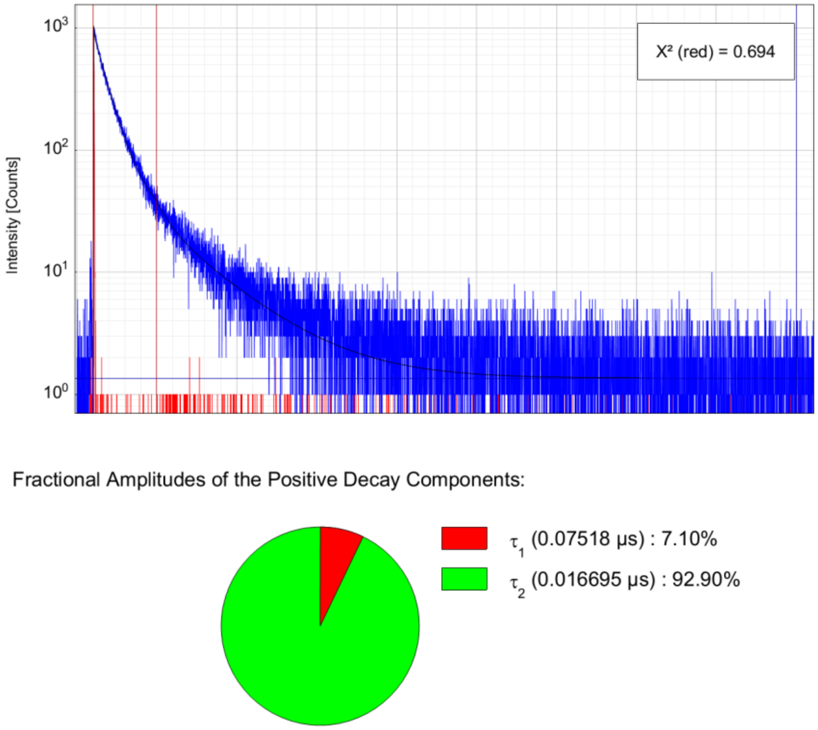

Figure A.11. Bi-exponential fit of CdSe/CdS NRs capped with native ligands.

A.15. Tri-exponential fit of CdSe/CdS NRs capped with DTCBipyFe

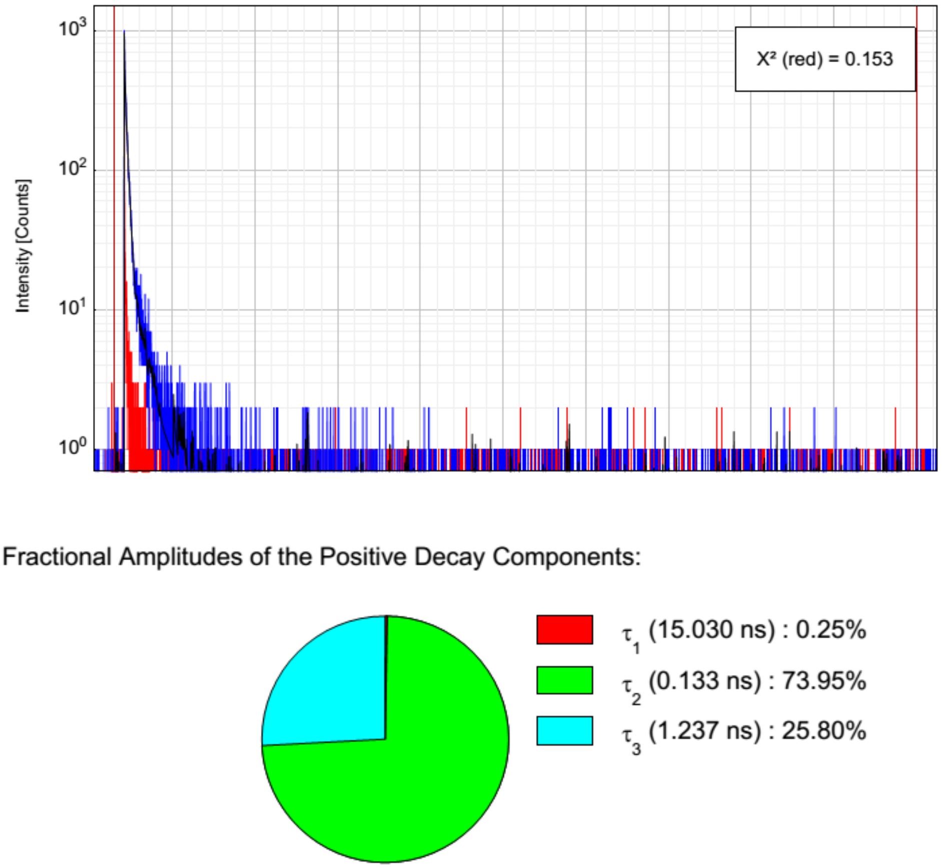

Figure A.12. Tri-exponential fit of CdSe/CdS NRs capped with DTCBipyFe

A.16. DTCBipy Decomposition UVVis and Fluorescence

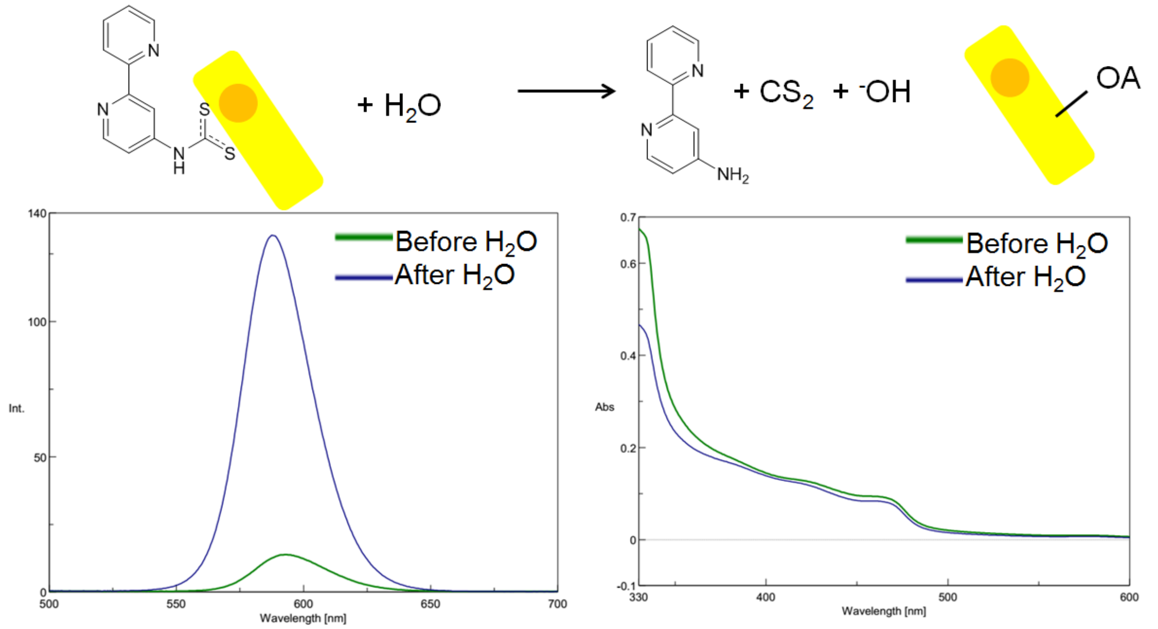

Figure A.13. Solutions of pyridine and DTCBipy exchanged CdSe/CdS before and after addition of the appropriate amount of water to bring the mol fraction of H_2O to χ=0.2.

B. Additional Synthetic Procedures for Chapter 3

B.1. Experimental Detail

Materials: Dichloromethane (DCM) (anhydrous, ≥99.8%), ethanedithiol (≥98.0%), trimethylamine (≥99.5%), ethyl acetate (EtOAc) (99.9%), hexanes (99.9%), $NaHCO_3$ (ACS grade), and $MgSO_4$ (anhydrous, 97%) were purchased from Sigma-Aldrich. 9-Fluorenylmethyl chloroformate (Fmoc-Cl) (98%) was purchased from Oakwood Chemical. All materials were used as purchased without further purification.

FMT ligand synthesis

To a 100-ml round bottom flask with stir bar was added dry DCM, Fmoc-Cl (2.5 g, 10 mmol),and ethanedithiol (3.35 ml, 40 mmol). The reaction flask was sealed and maintained under inert atmosphere. Triethylamine (1.4 ml, 10 mmol) was added dropwise via syringe. The reaction was monitored via TLC (20% EtOAc / 80% Hexanes). Reactions typically completed within 15 min. The crude product was then washed 2 times with 5% $NaHCO_3$, followed by one brine wash. The organic layer was then dried over $MgSO_4$, solvent removed under reduced pressure. The resulting crude product was purified via column chromatography using a solvent gradient from 2.5% EtOAc/hexanes to 10% EtOAc/hexanes to yield a thick yellow oil. Yield: 1.74g (55%) ^{1}H NMR (400MHz, $CDCl_3$) δ 7.79 (d, 2H, J=7.6 Hz), 7.60 (d, 2H. J=7.1 Hz), 7.43 (t, 2 H, J=7.4Hz), 7.34 (td, 2H, J=7.5, 1.1 Hz), 4.52 (d, 2H, J=7.4 Hz), 4.28 (t, 1H, J=7.3 Hz), 3.08 (t, 2H, J=6.7 Hz, 2.76 (m, 2H), 1.65 (t, 1H, J=8.6 Hz). ^{13}C NMR (100 MHz, $CDCl_3$) δ 170.4 (C=O), 143.2, 141.3, 127.9, 127.2, 125.1, 120.1 (ArC), 69.2 (-CH-), 46.7(-CH_2-), 35.0(-CH_2-), 24.8(-CH_2-) ppm.

OA-QD synthesis

The synthetic procedure for fabricating oleic acid capped PbS QDs are described in detail by Hines and Scholes.[147]

FMT-in synthesis exchange

To a solution of PbS QDs in $CHCl_3$ under vigorous stirring was added a solution of FMT in $CHCl_3$. After 30 min, the particles were precipitated with acetone three times, and the removal of the native OA ligands was verified via ^{1}H NMR spectroscopy, notably the loss of the vinylic protons.

To prepare FMT-PbS QDs for device fabrication, the FMT ligand (0.1 g, 0.316 mmol) was first dissolved in 1 mL of toluene. In another round bottom flask, PbO (0.3 g, 1.3 mmol) and oleic acid (1.5 mL, 4.7 mmol) was dissolved in 18 mL of octadecene and degassed at 100°C under vacuum overnight to form Pb-oleate. In a separate flask, bis(trimethylsilyl) sulfide (TMS) (0.29 mL, 1.37 mmol) was dissolved in 13 mL of degassed octadecene. The Pb-oleate solution was heated to 63°C, and then the TMS solution was injected rapidly to enable nucleation of the PbS-QDs. After the initial synthesis of the oleic acid capped PbS QDs, the FMT solution was injected into the flask at 60°C during the cooling stage of the reaction. The reaction was further cooled to 30°C, and acetone was injected into the flask to precipitate the QDs. The FMT-QDs were centrifuged at 7800 rpm for 5 minutes, and the precipitate was redispersed in toluene. These FMT-QDs were precipitated again with acetone, and dried under vacuum for 20 minutes. The FMT-QDs were then dissolved in anhydrous octane at 50 mgmL^{-1}.

Full device preparation

Two layers of ZnO nanoparticles are spin coated onto an ITO substrate at 3000 rpm for 30 s. The synthesis of these ZnO nanoparticles are discussed elsewhere.[125] Then a 315mg/mL of a $PbI_{0.8}Br_{0.2}$-PbS active layer was spin coated onto the top of the ZnO nanoparticles .The synthesis and ligand exchange method for these $PbI_{0.8}Br_{0.2}$-PbS QDs are discussed elsewhere.[134] Then two layers of EDT-PbS were spin coated onto the active layer. The methods are discussed below:

Direct soak EDT-PbS QDs

The preparation of the EDT-PbS QD exchange was performed as described in a previous study.[134] To prepare one layer of EDT-PbS QDs, a 50mg/mL solution OA-QDs were spin coated at 2500 rpm for 10 s onto the top of a PbS-active layer. The OA-QD layer was then soaked in a 0.01% v/v solution of 1,2-ethanedithiol (EDT) in acetonitrile for 30 s. The solution was then spin coated off at 2500 rpm, and washed three times with acetonitrile. These steps were repeated twice to yield 2 layers of EDT-PbS.

FMT-cleaved EDT-PbS QDs

The FMT-QDs initially dispersed in toluene were precipitated with the addition of acetone. The QDs were further dried and dispersed in octane at a concentration of 50 mgmL^{-1} The FMT-QDs were spin coated on top of a PbS-active layer at a spin speed of 2500 rpm for 10 s. The FMT-QD layer is then treated with mild base solution noted below in ethyl acetate for 30 s. The device was then spun at 2500 rpm for 10 s to remove the residual solvent. The film was washed 3 additional times with ethyl acetate.

FMT mild base preparation

Mixtures of bases were prepared at a 1% v/v solution in ethyl acetate. For example, a 9:3 mixture of DTP:DBU is as follows: 100 μL of DTP is diluted in 10 mL of ethyl acetate. In a separate vial, 100 μL of DBU is dissolved in 10 mL of ethyl acetate. Then 900 μL of the 1% DTP solution is mixed with 300 μL of the 1% DBU solution yield a 9:3 DTP: DBU mixture.

For the 30:1 DMPpy:DBU mixture, 100 μL of DMPpy is diluted in 10 mL of Ethyl Acetate. In a separate vial, 100 μL of DBU is dissolved in 10 mL of ethyl acetate. Then 900 μL of the 1% DMPpy solution is mixed with 30 μL of the 1% DBU solution to yield a 30:1 DMPpy: DBU mixture.

Absorbance characterization

Film Absorbance measurements were performed by a Lambda 950 500 UV-Vis-IR spectrometer.

Fourier transform infrared (FTIR) spectroscopy measurements

Attenuated total reflectance (ATR) FTIR measurements were performed on a Thermo Nicolet is50.

UPS Measurements

A thin layer of colloidal QDs were spin-coated at 2500 rpm onto an Au substrate before UPS testing. The ultraviolet photo-electron spectra were obtained using the 21.22 eV He I lines from the discharge lamp. The band gaps for both the EDT-PbS film and cFMT-PbS film were determined by the optical absorption spectrum by taking the value from their first excitonic peaks. The Fermi level for each film were taken from the intersection from the slope of the low binding energy section and its baseline, and subtracted from the He I line. The value of the valence band maximum was determined by adding the Fermi level and the value from the intersection from the slope of the high binding energy section and its baseline. The value of the conduction band minimum was determined by adding the value of the valence band maximum and the optical band gap.

XPS characterization

A layer of colloidal QDs were spin-coated at 2500 rpm onto a glass substrate before XPS measurements. The film was then mounted onto a stainless steel mounting plate. XPS measurements were performed on a Thermo Scientific K-Alpha system. The source used was an Al Kα source. The takeoff angle was 90°. In order to account for charging, XPS spectra were calibrated to the samples' respective C 1s peak at 284.8 eV.

AM1.5 Measurements

AM1.5 current voltage (*J*-*V*) sweeps were collected using a Keithley 2400 sourcemeter unit under simulated AM1.5G illumination (Sciencetech class A). The AM1.5 was calibrated using a reference solar cell (Newport). The devices were measured under a continuous flow of nitrogen gas. The aperture was 4.9 mm^2 for a device.

External Quantum Efficiency (EQE) measurements

EQE measurements are performed with an Oriel Instruments Quantum Efficiency measurement system.

DFT Calculations

All DFT calculations were performed using Gaussian 09. B3LYP was used as the functional and all molecules were optimized to a basis set of 6-311g**.

B.2. FMT ^{1}H NMR

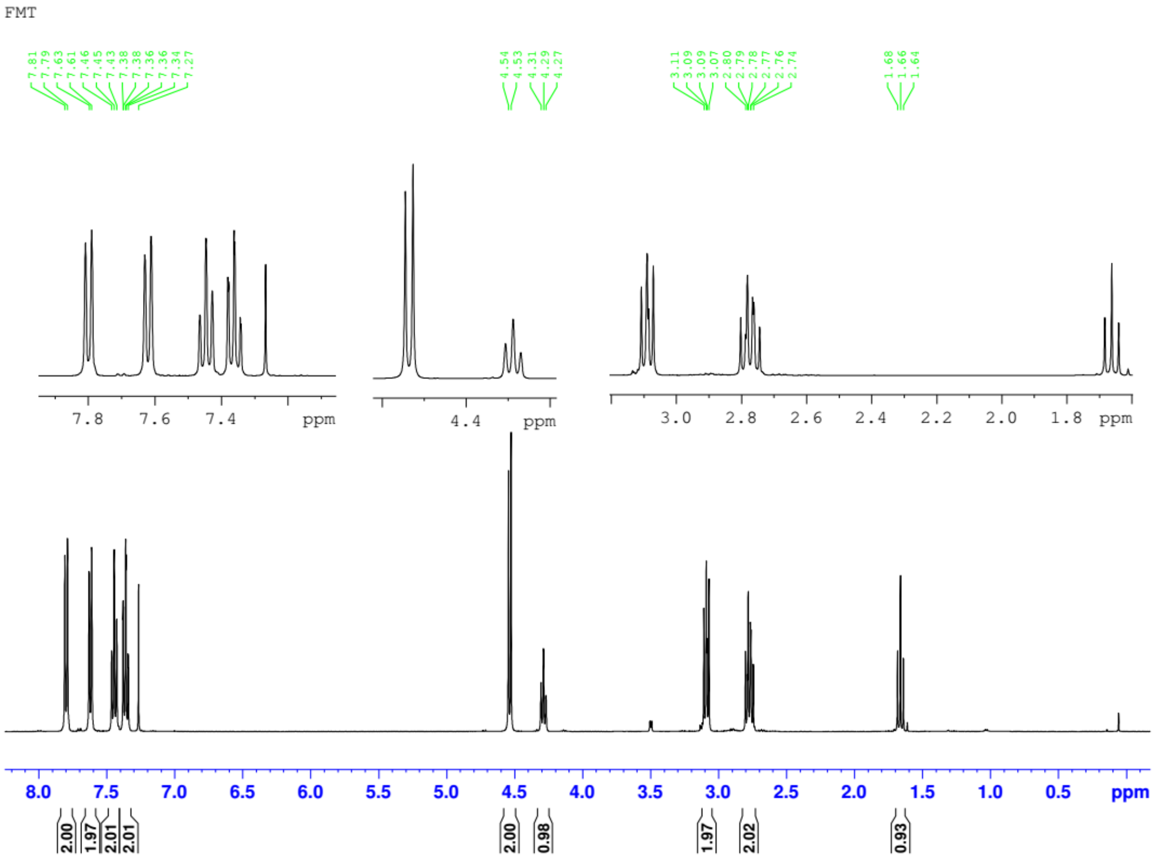

Figure B.1. ^{1}H NMR of Pure FMT.

B.3. FMT ^{13}C NMR

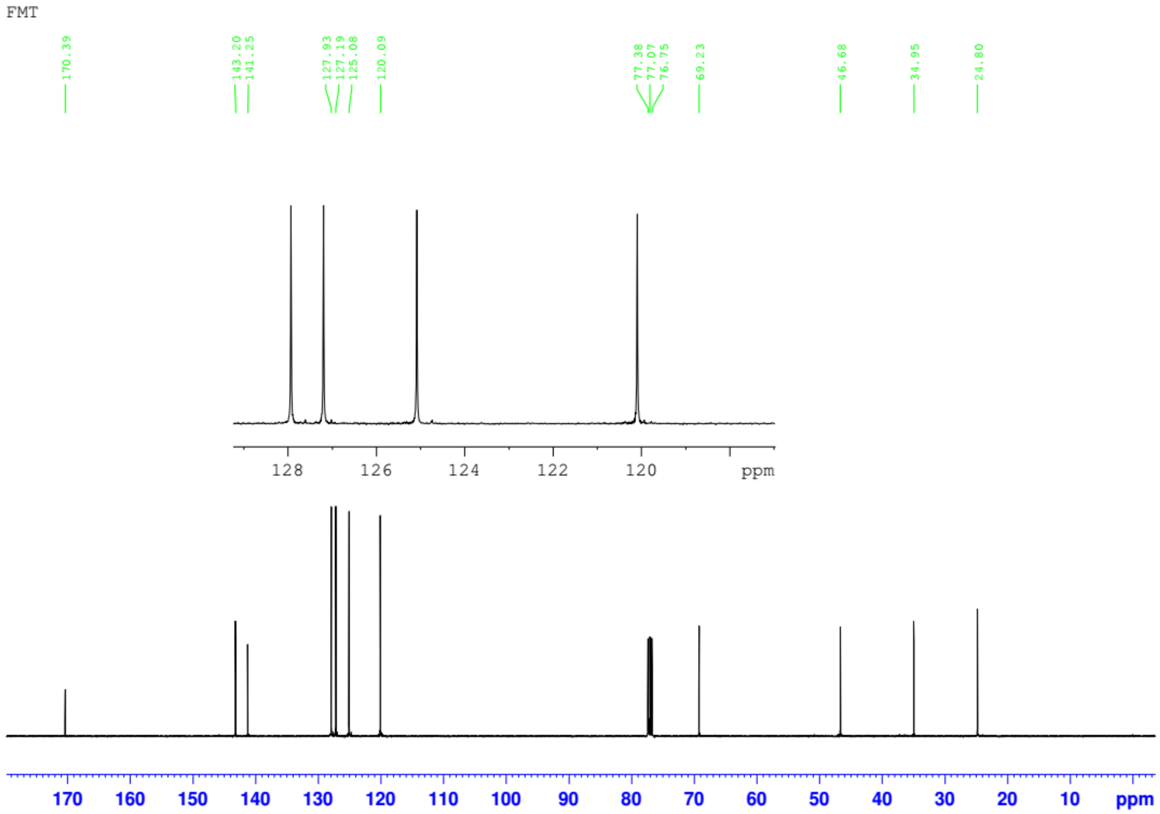

Figure B.2. ^{13}C NMR of Pure FMT.

B.4. ^{1}H NMR of OA-PbS

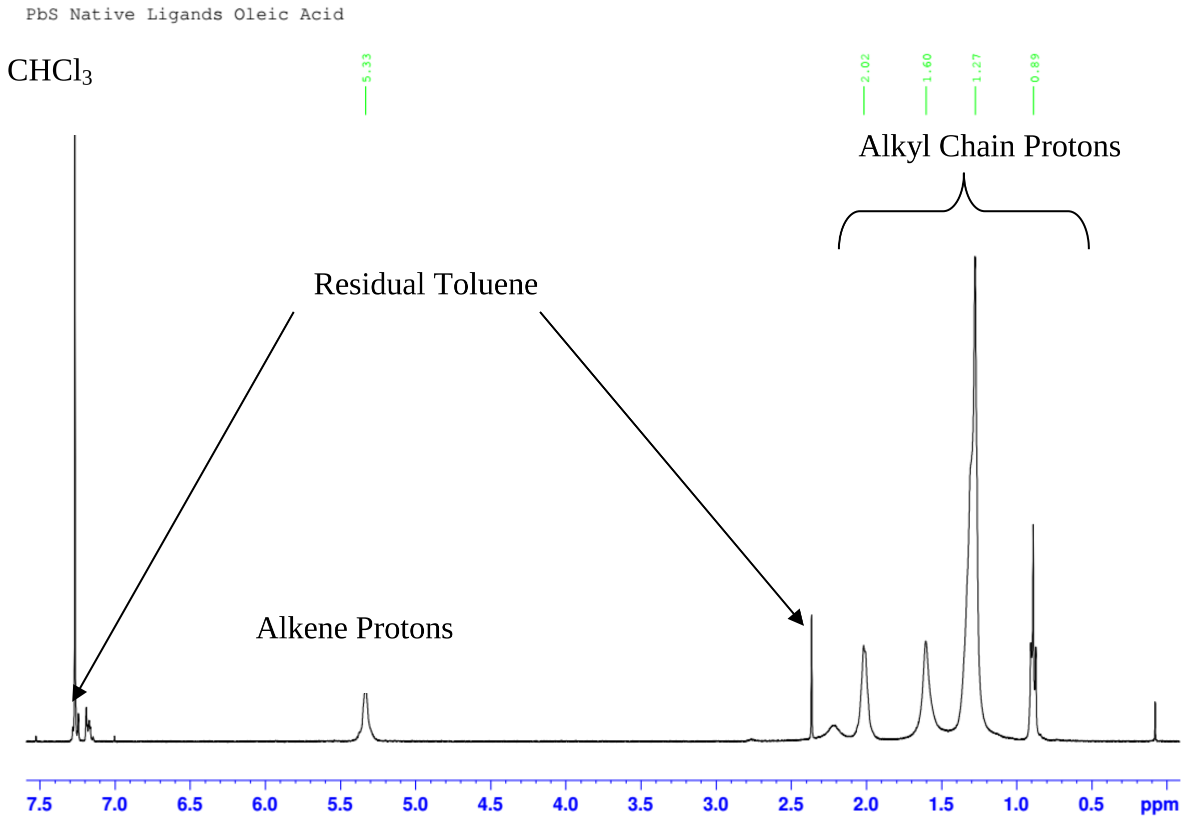

Figure B.3. ^{1}H NMR of OA-PbS. Pertinent signals are marked.

B.5. ^{1}H NMR of FMT-PbS

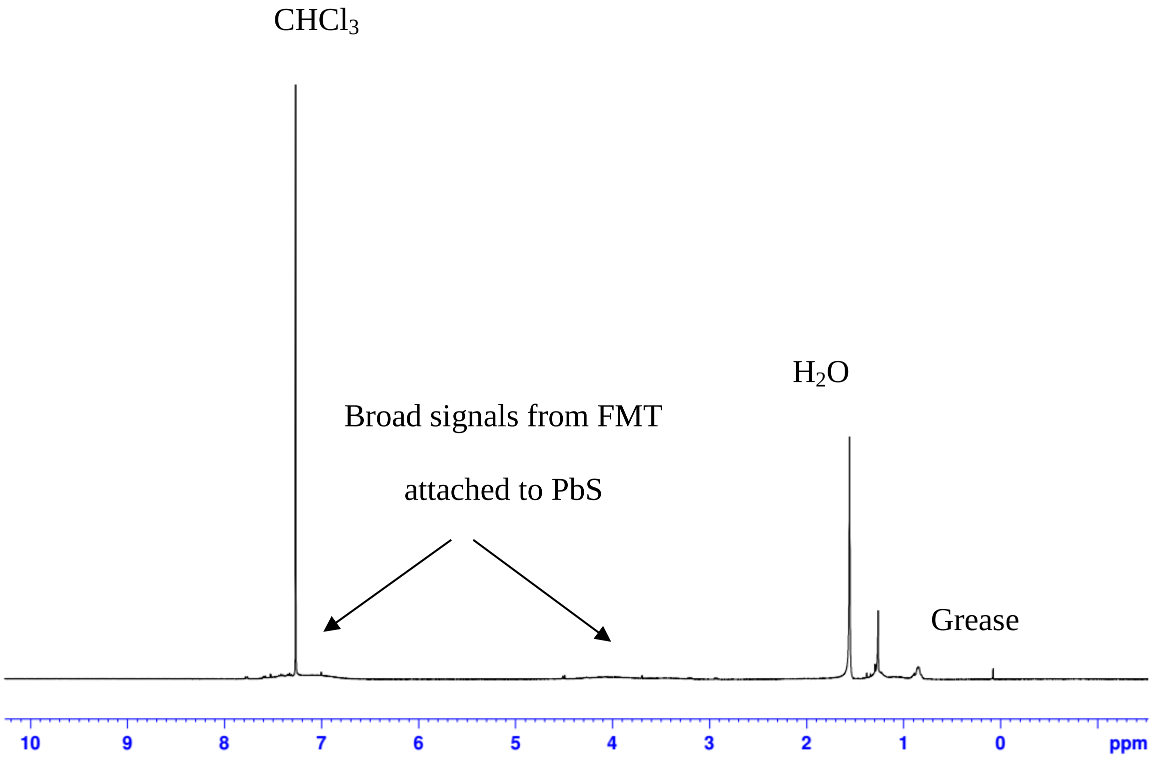

Figure B.4. ^{1}H NMR of FMT-PbS. Pertinent peaks are marked.

B.6. XPS Data

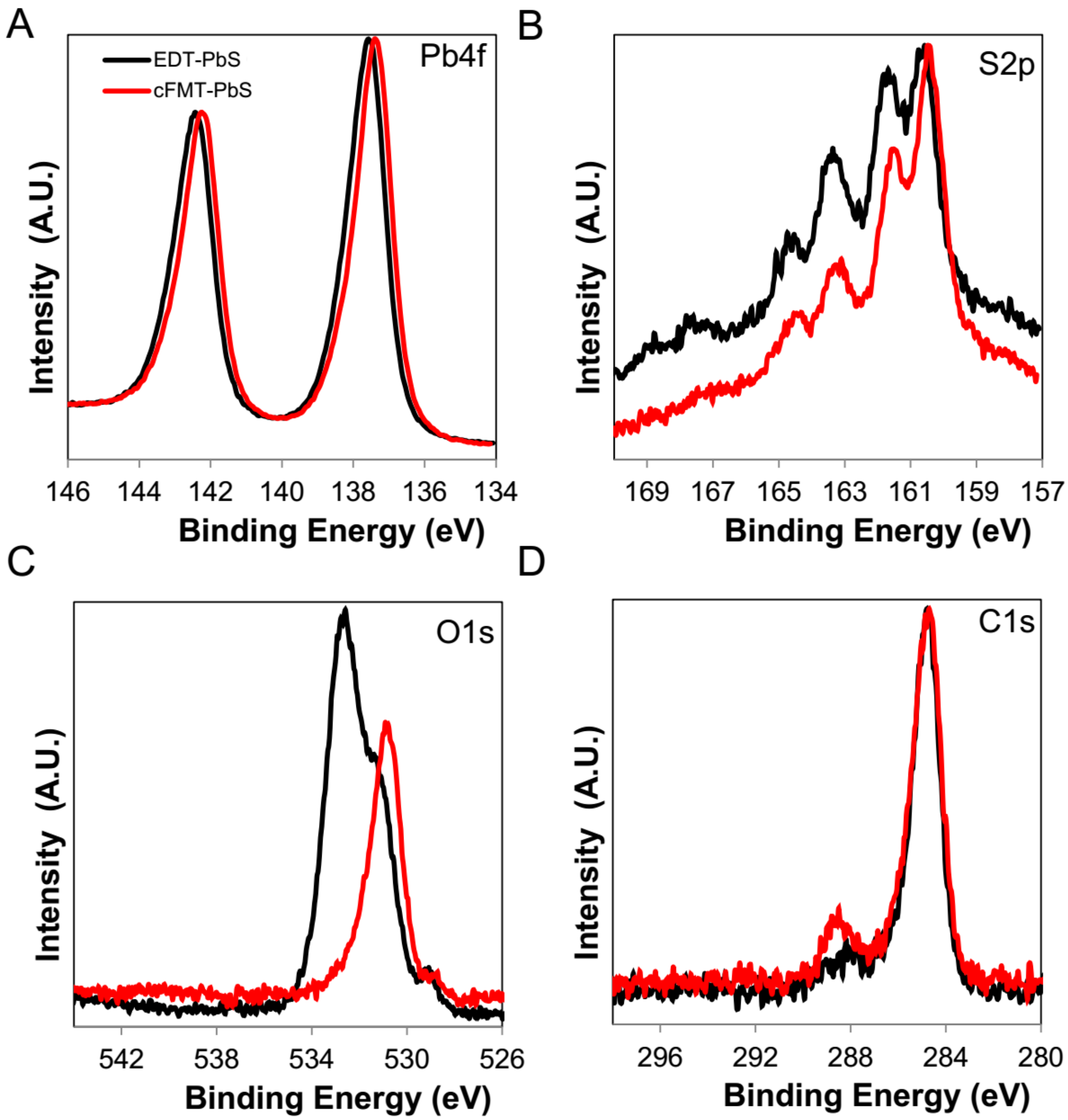

Figure B.5. XPS spectra comparing a FMT- cleaved Film to an direct soak EDT-PbS Film. XPS spectra are shown for a) Pb 4f, b) S 2p, c)O 1s, d) C 1s. The C1s spectra for FMT contains a small signal at 289 eV which is likely due to residual ethyl acetate from the cleavage procedure.

B.7. UPS Data

UPS-EDT-PbS

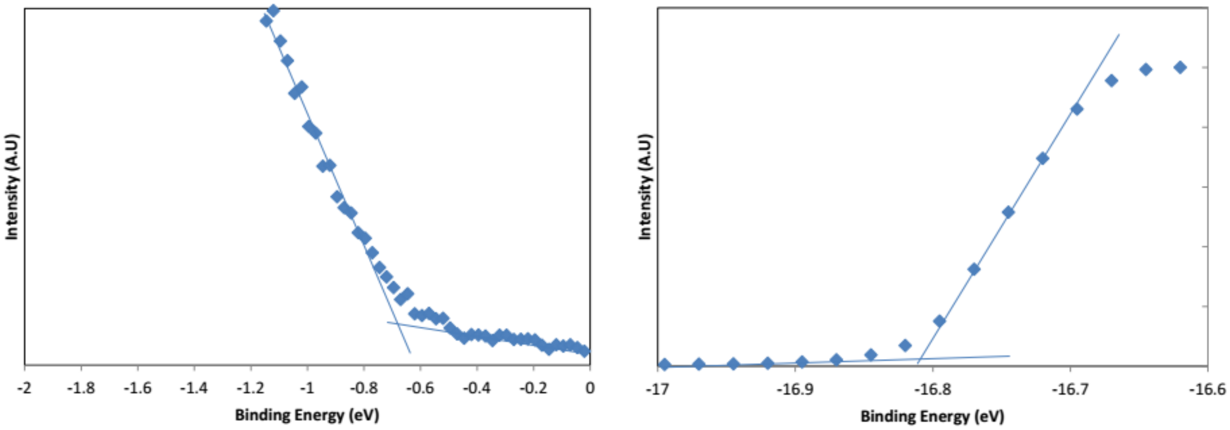

UPS-cFMT-PbS

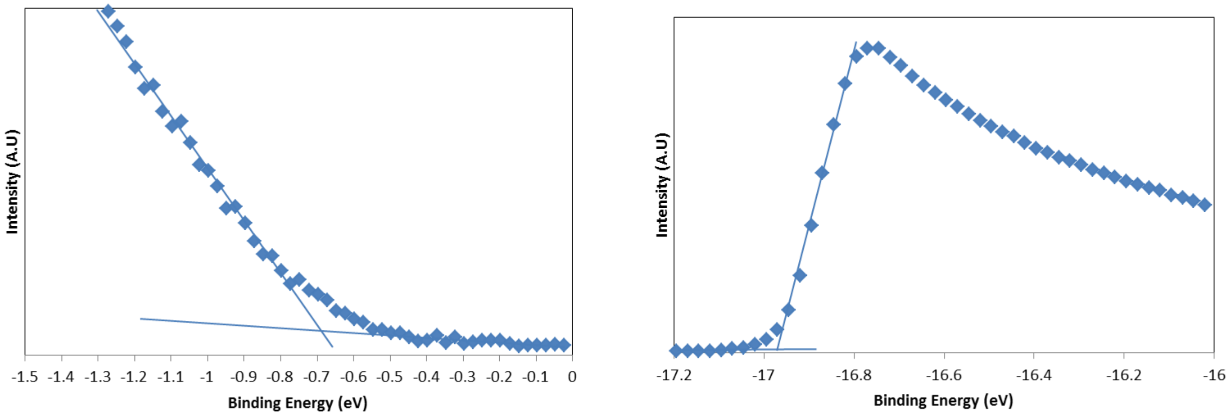

Figure B.6. Ultraviolet Photoelectron Spectra comparing a directly soaked EDT film and a FMT-Cleaved EDT-PbS Film. A) Zoom in spectra of the high binding energies for a directly soaked EDT film. B) Zoom in spectra of the low binding energies for a directly soaked EDT film. C) Zoom in spectra of the high binding energies for a FMT cleaved EDT-PbS Film. D) Zoom in Spectra of the low binding energies for a FMT cleaved EDT-PbS film.

B.8. JV Sweeps

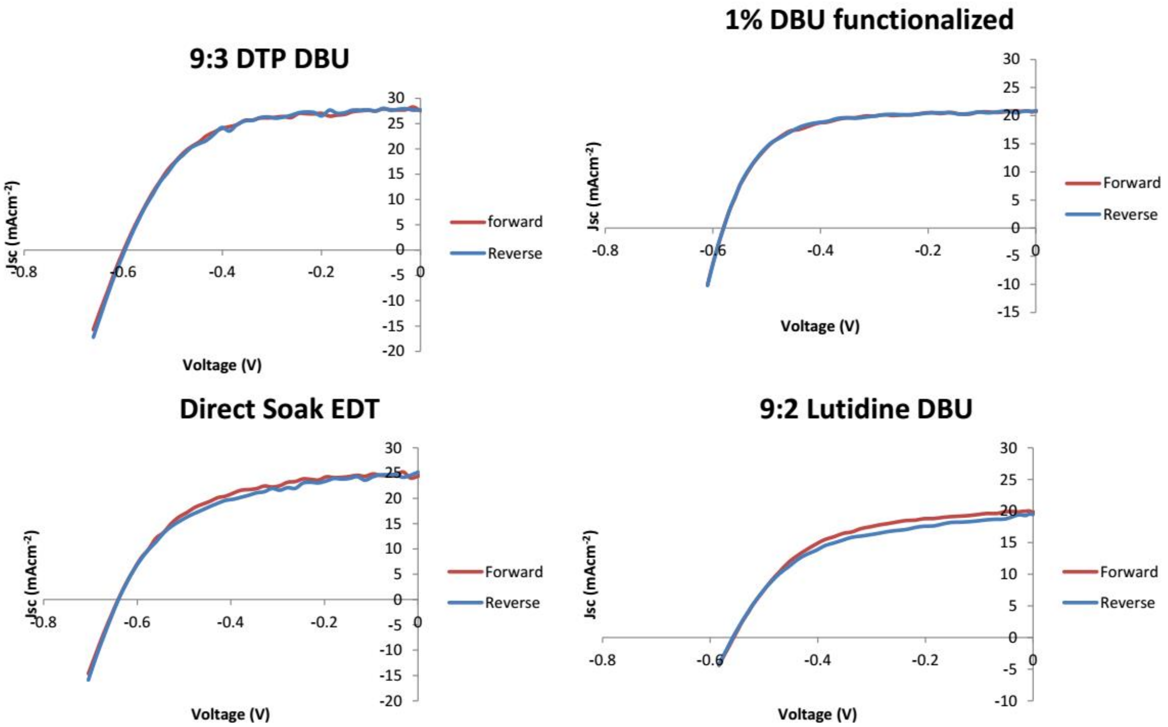

Figure B.7 Full device characteristics for those tabulated in Table 1.

B.9. DFT Data

Molecule	HOMO (eV)	LUMO(eV)	Bandgap (eV)
EDT	-6.73	-0.17	6.56
FMT	-6.22	-1.31	4.92

Figure B.8. HOMO, LUMO, and bandgap of EDT and FMT calculated from DFT.

C. Additional Synthetic Procedures for Chapter 4

C.1. General synthetic procedure for alkyl thiocarbonates

To an argon flushed 50 ml round bottom flask was added dry DCM (15 ml), pyridine (5 ml), and ethanedithiol (6.14 ml, 73.2 mmol). Alkyl chloroformate (24.4 mmol) was added slowly at a rate of 0.5 ml/hr via syringe pump. After addition was complete the reaction was allowed to stir for 6 hours at which point a white precipitate had formed. The reaction mixture was washed 2x with 10 ml of 5% HCl solution, 1x with 10ml of brine, and dried over $MgSO_4$. Solvent was removed under reduced pressure. The remaining clear colorless oil and white precipitate was purified via vacuum distillation.

O-butyl S-(2-mercaptoethyl) carbonothioate. BP 145 °C@ ~2 torr. Clear, colorless oil, 57.1% yield. ^{1}H NMR (400MHz, $CDCl_3$) δ 4.12 (t, 2H, J=5.4Hz), 3.02 (t, 2H, J=5.1 Hz), 2.73 (q, 2H, J=5.3 Hz), 1.60 (qt, 3H, J=6.6 Hz), 1.35 (sext, 2H, J=6.0 Hz), 0.89 (t, 3H, J=5.9 Hz).

O-hexyl S-(2-mercaptoethyl) carbonothioate. BP 135 °C@ ~2 torr. Clear, colorless oil, 48.2% yield. ^{1}H NMR (400MHz, $CDCl_3$) δ 4.22 (t, 2H, J=7.7 Hz), 3.07 (m, 2H), 2.78 (m, 2H), 1.65 (m, 3H), 1.31 (m, 6H), 0.90 (t, 3H, J=6.8 Hz).

C.2. Synthetic procedure for O-(4,5-dimethoxy-2-nitrobenzyl) S-(2-mercaptoethyl) carbonothioate

To a dry 25 ml round bottom flask was added 4,5-dimethoxy-2-nitrobenzyl chloroformate (276 mg, 1 mmol) the flask was transferred to a dark fume hood and flushed with argon. Dry DCM (7 ml), and ethanedithiol (0.25 ml, 3 mmol) were added. Triethylamine (0.4 ml, 1 mmol) was added dropwise with vigorous stirring. After 30 minutes TLC indicated reaction completion. The reaction mixture was reduced with rotary evaporation and resulting orange/red solid run through a “hypersep” column using a solvent gradient of 10% ethylacetate in hexanes to 30% ethylacetate in hexanes to produce a yellow crystal in 10.4% yield. ^{1}H NMR (400MHz, CDCl3) δ 7.70 (s, 1H), 6.97 (s, 1H), 5.63 (s, 1H), 3.97 (s, 3H), 3.94 (s, 3H), 3.09 (t, 2H, J=5.56 Hz), 2.77 (q, 2H, J=5.8 Hz), 1.63 (t, 1H, J=6.8 Hz).

C.3. Synthetic procedure for 2-((2-nitrobenzyl)thio)ethane-1-thiol

To a dry 100 ml round bottom flask was added DCM (48 ml), EDT (1.36 ml, 16 mmol), and triethylamine (0.56 ml, 4 mmol). 2-nitrobenzyl bromide (0.864 g, 4 mmol) was dissolved in 5 ml of DCM and added dropwise to the reaction solution. After 15 minutes TLC using ceric ammonium molybdate stain indicated reaction completion. The reaction solution was washed twice with 10 ml of deionized H_2O, once with 10 ml of brine, dried over $MgSO_4$, and reduced via rotary evaporation. The oil was purified via column chromatography (10-30% gradient of ethyl acetate in hexanes) to yield a slightly yellow, clear oil in 40.3% yield. ^1H NMR (400MHz, $CDCl_3$) δ 7.97 (dd, 1H, J=8.1, 1.1 Hz), 7.57 (td, 1H, J=7.5, 1.3 Hz), 7.45 (m, 2H), 4.09 (s, 2H), 2.68 (m, 4H), 1.67 (t, 1H, J=7.9 Hz).

C.4. PbS QD Synthesis

PbO (2.1 mmol), OA (7.1 mmol), and ODE (12.7 ml) were added to a 50 ml three-neck round bottom flask with stir bar, septa, condenser, and inlet adapter and allowed to degass at 100 °C for 18 hours overnight. The reaction was flushed with Ar and heated to 125 °C. TMS (0.85 mmol) was mixed with 1 ml of ODE in a nitrogen glovebox. The solution was drawn into a syringe and injected swiftly into the lead oleate solution. The solution immediately changed from clear, colorless to clear, dark brown. After 1 minutes the heating mantle was removed and solution allowed to cool to room temperature. The solution was then centrifuged (15 min, 8k rpm) to remove any insoluble material. 10 ml of ethanol and 10 ml of acetone was then added to the mixture for precipitation via centrifugation (15 min, 8k rpm). The pellet was suspended in toluene and cleaning process repeated two more times.

C.5. Procedure for Ligand Exchange

The absorbance of a suitable concentration of PbS QDs (OD of first exciton peak ~0.9) was measured for calculation of size and concentration and the solution was placed into a 6 dr vial with a stir bar.[241,242] ~5 mg of ligand (considered to be excess) was dissolved in 1 ml $CHCl_3$ and added dropwise to the solution of OA-capped PbS. The solution was allowed to stir for 1 hour. The seeds were then precipitated via addition of acetone and resuspended in $CHCl_3$ at least three times before being observed via ^1H NMR.

C.6. General Procedure for Ligand Degradation

Various ligand degradation attempts all followed the same methodology. The ligand concentration in solution varied depending on which characterization technique was to be used; for instance, in situ UV-Vis absorbance monitoring required a smaller concentration of ligand in comparison to in situ NMR experiments. GC-MS experiments (though no data yielded any viable information) were conducted by removing 50 µl from a UV-Vis experience and diluting with 1 mL of chromatography solvent.

Irradiation on degradation experiments was performed using a 4W lamp set at either 254 nm or 348 nm, or a Xe lamp with a A.R. density of 1.5 calibrated to 1 sun intensity. Removal of the IR filter on the sun lamp caused rapid organic decomposition. Various intervals were used (5 minutes, 15 minutes, 30 minutes, etc.) to take data points during these experiments, but there was no evidence that the expected molecular transformations were occurring during any of these time increments. Typical results from UV-Vis absorbance and NMR spectroscopies are shown below.

C.7. UV Degradation of NET

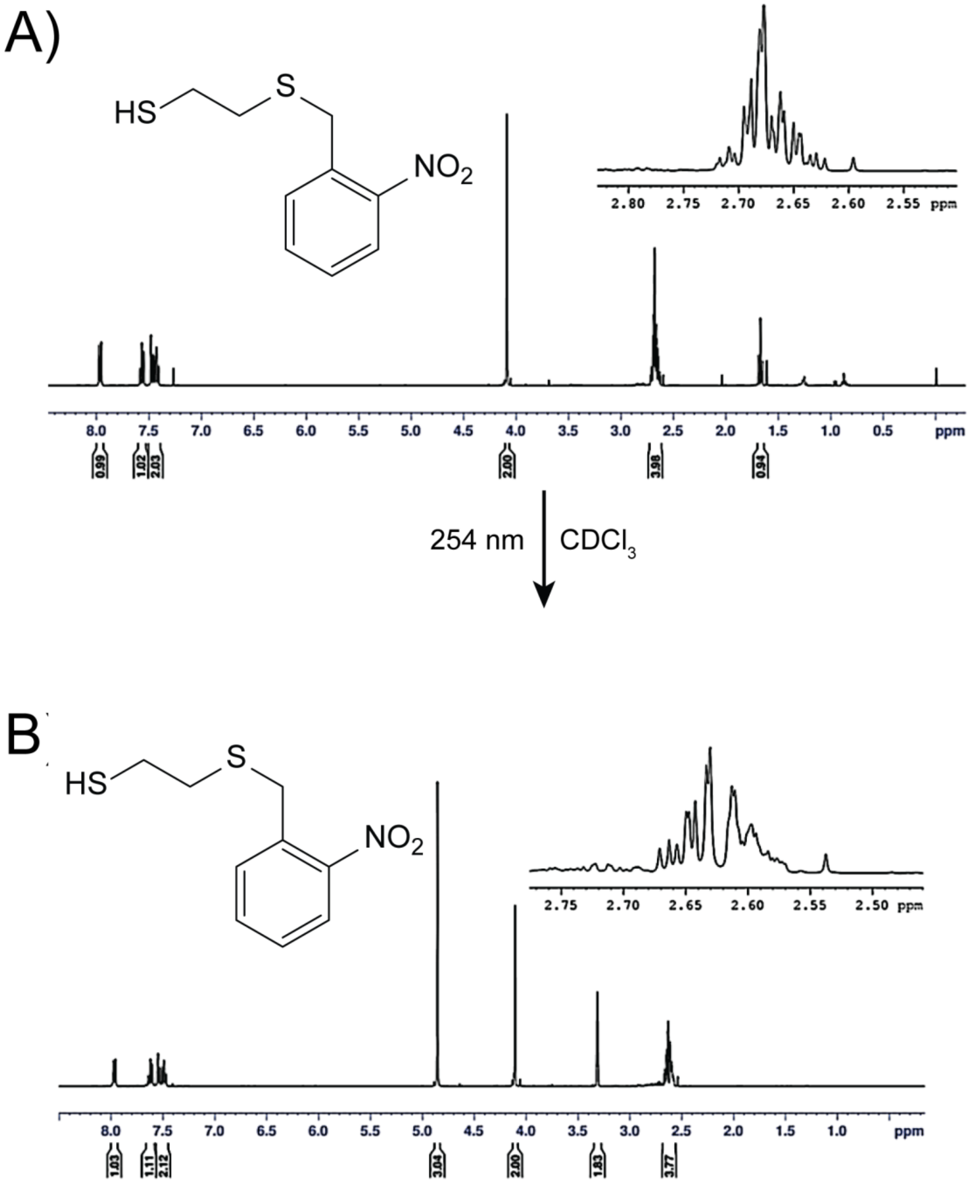

Figure C.1. Lack of degradation of NET when undergoing irradiation by a 4W 254 nm lamp for 4 hours.

C.8. NMR after 16 hour UV Irradiation of DMNC on PbS

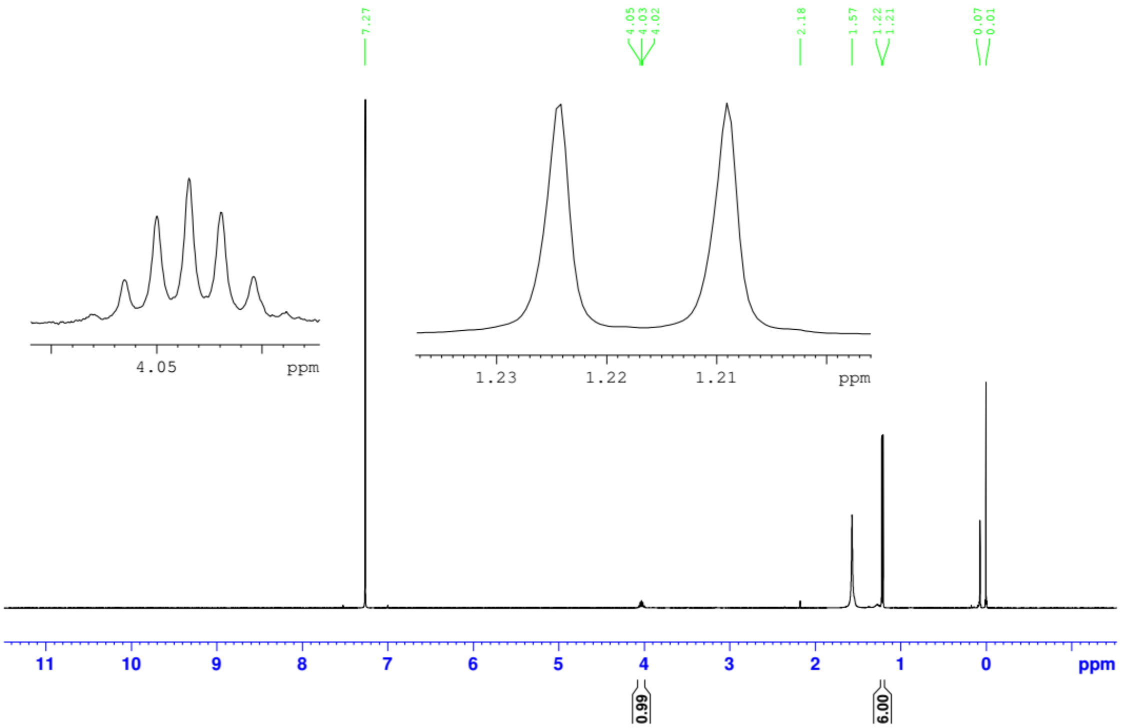

Figure C.2. Lack of free ligand when PbS ligand exchanged with DMNC is irradiated with a 4W 254 nm light overnight. If free ligand existed, a peak around ~10 ppm corresponding to the nitrosoaldehyde should be present.

C.9. UVVis Absorbance spectra of PbS ligand exchanged with DNMC before and after irradiation with UV light

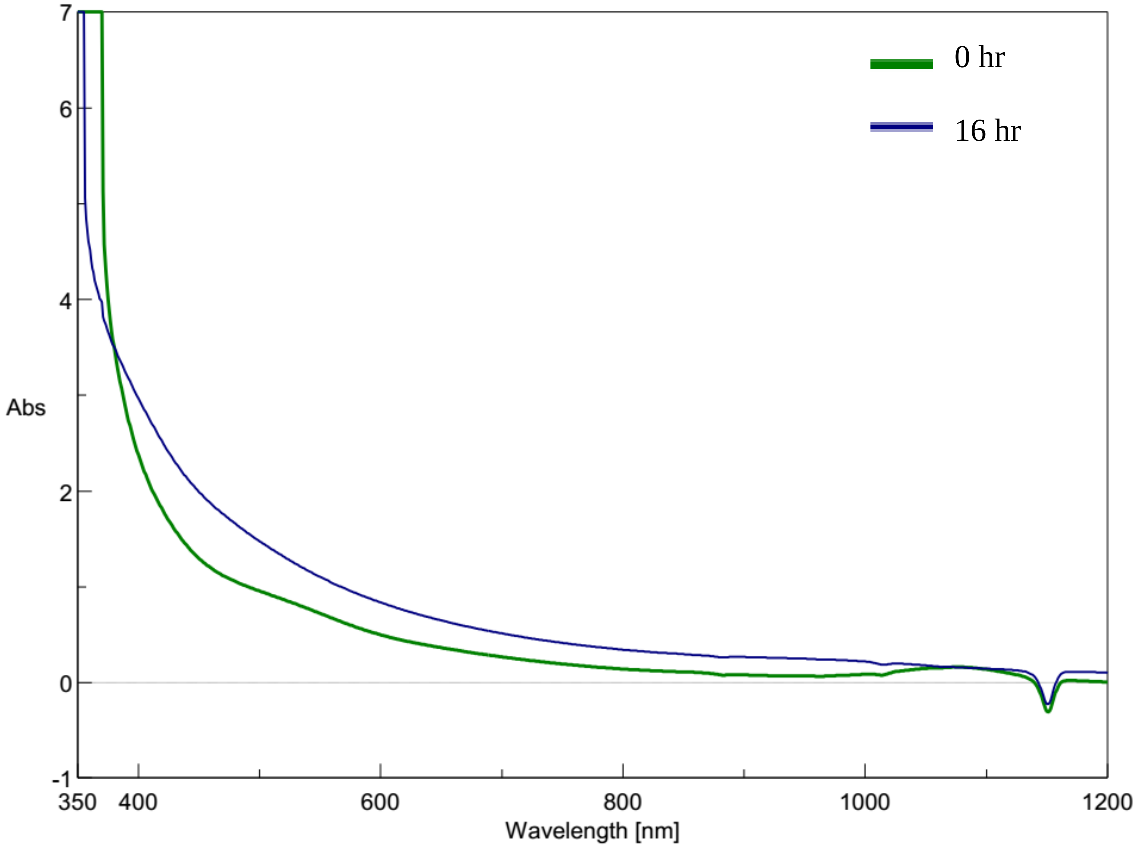

Figure C.3. Observance of ligand degradation via UVVis spectroscopy was not possible due to the occlusion of ligand absorbances by the PbS. Some absorbance is seen in the 16 hr sample due to scattering from precipitated PbS after prolonged irradiation.

D. Additional Procedures and Data for Chapter 5

D.1. General Synthetic Procedures

Pb Salt Synthesis. $Pb(NO_3)_2$ (1 mmol) was dissolved in 5 ml of deionized H_2O. Separately the desired thiol (in this case DDT, D3MP, FMT, DMC, or DTC) (2 mmol) was dissolved in 1 ml of acetone. The thiol solution was added dropwise to the lead solution. Another solution of 2 mmol of triethylamine in 1 ml of acetone was then added dropwise, resulting in precipitation of a yellow solid. The solid was filtered and allowed to dry on vacuum overnight.

$Pb(OAc)_2$ Syntheses. Pb(OAc)2 (1 mmol) and D3MP (6.65 ml) were added to a 25 ml round bottom flask with stir bar and inlet adapter and degassed at room temperature for 30 minutes. The flask was then flushed with Ar and heated to 200 °C where it was held for 10 minutes. The heating mantle was then removed and the reaction allowed to cool to room temperature. The particles were then cleaned via precipitation with ethanol and resuspension in chloroform three times before characterization.

Other Pb Salt Syntheses. Solvent (DPE or ODE, 9.6 ml) and surfactant (0.4 ml, same ligand as salt) were combined in a 25 ml three-neck round bottom flask with stir bar and condenser and degassed at 100 °C for 2 hours. Lead salt (0.4 mmol) in 2 ml of TOP was degassed at room temperature for 2 hours. A solution of TMS (0.1-0.3 mmol) in ODE (1 ml) was prepared in the glovebox. After 2 hours the lead salt and reaction flask were flushed with Ar. The reaction flask was heated to 140 °C. Both lead salt and TMS solutions were injected either at the same time or with a 5 second delay into the reaction solution. The reaction solution was allowed to grow for a set amount of time until the heating mantle was removed. The reaction solution was then centrifuged to remove insoluble debris. The particles were then cleaned via precipitation with ethanol and resuspension in hexanes three times prior to characterization. three time with ethanol and resuspended in hexanes prior to characterization.

D.2. Reaction Conditions for PbS Syntheses

Metal Precursor	Chalcogenide Precursor	Surfactants	Solvents	Temp (° C)	Time (min)	Morphology	Diameter (nm)
$Pb(OAc)_2$ (1 mmol)	DDT (6.67 ml)			200	10	Cubes	51.8 ± 4.7 (n=120)
$Pb(OAc)_2$ (1 mmol)	D3MP (6.67 ml)			200	10	Cubes	23.3 ± 1.7 (n=120)
$Pb(OAc)_2$ (1 mmol)	D3MP (6.67 ml)			200	10	Hexagons	24.8 ± 1.9 (n=120)
$Pb(OAc)_2$ (1 mmol)	D3MP (6.67 ml)			180	10	Hexagons	22.0 ± 1.2 (n=120)
$Pb(OAc)_2$ (0.5 mmol)	D3MP (6.67 ml)			180	10	Spherical	20.7 ± 1.9 (n=120)
$Pb(OAc)_2$ (2 mmol)	D3MP (6.67 ml)			180	10	Spherical	25.2 ± 4.6 (n=120)
$Pb(OAc)_2$ (1 mmol)	D3MP (6.67 ml)		ODE (3.33 ml)	180	10	Spherical	23.3 ± 3.5 (n=120)
$Pb(OAc)_2$ (1 mmol)	D3MP (6.67 ml)			190	10	Cubes	Agg
$Pb(DTC)_2$ (0.2 mmol)	Injection-TMS (0.2 mmol) in ODE (1 ml)	HDA (6.2 mmol)	TOP (2 ml)	70	60	Cubes (agg)	PD/Agg
$Pb(DTC)_2$ (0.2 mmol)		Injection-OLAM (0.7 mmol) in ODE (1 ml)	ODE (5 ml)	180	1	Cubes	Agg
$Pb(DTC)_2$ (0.2 mmol)		Injection-OA (0.7 mmol) in ODE (1 ml)	ODE (5 ml)	180	5	n/a	n/a
$Pb(DTC)_2$ (0.2 mmol)		Injection-OLAM (0.7 mmol) in ODE (1 ml)	DPE (5 ml)	125	1	n/a	n/a
$Pb(DTC)_2$ (0.2 mmol)	Injection 2-TMS (0.1 mmol) in ODE (1 ml)	Injection 1-OLAM (0.7 mmol) in ODE (1 ml)	DPE (5 ml)	125	1	n/a	Agg
$Pb(DTC)_2$ (0.2 mmol)	Injection 1-TMS (0.1 mmol) in ODE (1 ml)		DPE (5 ml)	125	1	n/a	Agg
$Pb(DTC)_2$ (0.2 mmol)	Injection 1-TMS (0.1 mmol) in ODE (1 ml)		DPE (5 ml)	125	1	Cubes	PD/Agg
$Pb(DTC)_2$ (0.2 mmol)	Injection 2-TMS (0.1 mmol) in ODE (1 ml)	Injection 2-OLAM (2.8 mmol)	DPE (5 ml)	125	1	n/a	Agg
$Pb(DTC)_2$ (0.2 mmol)	Injection 1-TMS (0.1 mmol) in ODE (1 ml)	Injection 2-DDT (0.7 mmol) in DPE (1 ml)	DPE (5 ml)	125	1	n/a	Agg
$Pb(DTC)_2$ (0.2 mmol)	Injection-DDT (0.7 mmol) in DPE (1 ml)		DPE (5 ml)	125	20	Cubes	Agg
Injection $Pb(DTC)_2$ (0.2 mmol) in ODE (1.5 ml)			OLAM (5 ml)	300	1.5	n/a	Agg
$PbCl_2$ (0.2 mmol)	Injection-Sulfur (0.67 mmol) in OLAM (2.5 ml)		OLAM (5 ml)	220	60	Spherical	
$PbCl_2$ (0.2 mmol)	Injection 1-FMT (0.5 mmol) in DPE (0.5 ml)	Injection 2-TMS (0.1 mmol) in ODE (0.5 ml)	DPE (5 ml) DMSO (3 ml)	135	1.5	n/a	Agg
$PbCl_2$ (0.2 mmol)	Injection 1-FMT (0.5 mmol) in DPE (0.5 ml)	Injection 2-TMS (0.1 mmol) in ODE (0.5 ml)	DPE (5 ml) DMSO (3 ml)	80	1.5	n/a	Agg
$PbCl_2$ (0.2 mmol)	Injection 1-FMT (0.5 mmol) in DPE (0.5 ml)	Injection 2-TMS (0.1 mmol) in ODE (0.5 ml)	DPE (5 ml) DMSO (3 ml)	25	1.5	n/a	Agg

$PbCl_2$ (0.2 mmol)	Injection 1-Toluene (0.5 mmol) in DPE (0.5 ml)	Injection 2-TMS (0.1 mmol) in $CHCl_3$ (0.5 ml)	Toluene (5 ml) DMSO (3 ml)	0	5	n/a	Agg
Injection-Pb$(DDT)_2$ (0.2 mmol) in TOP (1.5 ml)			ODE (5 ml)	210	10	n/a	Agg
Injection 1-Pb$(DDT)_2$ (0.2 mmol) in ODE (1.5 ml)	Injection 2-TMS (0.1 mmol) in ODE (1 ml)		ODE (5 ml)	125	1	Spherical	3.4 ± 0.4 (n=120)
Injection 1-Pb$(DDT)_2$ (0.2 mmol) in TOP (1 ml)	Injection 2-TMS (0.1 mmol) in ODE (1 ml)		ODE (5 ml)	125	1	Spherical	3.8 ± 0.5 (n=120)
Injection 1-Pb$(DDT)_2$ (0.2 mmol) in TOP (1 ml)	Injection 2-TMS (0.1 mmol) in ODE (1 ml)		ODE (5 ml)	100	1	n/a	NU
Injection 1-Pb$(DDT)_2$ (0.2 mmol) in TOP (1 ml)	Injection 2-TMS (0.1 mmol) in ODE (1 ml)		ODE (5 ml)	140	1	Spherical	4.2 ± 0.5 (n=120)
Injection 1-Pb$(DDT)_2$ (0.2 mmol) in TOP (1 ml)	Injection 2-TMS (0.1 mmol) in ODE (1 ml)		ODE (5 ml)	160	1	Spherical	4.7 ± 0.5 (n=120)
Injection 1-Pb$(DDT)_2$ (0.2 mmol) in TOP (1 ml)	Injection 2-TMS (0.1 mmol) in ODE (1 ml)		ODE (5 ml)	140	1	Spherical	
Injection 1-Pb$(DDT)_2$ (0.2 mmol) in TOP (1 ml)	Injection 2-TMS (0.2 mmol) in ODE (1 ml)		ODE (5 ml)	140	1	Spherical	
Injection 1-Pb$(DDT)_2$ (0.2 mmol) in TOP (1 ml) and ODE (1 ml)	Injection 2-TMS (0.1 mmol) in ODE (1 ml)		ODE (5 ml)	140	1.5	Spherical	3.8 (calc)
Injection 1-Pb$(DDT)_2$ (0.2 mmol) in TOP (1 ml) and ODE (1 ml)	Injection 2-TMS (0.1 mmol) in ODE (1 ml)		ODE (5 ml)	140	1.5	Spherical	3.8 (calc)

Injection 1-Pb(DDT)$_2$ (0.2 mmol) in TOP (1 ml) and ODE (1 ml)	Injection 2-TMS (0.1 mmol) in ODE (1 ml)		ODE (5 ml)	140	1.5	Spherical	
Injection 1-Pb(DDT)$_2$ (0.2 mmol) in TOP (1 ml) and ODE (1 ml)	Injection 2-TMS (0.1 mmol) in ODE (1 ml)		ODE (5 ml)	140	1.5	Spherical	1.9 (calc)
Injection 1-Pb(D3MP)$_2$ (0.2 mmol) in TOP (1 ml) and ODE (1 ml)	Injection 2-TMS (0.1 mmol) in ODE (1 ml)		ODE (5 ml)	140	1.5	Spherical	4.2 ± 0.3 (n=120)
Injection 1-Pb(D3MP)$_2$ (0.6 mmol) in TOP (1 ml) and ODE (1 ml)	Injection 2-TMS (0.3 mmol) in ODE (1 ml)		ODE (15 ml)	140	1.5	Spherical	
Injection 1-Pb(D3MP)$_2$ (0.6 mmol) in TOP (3 ml)	Injection 2-TMS (0.3 mmol) in ODE (1 ml)		ODE (5 ml)	140	1.5	Spherical	
Injection 1-Pb(D3MP)$_2$ (0.2 mmol) in TOP (1 ml) and ODE (1 ml)	Injection 2-TMS (0.1 mmol) in ODE (1 ml)		DPE (5 ml)	140	1.5	Spherical	4.1 (calc)
Injection 1-Pb(D3MP)$_2$ (0.2 mmol) in TOP (1 ml) and ODE (1 ml)	Injection 2-TMS (0.1 mmol) in ODE (1 ml)		ODE (4.8 ml) D3MP (0.4 mmol)	140	1.5	Spherical	4.3 (calc)
Injection 1-Pb(D3MP)$_2$ (0.2 mmol) in TOP (1 ml) and ODE (1 ml)	Injection 2-TMS (0.1 mmol) in ODE (1 ml)		ODE (2.5 ml) D3MP (2.5 ml)	140	1.5	Spherical	4.3 (calc)
Injection 1-Pb(D3MP)$_2$ (0.2 mmol) in TOP (1 ml) and ODE (1 ml)	Injection 2-TMS (0.1 mmol) in ODE (1 ml)		ODE (4.8 ml) D3MP (0.2 mmol)	140	1.5	Spherical	3.7 (calc)

Injection 1-Pb(D3MP)$_2$ (0.4 mmol) in TOP (2 ml) and ODE (1 ml)	Injection 2-TMS (0.2 mmol) in ODE (1 ml)		ODE (9.6 ml) D3MP (0.4 ml)	140	1.5	Spherical	4.3 (calc)
Injection 1-Pb(D3MP)$_2$ (0.4 mmol) in TOP (2 ml) and ODE (1 ml)	Injection 2-TMS (0.2 mmol) in ODE (1 ml)		ODE (9.6 ml) D3MP (0.4 ml)	140	1.5	Spherical	4.5 (calc)
Injection 1-Pb(D3MP)$_2$ (0.4 mmol) in TOP (2 ml)	Injection 2-TMS (0.2 mmol) in ODE (1 ml)		ODE (9.6 ml) D3MP (0.4 ml)	190	5	Spherical	
Injection 1-Pb(D3MP)$_2$ (0.4 mmol) in TOP (2 ml)	Injection 2-TMS (0.2 mmol) in ODE (1 ml)		D3MP (10 ml)	190	10	Cubes	Agg
Injection 1-Pb(D3MP)$_2$ (0.4 mmol) in TOP (2 ml)	Injection 2-TMS (0.2 mmol) in ODE (1 ml)		D3MP (10 ml)	180	10	Cubes	
Injection 1-Pb(D3MP)$_2$ (0.4 mmol) in TOP (2 ml)	Injection 2-TMS (0.2 mmol) in ODE (1 ml)		D3MP (10 ml)	180	10	Cubes	
Injection 1-Pb(D3MP)$_2$ (0.2 mmol) in TOP (1 ml) and ODE (1 ml)	Injection 2-TMS (0.1 mmol) in ODE (1 ml)		ODE (5 ml)	140	1.5	Spherical	4.0 (calc)
Injection 1-Pb(DMC)$_2$ (0.2 mmol) in TOP (1 ml) and ODE (1 ml)	Injection 2-TMS (0.1 mmol) in ODE (1 ml)		ODE (5 ml)	140	1.5	Spherical	4.6 (calc)
Injection 1-Pb(DMC)$_2$ (0.2 mmol) in TOP (1 ml) and ODE (1 ml)	Injection 2-TMS (0.1 mmol) in ODE (1 ml)		ODE (5 ml)	140	1.5	Spherical	

Injection 2-Pb$(FMT)_2$ (0.05 mmol) in ODE (1 ml)	Injection 1-TMS (0.025 mmol) in ODE (0.5 ml)	FMT (0.1 mmol)	ODE (5 ml)	170	n/a	n/a	
Injection 2-Pb$(FMT)_2$ (0.1 mmol) in DCB (2 ml)	Injection 1-TMS (0.05 mmol) in ODE (0.5 ml)	FMT (0.3 mmol)	ODE (5 ml)	150	n/a	n/a	

Figure C.1. Various reaction conditions. Abbreviations: dodecanethiol (DDT), bis-trimethylsilyl sulfide (TMS), dithiocarbamate (DTC), hexadecylamine (HDA), octadecene (ODE), trioctylphosphine (TOP), diphenyl ether (DPE), oleylamine (OLAM), oleic acid (OA), O-((9H-fluoren-9-yl)methyl) S-(2-mercaptoethyl) carbonothioate (FMT), O-dodecyl S-(2-mercaptoethyl) carbonothioate (DMC), polydisperse (PD), and agglomerated (Agg).

D.3. Absorption spectra of PbS QDs.

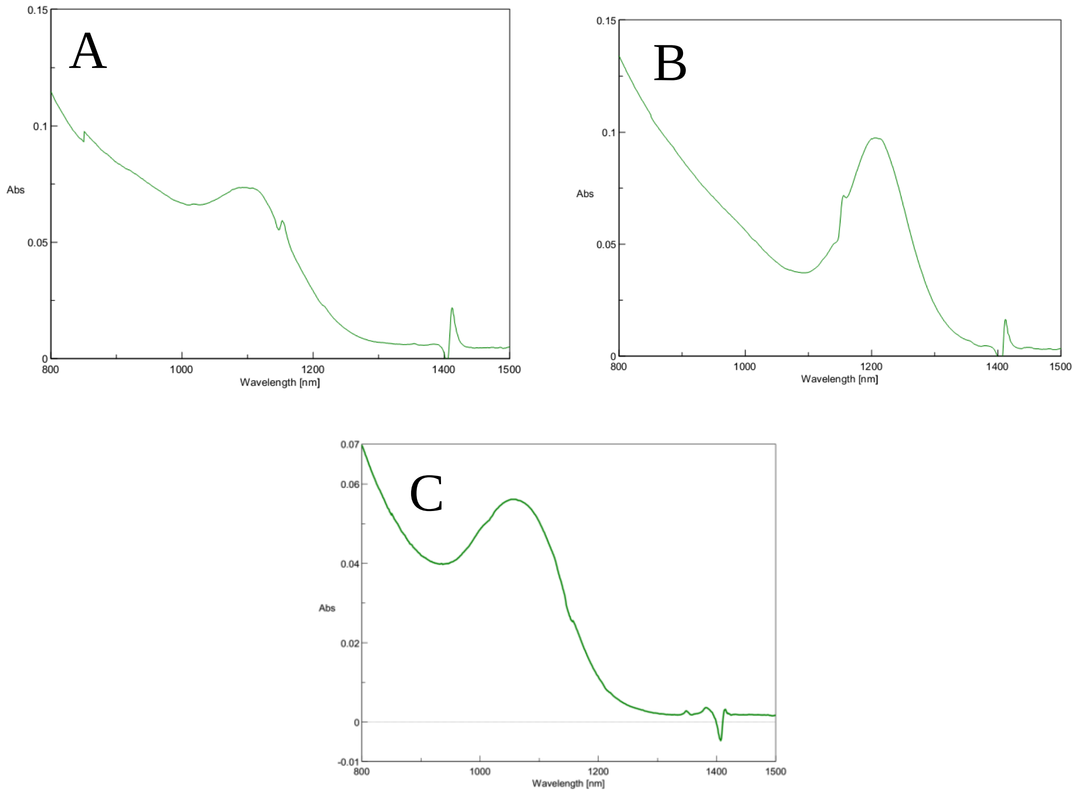

Figure C.2. Absorption spectra of PbS QDs. A) DDT-capped crystal bound PbS (λ_{ex}=1107 nm), B) D3MP-capped crystal bound PbS (λ_{ex}=1210 nm), C) Surface bound DDT-capped surface bound PbS (λ_{ex}=1058 nm).

19 Briarwood Ct.
Lyman, SC 29365

Phone (cell) (+1) 864-706-9032
adylanlacroix@gmail.com

Andrew Dylan La Croix

Education

Vanderbilt University, Nashville, TN
Expected Graduation Sept. 2018
PhD in Chemistry
Advisor: Janet E. Macdonald

Lander University, Greenwood, SC
2012 B.S. in Chemistry, *summa cum laude*

Research Experience

Macdonald Laboratory, Vanderbilt University, Aug. 2012 – Sept. 2018

- Studied the surface chemistry of semi-conducting nanoparticles
- Synthesized unique ligands to impart exotic functionality on inorganic semiconductor materials
- Worked towards developing improved methods of solar cell fabrication
- Maintained lab equipment (GC, Spectrometers, Glovebox, etc.)

Brodhacker Laboratory (Lander University, Undergraduate)

- Synthesized molecules for shrinkage reduction in polymers
- Followed synthetic route for production of azo-benzene polymers
- Funded by the NASA Jet Propulsion Laboratory

Teaching

Lab Teaching Assistant, Vanderbilt University

Organic Chemistry, 2012-2016, Multiple Semesters

- Supervised students in lab environment
- Assessed lab technique
- Evaluated written reports

Senior Capstone, 2015, Spring

- Assisted in development of novel research ideas
- Led students through research program

Analytical Chemistry, 2013, Spring

- Demonstrated proper lab technique
- Communicated results from written reports

Undergraduate Mentor, Vanderbilt University

Various Students, 2014-2018

- Took charge of single or groups of students
- Relegated research tasks for completion of projects
- Fostered welcoming learning environment

Selected Publications

Andrew D. La Croix, James Z. Fan, Zhenyu Yang, Emma Howard, Rafael Quintero-Bermudez, Larissa Levina, Nicole M. Jenkinson, Yiying Li, Zheng-Hong Lu, Edward H. Sargent, and Janet E. Macdonald, “Multi-step Ligand Exchange On P-type Quantum Dots Facilitates High-performance Solar Cells,” *ACS Energy Lett.,* **Submitted.**

Andrew D. La Croix, Andrew O'Hara, Kemar R. Reid, Noah J. Orfield, Sokrates T. Pantelides, Sandra J. Rosenthal, Janet E. Macdonald, "Design of a Hole Trapping Ligand," *Nano Lett.*, **2017**, 17 (2): 909-914.

Lisa K. Brodhacker, Joe Ritter, **Andrew D. La Croix,** Bruce Holenstein, Russel M. Genet, "Recent Developments in the Production of Spin-cast Epoxy Mirrors," *Proc. SPIE 8971, Free-Space Laser Communication and Atmospheric Propagation XXVI*, 89710O (6 March 2014).

Selected Presentations

ACS National Meeting Denver, CO, 2015 (Oral Presentation)
Progress towards complete photocatalytic water splitting utilizing hybrid nanoparticles

Gordon Research Conference, Mt. Snow, VT, 2016 (Poster Presentation)
Electronic interaction of dithiocarbamate ligands with nanorods for hole transport to an attached metal center

TN-SCORE Conference, Nashville, TN, 2013 (Invited Oral Presentation)
Photo-oxidation and Reduction of Water Utilizing Pt-tipped CdSe/CdS Hybrid Nanostructures with Hole-Extracting Ligands

Sixth Annual Alt-Az Initiative Conference, Portland, OR, 2012 (Invited Oral Presentation)
Synthesis and Characterization of Spiro Orthocarbonate compounds for the use of Shrinkage Reduction in Epoxy Telescope Mirrors

Awards

Mitchum E. Warren, Jr. Graduate Research Fellowship, 2017

South Carolina Space Consortium Grant, 2012
Grant awarding $5000 to a student and $30,000 to the lab for summer research.

Research Grant from the University of Hawaii Institute for Astronomy
Grant in the amount of $1600 for studying "The synthesis of azobenzene compounds for photonic muscle space telescopes."

Leadership

Member of Mitchum E. Warren Graduate Student Committee, 2015-2016
Organization of student seminars and invitation of prestigious speaker

President of Local American Chemical Society Chapter, 2011-2012
Led the chapter in instilling enthusiasm within the university and community